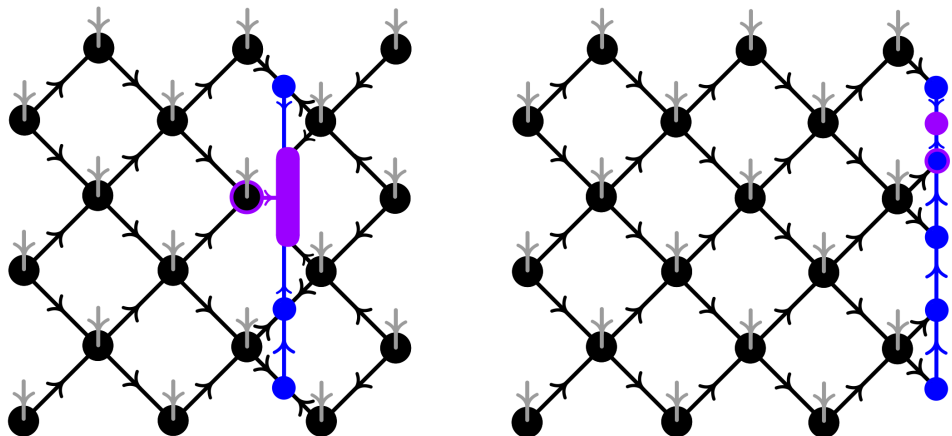


VARIATIONAL GROUND STATES
AND QUASIPARTICLE EXCITATIONS
IN ISOMETRIC TENSOR NETWORK STATES

Master's Thesis
Quantum Science and Technology

Technische Universität München (TUM) and Ludwig-Maximilians-Universität (LMU)

Lukas Julius Wittmann



Chair of Solid-State Theory
TUM School of Natural Sciences, Department of Physics
Technical University of Munich

September 2025

Supervisor: Dr. Johannes Hauschild
First examiner: Prof. Dr. Frank Pollmann
Second examiner: Prof. Dr. Michael Knap

Abstract

Quantum many-body systems give rise to rich emergent phenomena in their ground states and elementary excitations. Extracting theoretical predictions for experimentally measurable quantities—such as the dynamical structure factor—requires numerical methods that overcome the exponential growth of the Hilbert space with system size. On finite and infinite chains, ground states of local, gapped Hamiltonians can be faithfully approximated within the manifold of matrix product states (MPS). Algorithms for finding these representations are well established in form of the density matrix renormalization group (DMRG) and variational uniform matrix product states (VUMPS). For a ground state in the smooth manifold, the tangent space is spanned by local tensor perturbations and is therefore well suited to variationally optimize quasiparticle excitations therein. All these 1D methods benefit from an isometric canonical form that can be reached exactly within the internal gauge freedom. In two dimensions, projected entangled pair states (PEPS) provide the natural generalization of MPS. Due to closed loops in the virtual network, an analogous canonical form can only be imposed on a strict variational subset. Isometric projected entangled pair states (isoPEPS) enforce an orthogonality column, which enables the generalization of the successful 1D DMRG algorithm to 2D, dubbed DMRG². The main challenges concern shifting the orthogonality column with minimal error and efficiently compressing the boundaries of the energy expectation value. The first part of this thesis is devoted to reproducing the ansätze and algorithms in 1D. Building on this foundation, we study isoPEPS on a diagonal square lattice in the second part. In particular, we newly propose **(i) a bulk-weighted boundary compression scheme** that explicitly exploits the isometric form to improve the performance of DMRG², and **(ii) an ansatz for variational quasiparticle excitations**. Our Python implementations of all algorithms are openly available in a Git repository [Wit25]. We perform benchmarks on the transverse field Ising model and find that the quasiparticle ansatz faithfully captures the low-energy excitations.

Contents

Abstract	i	
1	Introduction	1
2	Transverse field Ising model	3
2.1	Qualitative quantum phase diagram	3
2.2	Perturbation theory for large and small transverse field	4
2.3	Exact solution in one dimension	9
3	Tensor network basics	11
4	Uniform matrix product states (uMPS)	15
4.1	Primitivity, the manifold and its tangent space	15
4.2	Intrinsic canonical form and area law	17
4.3	Variational uniform matrix product states (VUMPS)	20
4.4	Variational plane wave excitations (VPWE)	26
5	Matrix product states (MPS)	31
5.1	Intrinsic canonical form	32
5.2	Density matrix renormalization group (DMRG)	33
5.3	Variational quasiparticle excitations (VQPE)	38
6	Isometric projected entangled pair states (isoPEPS)	45
6.1	Imposed canonical form and Yang-Baxter move	46
6.2	Boundary compression	50
6.3	Density matrix renormalization group squared (DMRG ²)	57
6.4	Variational quasiparticle excitations	65
7	Conclusion and outlook	81
A	Detailed Jordan-Wigner and Bogoliubov transformation	87
B	Quantum channels and matrix product states	93
C	Extensive tensor network diagrams	105
Bibliography		116

Chapter 1

Introduction

Quantum many-body systems exhibit rich emergent phenomena. When sufficiently cooled down, most spin systems spontaneously break a symmetry and show magnetic long-range order. However, there are more exotic and less understood strongly correlated phases of matter, such as quantum spin liquids (QSL) in two dimensions. Features that qualify a system as such are topological ground state degeneracy, long-range entanglement and the emergence of fractionalized quasiparticle excitations. Numerical methods are indispensable for making quantitative theoretical predictions about observables—such as the dynamical structure factor—that are experimentally measurable in candidate materials. [KM19]

The central challenge in numerical approaches is the exponential growth of the Hilbert space dimension with system size. Exact diagonalization (ED) methods, which directly tackle the energy eigenvalue problem, are therefore limited to a few tens of spins, even when employing iterative Lanczos algorithms and exploiting symmetries of the Hamiltonian. Quantum Monte Carlo (QMC) methods do not operate on the high dimensional Hamiltonian matrices and state vectors explicitly, but stochastically sample over configuration spaces. While being extremely efficient for bipartite systems, for geometrically frustrated spin systems—prime QSL candidates—QMC methods are plagued by the sign problem: statistical errors get out of control due to fluctuating signs of the configuration weights. [San10]

Approximating the wavefunction with a network of low-dimensional tensors and not suffering from the sign problem, tensor network state methods open up a promising third path. The density matrix renormalization group (DMRG) algorithm [Whi92], later reformulated as a variational optimization over matrix product states (MPS) [Sch11], is the state-of-the-art method for finding ground states in one dimension. Its success can be explained with the area law of entanglement [Has07] for ground states of local, gapped 1D Hamiltonians and the ability of MPS to represent such states faithfully [VC06]. In the thermodynamic limit, DMRG can be applied in its infinite version, which successively grows the unit cell and recovers translation invariance asymptotically. Alternatively, the variational uniform matrix product states (VUMPS) algorithm [ZSVF⁺18] completely updates uniform MPS (uMPS) with each iteration and therefore keeps translation invariance at any time. Identifying the set of matrix product states as a smooth complex manifold [HMOV14] provided the geometric foundation for tangent space based approaches [HOV13]. The time-dependent variational principle (TDVP) projects the right hand side of the Schrödinger equation onto the tangent space, ensuring that the time evolution never leaves the manifold. It was formulated both for the infinite uniform [HCO⁺11] and finite [HLO⁺16] MPS. Moreover, since the tangent space results from infinitesimal deviations from the original ground state tensors, it is very natural to think of it as the space in which elementary excitations live. For uMPS, a plane wave superposition with definite momentum can be formed from the states in which the tensor is replaced on a single site [HPW⁺12, VHV19b]. For finite MPS with open boundary conditions, the local perturbations are superposed without explicit momentum coefficient [VDVH⁺21]. In both cases, the perturbation parameters have to be optimized energetically. As for the ground state and any

other effective eigenvalue problem, isometric conditions improve the numerical stability. For matrix product states with open boundary conditions, such a canonical form can be achieved exactly within the internal gauge degrees of freedom. This is not the case when generalizing MPS to two dimensions, which brings us to projected entangled pair states (PEPS) [VC04]. Although PEPS offer great variational power for representing area law states, the presence of closed loops in the virtual legs prevents the existence of an analogous canonical form and thus leads to generalized eigenvalue problems. This was the motivation for Zaletel and Pollmann [ZP20] to further restrict the variational ansatz to isometric projected entangled pair states (isoPEPS). Although forming a strict PEPS subset, isoPEPS are conjectured to capture all gapped phases with gappable edges [SSB⁺20]. The imposed orthogonality column enables an algorithm dubbed DMRG² [LZP22], the generalization of the successful 1D DMRG algorithm to 2D. The main challenges here concern shifting the orthogonality column as error-free as possible, and finding an efficient way to compress the boundary terms in the energy expectation value. To our knowledge, a quasiparticle excitation ansatz has so far only been studied for infinite PEPS [VMVH15, VHV19a], but not yet for isoPEPS. In this thesis, we work on a diagonal square lattice, for which an isometric form was recently introduced in [SKZP25]. In particular, we develop two new methods:

- 1) In section 6.2 we propose a new bulk-weighted boundary compression scheme that explicitly exploits the isometric structure of isoPEPS. Compared to the standard variational compression, the energy expectation value converges much faster with boundary bond dimension. In accordance with this, DMRG² achieves significantly lower energy errors, which we demonstrate in section 6.3.
- 2) In section 6.4 we introduce an isoPEPS quasiparticle excitation ansatz. It parametrizes the tangent space vector such that all desired orthogonality properties are fulfilled. We optimize it (i) from overlap with exact wavefunctions or MPS, and (ii) by diagonalization of the effective Hamiltonian.

Along the way, we cover the following: In chapter 2 we present the transverse field Ising (TFI) model, which is the paradigmatic model of quantum many-body spin systems and serves as a benchmark for all algorithms in this thesis. After having equipped ourselves with the basic tensor network tools and notations in chapter 3, we deal with the manifold of uMPS in chapter 4. We reproduce the established algorithms for variationally finding the ground state and quasiparticle excitations on top. We follow the same agenda for finite MPS in chapter 5. Finally, in chapter 6, we set the stage for isoPEPS on the diagonal square lattice in section 6.1, followed by a presentation of our newly developed methods 1) and 2). We close with conclusion and outlook in chapter 7. All described algorithms are implemented in open-source Python code [Wit25].

Chapter 2

Transverse field Ising model

Owing to its simple yet rich structure, the *transverse field Ising* (TFI) model serves as the paradigm example of a quantum many-body spin system. It contains an interaction term favoring magnetic alignment (in x -direction) and a transverse field term introducing quantum fluctuations (in z -direction). The Hamiltonian reads

$$H = -J \sum_{\langle n,m \rangle} \sigma_n^x \sigma_m^x - g \sum_n \sigma_n^z, \quad (2.1)$$

where $\langle n, m \rangle$ denotes a pair of nearest neighbors on a hypercubic lattice of N sites, and

$$\sigma^x = \begin{pmatrix} 0 & 1 \\ 1 & 0 \end{pmatrix}, \quad \sigma^y = \begin{pmatrix} 0 & -i \\ i & 0 \end{pmatrix}, \quad \sigma^z = \begin{pmatrix} 1 & 0 \\ 0 & -1 \end{pmatrix} \quad (2.2)$$

are the spin-1/2 Pauli matrices. We take the computational basis to be the σ^z -eigenbasis $\{| \uparrow \rangle, | \downarrow \rangle\}$ with eigenvalues $\{+1, -1\}$. The eigenvectors of σ^x , with eigenvalues $+1$ and -1 , are given by

$$| \rightarrow \rangle = \frac{1}{\sqrt{2}}(| \uparrow \rangle + | \downarrow \rangle), \quad | \leftarrow \rangle = \frac{1}{\sqrt{2}}(| \uparrow \rangle - | \downarrow \rangle). \quad (2.3)$$

We restrict ourselves to ferromagnetic interaction $J > 0$ and adopt the convention $g > 0$. Since the properties of the model only depend on the dimensionless ratio g/J , we often set $J = 1$ and vary g . Ultimately, we are interested in the ground state and the elementary excitations above it.

2.1 Qualitative quantum phase diagram

In the Landau (non-topological) framework, quantum phases—and the transitions between them—are characterized by ground state symmetry properties, local order parameters, the decay behavior of correlation functions, the energy gap in the thermodynamic limit, and the nature of elementary excitations [Sac11].

The TFI Hamiltonian (2.1) is invariant under a global spin-flip along the z -axis. More precisely, it has a \mathbb{Z}_2 -symmetry generated by the unitary operator

$$U = \prod_n \sigma_n^z, \quad (2.4)$$

such that $[H, U] = 0$. A state $|\psi\rangle$ is called symmetric if, up to a global phase, it is mapped to itself: $U|\psi\rangle = e^{i\varphi}|\psi\rangle$. With $\langle \cdot \rangle$ denoting the expectation value in the ground state $|0\rangle$,

$$m = \langle \sigma^x \rangle = \frac{1}{N} \sum_n \langle \sigma_n^x \rangle, \quad C_{nm} = \langle \sigma_n^x \sigma_m^x \rangle \quad (2.5)$$

serve as magnetization order parameter and correlation function.

Connecting the two trivial limits $g \gg J$ and $g \ll J$, we can qualitatively infer the following quantum phase diagram (illustrated in figure 2.1):

$g \gg J$: In the unique and symmetric ground state $|\uparrow\rangle = |\dots \uparrow\uparrow\dots\rangle$, all N spins are paramagnetically aligned along the $+z$ -direction, with total energy $E_0 = -gN$. The expectation value in x -direction vanishes at all sites, and different spins are completely uncorrelated: $m = 0$, $C_{nm} = \delta_{nm}$. The elementary excitations are single spin flips $|\dots \uparrow \downarrow \uparrow \dots\rangle$ of nonzero energy cost $2g$.

Moving to slightly smaller g , we expect the correlations to stay short-ranged and decay exponentially: $C_{nm} \sim e^{-|n-m|/\xi}$, with correlation length ξ .

$g \ll J$: There are two degenerate ground states $|\Rightarrow\rangle = |\dots \rightarrow\rightarrow\rightarrow\dots\rangle$ and $|\Leftarrow\rangle = |\dots \leftarrow\leftarrow\leftarrow\dots\rangle$ with energy $E_0 = -zJN/2$, where z is the coordination number of the hypercubic lattice. They are not symmetric but transform into each other under application of U . In the thermodynamic limit, a system spontaneously chooses one of the two degenerate ground states, which is commonly referred to as *spontaneous symmetry breaking* (SSB). The magnetization in x -direction has the maximum ferromagnetic value of $m = \pm 1$ and spins on different sites are long-range ordered with $C_{nm} = 1$. In one dimension, the lowest-lying excitations are topological domain walls $|\dots \rightarrow\rightarrow \leftarrow\leftarrow \dots\rangle$ with nonzero energy cost $2J$.

Moving to slightly larger g , quantum fluctuations are expected to reduce magnetization and long-range correlation to smaller but still nonzero values: $m = \pm m_0$, $C_{nm} = m_0^2$, with $0 < m_0 < 1$.

g_c : The qualitatively distinct ground states of the two limits cannot be analytically connected as tuning the transverse field g . This implies the existence of a critical value g_c at which the system exhibits a non-analytic quantum phase transition—from a symmetric disordered ground state for $g > g_c$ to a symmetry-broken ferromagnetic ground state for $g < g_c$. At the critical point, the energy gap above the ground state closes and correlations decay algebraically: $C_{nm} \sim |n - m|^{-\eta}$, with critical exponent η .

In section 2.3 we will show by exact solution that $g_c = J$ in one spatial dimension. In two dimensions cluster Monte Carlo simulations yield $g_c \approx 3.044J$ [BD02].

2.2 Perturbation theory for large and small transverse field

As a next step we want to find out how the degenerate first excited levels are quantitatively shifted when slightly moving away from the extreme limits $g \gg J$ and $g \ll J$.

Suppose we have a Hamiltonian H^0 which is easily diagonalized into degenerate groups (labelled by Greek letters) and orthonormal states within these groups (labelled by Latin letters):

$$H^0 |\alpha, n\rangle = E_\alpha |\alpha, n\rangle. \quad (2.6)$$

We investigate the influence of a perturbation λV , which is controlled by a small perturbation parameter λ . We assume that the energy differences $|E_\alpha - E_\beta|$ between groups are sufficiently

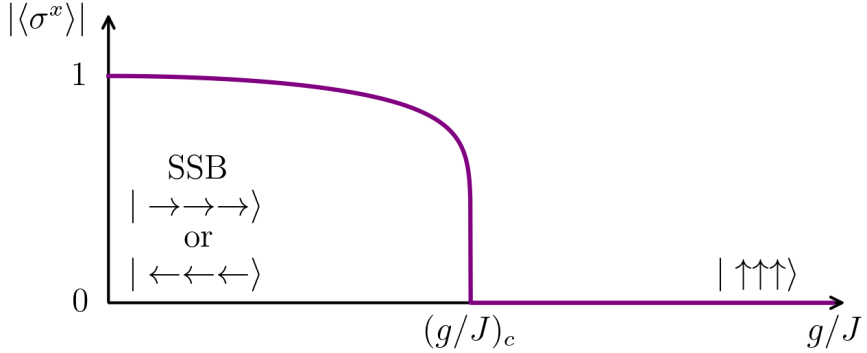


Figure 2.1: Qualitative quantum phase diagram for the TFI model on a hypercubic lattice. For $g \ll J$ the system spontaneously chooses one of the two degenerate, symmetry-broken ground states $|\Rightarrow\rangle$ and $|\Leftarrow\rangle$, with ferromagnetic magnetizations $\langle \sigma^x \rangle = 1$ and $\langle \sigma^x \rangle = -1$. With increasing g/J , quantum fluctuations reduce the magnetization magnitude to the value 0 at the critical point, where the system undergoes a quantum phase transition to a paramagnetic phase with unique symmetric ground state ($|\uparrow\rangle$ for $g \gg J$). Analytical solution and Monte Carlo simulations yield $g_c = J$ and $g_c \approx 3.044J$ in 1D and 2D, respectively.

large and use the effective Hamiltonian method [Sac11], which unitarily eliminates nonzero inter-group matrix elements to restrict the study to modified energy levels within each group. Going from the unperturbed energies in zeroth order up to second order in perturbation theory, the effective intra-group matrix elements are given by

$$\langle \alpha, n | H_{\text{eff},\alpha} | \alpha, m \rangle = E_\alpha \delta_{n,m} + \lambda \langle \alpha, n | V | \alpha, m \rangle + \lambda^2 \sum_{\beta \neq \alpha} \sum_l \frac{\langle \alpha, n | V | \beta, l \rangle \langle \beta, l | V | \alpha, m \rangle}{E_\alpha - E_\beta}. \quad (2.7)$$

The first order term accounts for the direct perturbation overlap between states within the same group. The second order term captures the indirect effect of states from other groups, via virtual transitions and back, weighted by the corresponding energy difference.

For the TFI Hamiltonians $H(g \gg J)$ and $H(g \ll J)$ with periodic boundary conditions, we separate the single quasiparticle excitations $\{|n\rangle\}$ from the vacuum ground state $|0\rangle$ below and the two particle states $\{|n, m\rangle\}$ above. We then compute the effective Hamiltonians (2.7) for small perturbations JV and gV , which all describe a single particle on a lattice with on-site energy μ and nearest-neighbor hopping t :

$$H_{\text{eff}} = \mu \sum_n |n\rangle \langle n| - t \sum_{\langle n, m \rangle} (|n\rangle \langle m| + |m\rangle \langle n|). \quad (2.8)$$

Diagonalization is easily achieved by Fourier transformation $|n\rangle = \frac{1}{\sqrt{N}} \sum_p e^{-ip \cdot n} |p\rangle$:

$$H_{\text{eff}} = \sum_p \epsilon_p |p\rangle \langle p|, \quad (2.9)$$

with $\epsilon_p = \mu - 2t \cos(p)$ in one dimension and $\epsilon_p = \mu - 2t [\cos(p_x) + \cos(p_y)]$ in two dimensions.

In the following we denote with $\Delta_\alpha = E_\alpha - E_0$ the unperturbed energy of group α above the ground state.

$$\underline{\underline{g \gg J}}: H^0 = -g \sum_n \sigma_n^z, \lambda = J, V = - \sum_{\langle n,m \rangle} \sigma_n^x \sigma_m^x.$$

- 0) Unique zero particle ground state $|0\rangle = |\uparrow \dots \uparrow\rangle,$
- 1) N single particle states $|n\rangle = |\uparrow \dots \uparrow \downarrow_n \uparrow \dots \uparrow\rangle$ with $\Delta_1 = 2g,$
- 2) $N(N-1)/2$ two particle scattering states $|n, m\rangle = |\uparrow \dots \uparrow \downarrow_n \uparrow \dots \uparrow \downarrow_m \uparrow \dots \uparrow\rangle$ with $\Delta_2 = 4g.$

$$\mathcal{O}(J): J \langle n | V | m \rangle = -J \text{ for } n, m \text{ nearest neighbors and 0 else} \rightsquigarrow \mu = \Delta_1, t = J.$$

$$\text{One dimension : } \epsilon_p = 2g - 2J \cos(p) + \mathcal{O}(J^2), \quad (2.10)$$

$$\text{Two dimensions : } \epsilon_p = 2g - 2J [\cos(p_x) + \cos(p_y)] + \mathcal{O}(J^2). \quad (2.11)$$

$$\underline{\underline{\underline{g \ll J}}}: H^0 = -J \sum_{\langle n,m \rangle} \sigma_n^x \sigma_m^x, \lambda = g, V = - \sum_n \sigma_n^z.$$

In this limit, qualitatively different lowest excitations emerge for the different spatial dimensions, so we treat them as separate cases.

One dimension

- 0) Zero particle ground state $|0\rangle = |\rightarrow \dots \rightarrow\rangle$ or $|0\rangle = |\leftarrow \dots \leftarrow\rangle,$
- 1) N single¹ domain wall states $|n\rangle = |\rightarrow \dots \rightarrow \downarrow_n \dots \leftarrow \dots \leftarrow\rangle$ with $\Delta_1 = 2J,$
- 2) $N(N-1)/2$ two domain wall scattering states $|n, m\rangle = |\rightarrow \dots \rightarrow \downarrow_n \dots \leftarrow_m \rightarrow \dots \rightarrow\rangle$ with $\Delta_2 = 4J.$

$$\mathcal{O}(g): g \langle n | V | m \rangle = -g \text{ for } n, m \text{ nearest neighbors and 0 else} \rightsquigarrow \mu = \Delta_1, t = g.$$

$$\Rightarrow \epsilon_p = 2J - 2g \cos(p) + \mathcal{O}(g^2). \quad (2.12)$$

Two dimensions

- 0) Zero particle ground state $\begin{array}{cccccccccc} \rightarrow & \rightarrow & \rightarrow & \rightarrow & & \leftarrow & \leftarrow & \leftarrow & \leftarrow \\ \rightarrow & \rightarrow & \rightarrow & \rightarrow & \text{or} & \leftarrow & \leftarrow & \leftarrow & \leftarrow \\ \rightarrow & \rightarrow & \rightarrow & \rightarrow & & \leftarrow & \leftarrow & \leftarrow & \leftarrow \\ \rightarrow & \rightarrow & \rightarrow & \rightarrow & & \leftarrow & \leftarrow & \leftarrow & \leftarrow \end{array},$
- 1) N single particle states $\begin{array}{ccccccccc} \rightarrow & \rightarrow & \rightarrow & \rightarrow \\ \rightarrow & \leftarrow & \rightarrow & \rightarrow \\ \rightarrow & \rightarrow & \rightarrow & \rightarrow \\ \rightarrow & \rightarrow & \rightarrow & \rightarrow \end{array}$ with $\Delta_1 = 8J,$

¹Strictly speaking, for PBC domain walls always come in pairs. But they are really independent excitations and so we treat them as individually existing particles here.

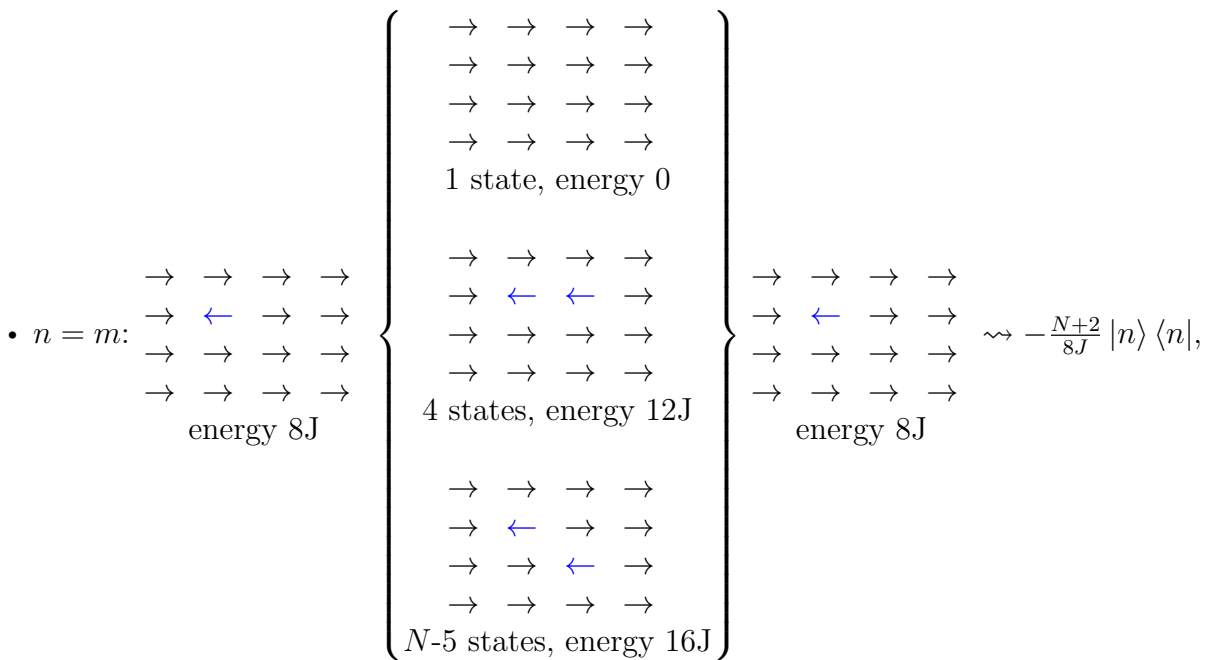
2) $2N$ nearest-neighbor bound states $\rightarrow \rightarrow \rightarrow \rightarrow \rightarrow \rightarrow \rightarrow \rightarrow$
 $\rightarrow \leftarrow \leftarrow \rightarrow \rightarrow \leftarrow \rightarrow \rightarrow$, with $\Delta_2 = 12J$,
 $\rightarrow \rightarrow \rightarrow \rightarrow \rightarrow \leftarrow \rightarrow \rightarrow$
 $\rightarrow \rightarrow \rightarrow \rightarrow \rightarrow \rightarrow \rightarrow \rightarrow$

3) $N(N - 1)/2 - 2N$ two particle scattering states $\rightarrow \rightarrow \rightarrow \rightarrow$
 $\rightarrow \leftarrow \rightarrow \rightarrow$, with $\Delta_3 = 16J$.²
 $\rightarrow \rightarrow \leftarrow \rightarrow$
 $\rightarrow \rightarrow \rightarrow \rightarrow$

$\mathcal{O}(g)$: The perturbation V brings the single particle states out of their degenerate subspace, so there is no nonzero matrix element in first order.

$\mathcal{O}(g^2)$: By drawing one representative of each (sub)group β and multiplying with the number of equivalent states, we diagrammatically calculate the matrix elements

$$\sum_{\beta=0,2,3} \sum_l \frac{\langle n | V | \beta, l \rangle \langle \beta, l | V | m \rangle}{8J - E_\beta}. \quad (2.13)$$



²The three particle bound states with energy $\Delta_4 = 14$ lie below the two particle scattering states. But since they have no overlap with the single particle states up to second order, we do not consider them here.

- $|n - m| = 1$:

$$\begin{array}{cccc} \rightarrow & \rightarrow & \rightarrow & \rightarrow \\ \rightarrow & \leftarrow & \rightarrow & \rightarrow \\ \rightarrow & \rightarrow & \rightarrow & \rightarrow \\ \rightarrow & \rightarrow & \rightarrow & \rightarrow \end{array}$$

energy 8J

$\left\{ \begin{array}{c} \rightarrow \rightarrow \rightarrow \rightarrow \\ \text{1 state, energy 0} \\ \rightarrow \rightarrow \rightarrow \rightarrow \\ \rightarrow \leftarrow \leftarrow \rightarrow \\ \rightarrow \rightarrow \rightarrow \rightarrow \\ \rightarrow \rightarrow \rightarrow \rightarrow \end{array} \right\}$

$\rightsquigarrow -\frac{1}{8J} |n\rangle \langle m|,$

$\left\{ \begin{array}{c} \rightarrow \rightarrow \rightarrow \rightarrow \\ \rightarrow \rightarrow \leftarrow \rightarrow \\ \rightarrow \rightarrow \rightarrow \rightarrow \\ \rightarrow \rightarrow \rightarrow \rightarrow \\ \text{energy 8J} \\ \rightarrow \rightarrow \rightarrow \rightarrow \\ \rightarrow \rightarrow \rightarrow \rightarrow \\ \rightarrow \rightarrow \rightarrow \rightarrow \end{array} \right\}$
- $|n - m| > 1$:

$$\begin{array}{cccc} \rightarrow & \rightarrow & \rightarrow & \rightarrow \\ \rightarrow & \leftarrow & \rightarrow & \rightarrow \\ \rightarrow & \rightarrow & \rightarrow & \rightarrow \\ \rightarrow & \rightarrow & \rightarrow & \rightarrow \end{array}$$

energy 8J

$\left\{ \begin{array}{c} \rightarrow \rightarrow \rightarrow \rightarrow \\ \text{1 state, energy 0} \\ \uparrow \\ \text{cancel each other} \\ \downarrow \\ \rightarrow \rightarrow \rightarrow \rightarrow \\ \rightarrow \leftarrow \rightarrow \rightarrow \\ \rightarrow \rightarrow \leftarrow \rightarrow \\ \rightarrow \rightarrow \rightarrow \rightarrow \\ \text{1 state, energy 16J} \end{array} \right\}$

$\rightsquigarrow 0.$

$\left\{ \begin{array}{c} \rightarrow \rightarrow \rightarrow \rightarrow \\ \rightarrow \rightarrow \rightarrow \rightarrow \\ \rightarrow \rightarrow \leftarrow \rightarrow \\ \rightarrow \rightarrow \rightarrow \rightarrow \\ \text{energy 8J} \\ \rightarrow \rightarrow \rightarrow \rightarrow \\ \rightarrow \rightarrow \rightarrow \rightarrow \\ \rightarrow \rightarrow \rightarrow \rightarrow \end{array} \right\}$

Note that in second order also the ground state energy is shifted.

- ground state: $\begin{array}{cccc} \rightarrow & \rightarrow & \rightarrow & \rightarrow \\ \rightarrow & \rightarrow & \rightarrow & \rightarrow \\ \rightarrow & \rightarrow & \rightarrow & \rightarrow \end{array} \left\{ \begin{array}{cccc} \rightarrow & \rightarrow & \rightarrow & \rightarrow \\ \rightarrow & \leftarrow & \rightarrow & \rightarrow \\ \rightarrow & \rightarrow & \rightarrow & \rightarrow \\ \rightarrow & \rightarrow & \rightarrow & \rightarrow \end{array} \right\} \begin{array}{cccc} \rightarrow & \rightarrow & \rightarrow & \rightarrow \\ \rightarrow & \rightarrow & \rightarrow & \rightarrow \\ \rightarrow & \rightarrow & \rightarrow & \rightarrow \end{array} \rightsquigarrow -\frac{N}{8J}$.
 $\begin{array}{c} \text{energy 0} \\ | \\ N \text{ states, energy } 8J \\ | \\ \text{energy 0} \end{array}$

\rightsquigarrow We subtract $-N/(8J)$ as an energy offset and end up with $\mu = \Delta_1 - g^2/(4J)$, $t = g^2/(8J)$.

$$\Rightarrow \epsilon_p = 8J - \frac{g^2}{4J}[1 + \cos(p_x) + \cos(p_y)] + \mathcal{O}(g^3). \quad (2.14)$$

At this point a comment about the spontaneous symmetry breaking for $g \ll J$ is in order. If we pushed the perturbation theory up to N -th order for finite N , the degeneracy between the symmetric ground states $\frac{1}{\sqrt{2}}(|\Rightarrow\rangle \pm |\Leftarrow\rangle)$ would be lifted by an exponentially small energy splitting $\delta E_{\pm} = \mathcal{O}(g^N)$. SSB is thus restricted to the thermodynamic limit $N \rightarrow \infty$, where there is no tunneling matrix element between $|\Rightarrow\rangle$ and $|\Leftarrow\rangle$ at any finite order in g . We will see in section 5.2 that DMRG is able to detect the energy splitting δE_{+} for small enough N .

2.3 Exact solution in one dimension

In one dimension, the spectrum of the TFI model is exactly solvable for all values of g . The Hamiltonian (2.1) with periodic boundary conditions (PBC) $\sigma_{N+1}^x \equiv \sigma_1^x$ is

$$H = -J \sum_{n=1}^N \sigma_n^x \sigma_{n+1}^x - g \sum_{n=1}^N \sigma_n^z. \quad (2.15)$$

We show the detailed calculations in appendix A, and only summarize the three fundamental steps here [Pfe70, Sac11]:

- 1) *Jordan-Wigner transformation*—Mapping spin-1/2 degrees of freedom to spinless fermions.

$$\sigma_n^z = 1 - 2c_n^\dagger c_n \text{ and } \sigma_n^x = \eta_n(c_n^\dagger + c_n), \quad (2.16)$$

where $\eta_n = \prod_{m < n} (1 - 2c_m^\dagger c_m)$ is the non-local Jordan-Wigner string. The Hamiltonian block diagonalizes into sectors of even/odd fermion parity,

$$P_f = (-1)^{N_f} = (-1)^{\sum_n c_n^\dagger c_n} = \prod_n \sigma_n^z, \quad (2.17)$$

when we impose anti-periodic boundary conditions $c_{N+1} = -c_1$ for $P_f = 1$ and periodic boundary conditions $c_{N+1} = c_1$ for $P_f = -1$.

- 2) *Fourier transformation*—Going to momentum space.

$$c_n = \frac{1}{\sqrt{N}} \sum_p e^{-ipn} c_p, \quad (2.18)$$

for momenta $p = \frac{2\pi}{N}k$ with k quantized to half-integers for $P_f = 1$ and to integers for $P_f = -1$.

- 3) *Bogoliubov transformation*—Diagonalizing the quadratic Hamiltonian.

$$\gamma_p = u_p c_p - i v_p c_p^\dagger, \quad (2.19)$$

where $u_p = \cos\left(\frac{\vartheta_p}{2}\right)$, $v_p = \sin\left(\frac{\vartheta_p}{2}\right)$ and $\tan(\vartheta_p) = -\frac{J \sin(p)}{g - J \cos(p)}$.

The final Hamiltonian in terms of fermionic creation and annihilation operators reads

$$H = E_0 + \sum_p \epsilon_p \gamma_p^\dagger \gamma_p \text{ with } \epsilon_p = 2\sqrt{g^2 - 2Jg \cos(p) + J^2}. \quad (2.20)$$

The ground state with energy $E_0 = -\sum_p \epsilon_p / 2$ is given by the vacuum $|0\rangle$ satisfying $\gamma_p |0\rangle = 0$ for all p . A single excitation with energy ϵ_p is created above by adding a fermion with corresponding momentum: $|p\rangle = \gamma_p^\dagger |0\rangle$. In a general M -particle state $\gamma_{p_1}^\dagger \cdots \gamma_{p_M}^\dagger |0\rangle$, the fermions occupy M distinct single particle states and their total energy adds up to $\sum_{m=1}^M \epsilon_{p_m}$.

Note that the exact dispersion relation ϵ_p agrees with the perturbative ones for large (2.10) and small (2.12) g/J . For the transition between these limits, the exact solution adds a valuable insight. The energy gap ϵ_0 closes at $g_c = J$, which quantitatively locates the critical point.

Chapter 3

Tensor network basics

We define a *tensor* as a multi-dimensional array of complex numbers, $A \in \mathbb{C}^{D_1 \times \dots \times D_r}$, where r is called the *rank* of the tensor. Graphically, we represent a tensor as a geometric shape with one *leg* attached for each index $\alpha_1, \dots, \alpha_r$. There are three fundamental tensor operations:

- *Transposition*: Permuting the indices.
- *Reshaping*: Merging or splitting legs. In particular, *matricization* means dividing the legs into two groups, *vectorization* means combining all legs into a single one. In analogy to the bracket notation for physical states, we denote vectorized tensors by $|A\rangle$. The corresponding $(A|$ denotes its transpose, but without implicit complex conjugation: $(A| = |A\rangle^T$. This aligns with how tensors are stored and manipulated computationally.
- *Contraction*: Connecting equal-dimensional legs of two tensors by summing over the corresponding indices and multiplying the tensor elements:

$$\alpha_1 - \boxed{AX} - \alpha_4 = \alpha_1 - \boxed{A} - \boxed{X} - \alpha_4 = \sum_{\alpha_3} A_{\alpha_1, \alpha_2, \alpha_3} X_{\alpha_3, \alpha_4}. \quad (3.1)$$

The *computational time complexity* is $\mathcal{O}[\dim(\text{contracted legs}) \times \dim(\text{open legs})]$. A *tensor network* is an arrangement of multiple tensors contracted with each other. The total contraction complexity can heavily depend on the pairwise contraction order. We draw a single outer shape for a tensor resulting from contractions described in its inside via diagrams or equations. The latter can be implicit about the legs being contracted, such as AX in (3.1).

For two tensors of equal *shape* (D_1, \dots, D_r) , we define the general *tensor inner product* as

$$(A, B)_2 = \sum_{\alpha_1, \dots, \alpha_r} \overline{A}_{\alpha_1, \dots, \alpha_r} B_{\alpha_1, \dots, \alpha_r}, \quad (3.2)$$

where the overline denotes complex conjugation. This coincides with the *Hermitian inner product* $(\overline{A}|B)$ for vectors and the *Frobenius inner product* $\text{tr}[A^\dagger B]$ for matrices. The induced norm is given by

$$\|A\|_2 = \sqrt{(A, A)_2} = \left(\sum_{\alpha_1, \dots, \alpha_r} |A_{\alpha_1, \dots, \alpha_r}|^2 \right)^{1/2}. \quad (3.3)$$

We call a tensor *left/right isometric* if it can be reshaped into a matrix A_L/A_R with orthonormal columns/rows, i.e. if $A_L^\dagger A_L = \mathbb{1}/A_R^\dagger A_R = \mathbb{1}$. We introduce ingoing and outgoing arrows on the legs such that the contraction of an isometric tensor with its complex conjugate over all ingoing legs yields the identity over all outgoing legs. The total Hilbert space dimension of the

ingoing legs must be greater than or equal to that of the outgoing legs to permit an isometric map. For example, for $A_L, A_R \in \mathbb{C}^{D \times d \times D}$:

$$\begin{array}{c} \text{Diagram showing } A_L \text{ and } \bar{A}_L \text{ tensors with their legs labeled by arrows.} \\ = \quad [\quad , \quad \begin{array}{c} \text{Diagram showing } A_R \text{ and } \bar{A}_R \text{ tensors with their legs labeled by arrows.} \\ = \quad [\quad] \end{array} \end{array} \quad (3.4)$$

Any matrix $A \in \mathbb{C}^{M \times N}$ with $K = \min(M, N)$ admits the following standard decompositions involving isometric factors [HJ12]:

QR decomposition $A = QR$

$$[A] = \rightarrow [Q] \rightarrow [R]$$

$$\begin{aligned} Q &\in \mathbb{C}^{M \times K} \text{ left isometric } (Q^\dagger Q = \mathbb{1}) \\ R &\in \mathbb{C}^{K \times N} \text{ upper triangular } (R_{k,n} = 0 \text{ for } k > n) \end{aligned} \quad (3.5)$$

The computational runtime complexity scales as $\mathcal{O}(MKN)$. If A has full rank, the decomposition can be made unique by ensuring that all main diagonal entries of R are positive. Applying the QR decomposition to A^T and transposing back goes under the name *LQ decomposition*: $A = LQ$ with $L \in \mathbb{C}^{M \times K}$ lower triangular ($L_{m,k} = 0$ for $k > m$) and $Q \in \mathbb{C}^{K \times N}$ right isometric ($QQ^\dagger = \mathbb{1}$).

Singular value decomposition (SVD) $A = USV$

$$[A] = \rightarrow [U] \rightarrow [S] \leftarrow [V]$$

$$U \in \mathbb{C}^{M \times K} \text{ left isometric } (U^\dagger U = \mathbb{1})$$

$$S \in \mathbb{R}^{K \times K} \text{ diagonal, positive semidefinite, nonincreasing } (S_{k,k} \equiv S_k \geq S_{k+1} \geq 0) \quad (3.6)$$

$$V \in \mathbb{C}^{K \times N} \text{ right isometric } (VV^\dagger = \mathbb{1})$$

The rank of A is equal to the number of nonzero *singular values* $S_k > 0$. Let us assume that this is K . We can define a *truncation* of A by keeping only the largest $D < K$ singular values:

$$\tilde{A} = \tilde{U} \tilde{S} \tilde{V} \text{ with } \tilde{U} = U_{[:,D]}, \tilde{S} = S_{[:D,:D]}, \tilde{V} = V_{[:D,:]} \quad (3.7)$$

It can be proven that this is the best rank- D approximation to A , with minimal *truncation error*

$$\varepsilon_{\text{trunc}} = \|\tilde{A} - A\|_2 = \left(\sum_{k>D} S_k^2 \right)^{1/2}. \quad (3.8)$$

As the QR decomposition (but with a larger prefactor), the computational runtime complexity scales as $\mathcal{O}(MKN)$.

Polar decomposition $A = UP$

$$[A] = \rightarrow [U] \rightarrow [P] \diagup \leftarrow [U] \leftarrow [P]$$

$$U \in \mathbb{C}^{M \times N} \text{ left isometric } (U^\dagger U = \mathbb{1}) \text{ if } M \geq N, \text{ right isometric } (UU^\dagger = \mathbb{1}) \text{ if } M \leq N \quad (3.9)$$

$$P \in \mathbb{C}^{N \times N} \text{ positive semidefinite}$$

We refer to this as the *right polar decomposition*. A *left polar decomposition* is obtained by applying a right polar decomposition to A^T and transposing back: $A = PU$, where $P \in \mathbb{C}^{M \times M}$ is positive semidefinite, and U again satisfies isometric conditions depending on the relative dimensions. Note that the polar decompositions can be easily derived from the singular value decomposition: Given $A = \tilde{U}\tilde{S}\tilde{V}$, we insert an identity $\tilde{V}\tilde{V}^\dagger$ or $\tilde{U}^\dagger\tilde{U}$ to get

$$A = \underbrace{(\tilde{U}\tilde{V})}_{U} \underbrace{(\tilde{V}^\dagger\tilde{S}\tilde{V})}_{P} \text{ or } A = \underbrace{(\tilde{U}\tilde{S}\tilde{U}^\dagger)}_{P} \underbrace{(\tilde{U}\tilde{V})}_{U}. \quad (3.10)$$

Variational tensor network states

A *tensor network state* is a (high dimensional) quantum many body vector $|\psi\rangle \in \mathcal{H}$ decomposed into a network of (lower dimensional) tensors. For approximating ground states and lowest-lying excited states of a Hamiltonian H with tensor network states, we deal with minimization problems of the form

$$\arg \min_X \frac{\langle \psi(\bar{X}) | H | \psi(X) \rangle}{\langle \psi(\bar{X}) | \psi(X) \rangle}, \quad (3.11)$$

where we optimize over one single tensor X of the network (while keeping all the others fixed). To enforce normalization of $|\psi(X)\rangle$, we introduce a Lagrange multiplier λ and minimize the energy functional

$$F(X, \bar{X}, \lambda) = \langle \psi(\bar{X}) | H | \psi(X) \rangle - \lambda [\langle \psi(\bar{X}) | \psi(X) \rangle - 1]. \quad (3.12)$$

Taking the derivative with respect to all components of \bar{X} , we obtain the stationary condition

$$\partial_{\bar{X}} \langle \psi(\bar{X}) | H | \psi(X) \rangle - \lambda \partial_{\bar{X}} \langle \psi(\bar{X}) | \psi(X) \rangle = 0. \quad (3.13)$$

We now introduce the *effective Hamiltonian matrix*

$$H_{\text{eff}} = \partial_X \partial_{\bar{X}} \langle \psi(\bar{X}) | H | \psi(X) \rangle, \quad (3.14)$$

and the *norm matrix*

$$N = \partial_X \partial_{\bar{X}} \langle \psi(\bar{X}) | \psi(X) \rangle, \quad (3.15)$$

whose networks are obtained by removing the tensors X, \bar{X} from the networks $\langle \psi(\bar{X}) | H | \psi(X) \rangle$ and $\langle \psi(\bar{X}) | \psi(X) \rangle$. The optimal tensor X (rearranged as a vector) corresponds to the ground state of the generalized eigenvalue problem

$$H_{\text{eff}} |X\rangle = \lambda N |X\rangle. \quad (3.16)$$

Making sure that X is completely surrounded by isometric tensors in $|\psi(X)\rangle$, the power of *isometric tensor network states* is twofold. First, the norm matrix is just the identity matrix, so that the generalized eigenvalue problem reduces to a standard one. Second, local SVD truncations of X become globally optimal.

In practice, there is usually no need for building the matrix H_{eff} . Instead, one should only implement the matrix-vector multiplication $H_{\text{eff}} |X\rangle$, by finding an optimal contraction path for the action of H_{eff} on X on the tensor level. The ground state can then be efficiently computed using an iterative Lanczos method. [Orú14]

Chapter 4

Uniform matrix product states (uMPS)

4.1 Primitivity, the manifold and its tangent space

Our starting point is a single rank-3 tensor $A \in \mathbb{C}^{D \times d \times D}$, with one leg of *physical dimension* d and two legs of *virtual/bond dimension* D . Equivalently, one can see A as a set of d complex matrices A^s of dimension $D \times D$. Completely characterized by A , we define the *uniform matrix product state* (uMPS) in the thermodynamic limit as the translation invariant quantum state whose amplitude for orthonormal basis indices $\{s_n\}_{n \in \mathbb{Z}}$ is given by the infinite product of the respective matrices:

$$|\psi(A)\rangle = \sum_{\{s_n\}} (v_L| \prod_{n \in \mathbb{Z}} A^{s_n} |v_R) |\{s_n\}\rangle = \cdots - \boxed{A} - \boxed{A}^D - \boxed{A}^D - \boxed{A} - \boxed{A} - \cdots . \quad (4.1)$$

The boundary vectors $|v_L\rangle, |v_R\rangle \in \mathbb{C}^D$ ensure normalization and are specified later. [VHV19b]

Primitivity

The central object that occurs in all important computations—such as norm or local expectation values—is the *transfer matrix* defined as

$$T_A = \sum_{s=1}^d A^s \otimes \overline{A^s} = - \boxed{\begin{array}{c} A \\ \hline \overline{A} \end{array}} - . \quad (4.2)$$

Using the isomorphism $|\alpha, \beta\rangle \leftrightarrow |\alpha\rangle (\beta|$ between \mathbb{C}^{D^2} and $\mathbb{C}^{D \times D}$, with the relation

$$(\gamma, \delta| T_A | \alpha, \beta) = (\gamma| \mathcal{E}_A(|\alpha\rangle (\beta|) | \delta), \quad (4.3)$$

we can see T_A as a matrix representation of the linear map $\mathcal{E}_A : \mathbb{C}^{D \times D} \rightarrow \mathbb{C}^{D \times D}$, mapping matrices X to

$$\mathcal{E}_A(X) = \sum_{s=1}^d A^s X A^{s\dagger} = - \boxed{\begin{array}{c} A \\ \hline X \\ \hline A^\dagger \end{array}} - . \quad (4.4)$$

This is known as the *Kraus representation* of a *completely positive*¹ map. If \mathcal{E}_A is in addition *trace preserving*, it describes a *quantum channel*, mapping density matrices to density matrices. In appendix B we elaborate on the relation between uMPS and quantum channels [Wol12]. In particular, on the crucial spectral property of *primitivity*. After having ensured that T_A has

¹A linear map $\mathcal{E} : \mathbb{C}^{D \times D} \rightarrow \mathbb{C}^{D \times D}$ is called *positive* if it maps positive semidefinite matrices to positive semidefinite matrices, i.e. if $\mathcal{E}(X) \geq 0$ for all $X \geq 0$. It is called *completely positive* if $\mathcal{E} \otimes \text{id}_n$ is positive for all $n \in \mathbb{N}$, where id_n is the identity map on $\mathbb{C}^{n \times n}$ such that $\mathcal{E} \otimes \text{id}_n : X \otimes Y \mapsto \mathcal{E}(X) \otimes Y$.

*spectral radius*² $\rho = 1$ (by rescaling $A \rightarrow A/\sqrt{\rho}$ if $\rho \neq 1$), we call T_A *primitive* if, counting algebraic multiplicities, there is only one dominant eigenvalue of magnitude and value 1 and the corresponding left and right eigenvectors r, l are positive definite and normalized to $\text{tr}[l^T r] = 1$:

$$T_A = |r| (l| + \mathcal{O}(|\lambda_2|)) \text{ with } |\lambda_2| < 1, r, l > 0 \text{ and } (l|r) = 1. \quad (4.5)$$

We prove in appendix B, that primitivity of T_A is equivalent to the existence of a finite *injectivity length* $L_0 \in \mathbb{N}$ such that for all $L \geq L_0$ the products $A^{s_1} \dots A^{s_L}$ span the whole space of $D \times D$ matrices:

$$\text{span}\{A^{s_1} \dots A^{s_L}\}_{s_1, \dots, s_L} = \mathbb{C}^{D \times D}. \quad (4.6)$$

For d randomly drawn matrices $\{A^s\}_{s=1}^d$, the dimension of $\text{span}\{A^{s_1} \dots A^{s_L}\}_{s_1, \dots, s_L}$ is expected to grow as d^L until it reaches D^2 . Therefore, a generic tensor is expected to be primitive with $L_0 \sim 2 \ln D / \ln d$, whereas non-primitive tensors appear with measure zero in the space $\mathbb{C}^{D \times d \times D}$. [PGVWC07]

Using (4.5), we can reduce the uMPS overlap to the overlaps of the boundary vectors with the fixed points of T_A :

$$\langle \psi(\overline{A}) | \psi(A) \rangle = (v_L, \overline{v_L}) \lim_{N \rightarrow \infty} T_A^N |v_R, \overline{v_R}\rangle = (v_L, \overline{v_L} | r)(l| v_R, \overline{v_R}) \stackrel{!}{=} 1. \quad (4.7)$$

We formally choose v_L and v_R such that these overlaps equal unity, but they don't have any effect on the bulk properties of $|\psi(A)\rangle$ and we will not mention them anymore in the following.

The manifold

There exists a *gauge freedom* in the choice of the tensor representation A of a physical state $|\psi(A)\rangle$. It is easy to convince oneself that the *similarity transformation* $B^s = S A^s S^{-1}$ ³, for any invertible matrix $S \in \mathbb{C}^{D \times D}$, leaves the uMPS invariant: $|\psi(A)\rangle = |\psi(B)\rangle$. It can be proven⁴ that this is in fact the only such transformation:

$$|\psi(A)\rangle = |\psi(B)\rangle \text{ if and only if } B^s = S A^s S^{-1} \text{ for } S \in \text{GL}(D, \mathbb{C}). \quad (4.8)$$

Since matrices S which are scalar multiples of the identity have a trivial effect, the effective *gauge group* is not the *general linear group* $\text{GL}(D, \mathbb{C})$ but the *projective general linear group* $\text{PGL}(D, \mathbb{C}) = \text{GL}(D, \mathbb{C})/\text{GL}(1, \mathbb{C})$. For fixed bond dimension D , the *complex manifold* of primitive tensors modulo gauge is then given by

$$\mathcal{A}_D = \{A \in \mathbb{C}^{D \times d \times D} \mid T_A \text{ is primitive}\}/\text{PGL}(D, \mathbb{C}). \quad (4.9)$$

The primitivity property ensures that this quotient space is *biholomorphic*⁵ to the corresponding set of uMPS,

$$\mathcal{M}_D = \{|\psi(A)\rangle \in \mathcal{H} \mid A \in \mathcal{A}_D\}, \quad (4.10)$$

²The spectral radius is defined as $\rho = \max\{|\lambda| \mid T_A |X\rangle = \lambda |X\rangle \text{ for some nonzero } X \in \mathbb{C}^{D \times D}\}$.

³With a slight abuse of notation, we often denote the matrix-wise similarity transformation $S A^s S^{-1}$ for all s as $S A S^{-1}$.

⁴and with the *fundamental theorem* B.3 we do, but under the assumption of primitivity and unitality, which requires S to be unitary.

⁵A map between complex manifolds is *biholomorphic* if it is a bijective holomorphic map whose inverse is also holomorphic.

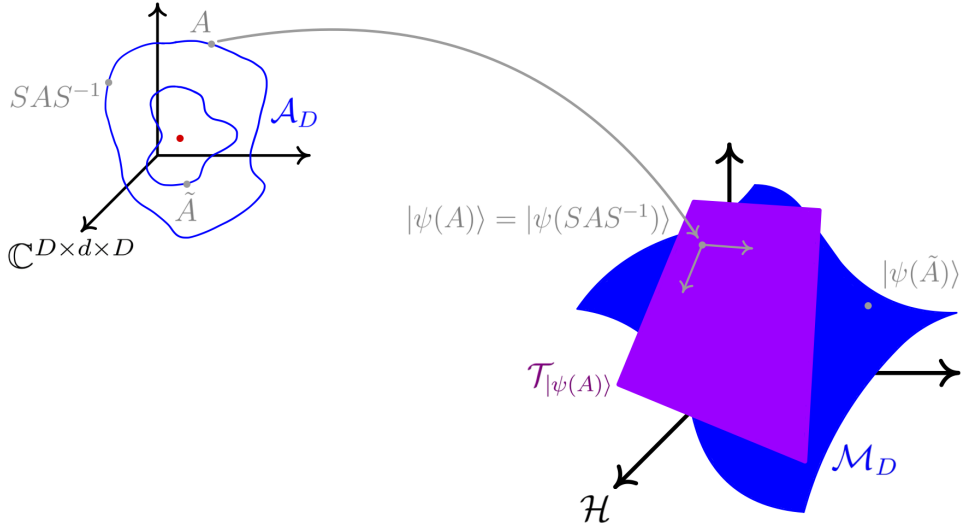


Figure 4.1: Illustration of the uMPS manifold and its tangent space. Tensors from parameter space $\mathbb{C}^{D \times d \times D}$ are mapped to physical states in Hilbert space \mathcal{H} . The actual tensor manifold \mathcal{A}_D is defined modulo gauge orbits. The red dot in the middle corresponds to a tensor of measure zero whose transfer matrix is not primitive. It has to be excluded from \mathcal{A}_D to define a so called *principal fiber bundle*. The uniform matrix product states then form a smooth, nonlinear manifold \mathcal{M}_D within the Hilbert space. To each point $|\psi(A)\rangle$ we can assign a linear tangent space $\mathcal{T}_{|\psi(A)\rangle}$ consisting of all states obtained by infinitesimal variations $|\psi(B; A)\rangle$. [HMOV14, HOV13]

turning it into a smooth, low-dimensional manifold in the exponentially large Hilbert space \mathcal{H} of d -dimensional spins on an infinite chain. We will see in the next section 4.2 that within \mathcal{M}_D we can faithfully approximate ground states of local, gapped Hamiltonians.

The tangent space

Since the sum of two uMPS with bond dimension D clearly does not remain within \mathcal{M}_D , the manifold \mathcal{M}_D is non-linear. However, as for any smooth manifold, we can assign a linear *tangent space* $\mathcal{T}_{|\psi(A)\rangle}$ to each point $|\psi(A)\rangle \in \mathcal{M}_D$. It consists of all states obtained by infinitesimal variations of the tensor A :

$$|\psi(B; A)\rangle = \sum_{\alpha, s, \beta} B_{\alpha, \beta}^s [\partial_{A_{\alpha, \beta}^s} |\psi(A)\rangle] = \sum_n \cdots \underbrace{[A]}_n \cdots \underbrace{[B]}_n \cdots \quad (4.11)$$

In section 4.4 this will be the space in which the quasiparticle excitations on top of the ground state vacuum live. In figure 4.1 we illustrate the mapping of tensors to uMPS, the manifold and its tangent space. [HMOV14, HOV13]

4.2 Intrinsic canonical form and area law

Within the gauge freedom SAS^{-1} , we want to bring the uMPS (4.1) into a *canonical form* that ensures orthonormality in a bipartition and numerical stability in the variational algorithms of sections 4.3, 4.4.

Canonical form

More precisely, we want to find invertible $L, R \in \mathbb{C}^{D \times D}$ such that

$$A_L = L A L^{-1} \text{ is left isometric: } (\mathbb{1}| T_{A_L} = (\mathbb{1}|, \quad (4.12)$$

$$A_R = R^{-1} A R \text{ is right isometric: } T_{A_R} |\mathbb{1}\rangle = |\mathbb{1}\rangle. \quad (4.13)$$

At this point it is useful to introduce the *dual map* \mathcal{E}_A^* of (4.4), which is defined via $\text{tr}[\mathcal{E}_A(X)Y] = \text{tr}[X\mathcal{E}_A^*(Y)]$ for all $X, Y \in \mathbb{C}^{D \times D}$. It has the Kraus representation

$$\mathcal{E}_A^*(Y) = \sum_{s=1}^d A^{s\dagger} Y A^s, \quad (4.14)$$

and the matrix representation T_A^\dagger , so that $T_A^\dagger |Y\rangle = |\mathcal{E}_A^*(Y)\rangle$. With our transpose-only bra notation this corresponds to $(Y| T_A = (\mathcal{E}_A^*(\bar{Y})|)$. From this we can conclude for the left fixed point l :

$$(l| T_A = (l| \text{ if and only if } \mathcal{E}_A^*(\bar{l}) = \bar{l}. \quad (4.15)$$

Since \bar{l} is positive definite, we can take its square root and the inverse thereof. Knowing this we define

$$A_L = \bar{l}^{1/2} A \bar{l}^{-1/2} \text{ to fulfill } \mathcal{E}_{A_L}^*(\mathbb{1}) = \sum_s A_L^{s\dagger} A_L^s = \bar{l}^{-1/2} \left(\sum_s A^{s\dagger} \bar{l} A^s \right) \bar{l}^{-1/2} = \mathbb{1}. \quad (4.16)$$

Similarly, we can take square root and inverse of the positive definite right fixed point r and define

$$A_R = r^{-1/2} A r^{1/2} \text{ to fulfill } \mathcal{E}_{A_R}^*(\mathbb{1}) = \sum_s A_R^{s\dagger} A_R^s = r^{-1/2} \left(\sum_s A^s r A^{s\dagger} \right) r^{-1/2} = \mathbb{1}. \quad (4.17)$$

In practice, computing A_L and A_R according to (4.16) and (4.17) is suboptimal due to a potentially ill-conditioned inversion of small eigenvalues of $\bar{l}^{1/2}$ and $r^{1/2}$. Instead, we iteratively solve the equations $LA = A_L L$ and $AR = RA_R$ with QR and LQ decompositions. Making the decompositions unique (by ensuring positive values on the main diagonal of the triangular matrices), we can reach convergence up to arbitrary tolerance tol:

$$\begin{array}{c} \boxed{L^{(i)}} \xrightarrow{\quad} \boxed{A} \xrightarrow{\quad} \\ \downarrow \end{array} \stackrel{\text{QR}}{\equiv} \rightarrow \begin{array}{c} \boxed{A_L^{(i+1)}} \xrightarrow{\quad} \boxed{L^{(i+1)}} \xrightarrow{\quad} \\ \downarrow \end{array} \text{ until } \|L^{(i+1)} - L^{(i)}\|_2 < \text{tol}, \quad (4.18)$$

$$\begin{array}{c} \boxed{A} \xrightarrow{\quad} \boxed{R^{(i)}} \xrightarrow{\quad} \\ \downarrow \end{array} \stackrel{\text{LQ}}{\equiv} \leftarrow \begin{array}{c} \boxed{R^{(i+1)}} \xleftarrow{\quad} \boxed{A_R^{(i+1)}} \xleftarrow{\quad} \\ \downarrow \end{array} \text{ until } \|R^{(i+1)} - R^{(i)}\|_2 < \text{tol}. \quad (4.19)$$

For any bond n in the uMPS, we can install the left isometric gauge (4.12) for all tensors on the left and the right isometric gauge (4.13) for all tensors on the right. It remains a *center matrix* $C = LR$ at the chosen bond, that relates A_L and A_R via $A_L C = L A R = C A_R$. We decompose C with an SVD into $C = USV$ and redefine $C \rightarrow S/\|S\|_2$, which normalizes the uMPS

and makes the center matrix diagonal positive definite. The isometric tensors are accordingly redefined as $A_L \rightarrow U^\dagger A_L U$ and $A_R \rightarrow V A_R V^\dagger$. Since both U and V are unitary matrices, i.e. satisfy $U^\dagger U = UU^\dagger = \mathbb{1}$, $VV^\dagger = V^\dagger V = \mathbb{1}$, all desired properties are preserved. Sometimes it is useful to summarize A_L and C (or equivalently C and A_R) into a normalized *center tensor* A_C .

In total, we derived the following *canonical form* for a uMPS $|\psi(A)\rangle \in \mathcal{M}_D$:

$$\begin{aligned}
|\psi(A)\rangle &= \cdots \rightarrow \boxed{A_L} \rightarrow \boxed{A_L} \xrightarrow{n} \boxed{A_C} \xleftarrow{n} \boxed{A_R} \leftarrow \boxed{A_R} \leftarrow \cdots \\
&= \cdots \rightarrow \boxed{A_L} \rightarrow \boxed{A_L} \xrightarrow{n} \boxed{A_L} \rightarrow \boxed{C} \xleftarrow{n} \boxed{A_R} \leftarrow \boxed{A_R} \leftarrow \cdots \\
&= \cdots \rightarrow \boxed{A_L} \rightarrow \boxed{A_L} \xrightarrow{n} \boxed{C} \leftarrow \boxed{A_R} \xleftarrow{n} \boxed{A_R} \leftarrow \cdots
\end{aligned} \tag{4.20}$$

In practice, the four tensors A_L , A_R , C and A_C are the central attributes of a uMPS class.

Area law

As a first application of the canonical form, we want to investigate the role of the bond dimension D . We can see (4.20) as a bipartition between all spins on the left and on the right of bond n :

$$|\psi(A)\rangle = \sum_{\alpha=1}^D C_\alpha |\psi(A_L)_\alpha\rangle |\psi(A_R)_\alpha\rangle. \tag{4.21}$$

Since the states

$$|\psi(A_L)_\alpha\rangle = \cdots \rightarrow \boxed{A_L} \rightarrow \boxed{A_L} \rightarrow \alpha, \quad |\psi(A_R)_\alpha\rangle = \alpha \leftarrow \boxed{A_R} \leftarrow \boxed{A_R} \leftarrow \cdots \tag{4.22}$$

are orthonormal, i.e. $\langle \psi(\bar{A}_L)_\alpha | \psi(A_L)_\beta \rangle = \delta_{\alpha\beta}$, $\langle \psi(\bar{A}_R)_\alpha | \psi(A_R)_\beta \rangle = \delta_{\alpha\beta}$, this is nothing but a *Schmidt decomposition* with *Schmidt values* $C_\alpha > 0$ and *Schmidt rank* D . The reduced density matrix $\rho_L = \text{tr}_R |\psi(A)\rangle \langle \psi(\bar{A})|$ yields the *entanglement entropy*

$$S(\psi_A) = -\text{tr}[\rho_L \log \rho_L] = -\sum_{\alpha=1}^D C_\alpha^2 \log C_\alpha^2. \tag{4.23}$$

This shows that the bond dimension D controls the amount of entanglement in the uMPS. More precisely, it sets an upper bound for the bipartite entanglement entropy:

$$S(\psi_A) \leq \log D. \tag{4.24}$$

As we know, the full Hilbert space is exponentially large in the chain length N , and [Pag93] proved that a typical random state fulfills a *volume law* for the entanglement entropy:

$$S(\psi_{\text{random}}) \approx \frac{N}{2} \log d - \frac{1}{2}, \tag{4.25}$$

scaling extensively with the subsystem size $N/2$. The good news is that ground states of local, gapped Hamiltonians are very special and lie in a small corner of the Hilbert space. Proven by [Has07] and strengthened by [AKLV13], the entanglement entropy of these ground states scales with the area of the boundary between the two subsystems, which is a constant in one spatial dimension. This is called the *area law*:

$$S(\psi_0) \leq \mathcal{O}[(\log d)^3/\Delta], \quad (4.26)$$

where Δ denotes the energy gap above the ground state. The bounds (4.24) and (4.26) indicate: Ground states of local, gapped Hamiltonians can be faithfully approximated by uMPS with bond dimension $D = \mathcal{O}(e^{(\log d)^3/\Delta})$.

Conversely, in appendix B, we prove that for any $|\psi(A)\rangle \in \mathcal{M}_D$, we can define a local, *frustration free*⁶ Hamiltonian, of which $|\psi(A)\rangle$ is the exact, unique ground state. This Hamiltonian is called *parent Hamiltonian* and it can be shown to be gapped.

4.3 Variational uniform matrix product states (VUMPS)

We now present a variational algorithm [ZSVF⁺18] that minimizes the energy of a local Hamiltonian H within the manifold \mathcal{M}_D of uniform matrix product states:

$$\arg \min_{A \in \mathcal{A}_D} \frac{\langle \psi(\bar{A}) | H | \psi(A) \rangle}{\langle \psi(\bar{A}) | \psi(A) \rangle}. \quad (4.27)$$

We can rewrite the stationary condition (3.13) as

$$\partial_{\bar{A}} \langle \psi(\bar{A}) | (H - \lambda) | \psi(A) \rangle = 0. \quad (4.28)$$

For a variational optimum $|\psi(A)\rangle$ with energy $\lambda = \langle \psi(\bar{A}) | H | \psi(A) \rangle$, (4.28) forces the residual $(H - \lambda) |\psi(A)\rangle$ of the full Schrödinger equation—which is not exactly solvable within the manifold—to be orthogonal to the space spanned by the states $\partial_A |\psi(A)\rangle$, which is equal to the tangent space $\mathcal{T}_{|\psi(A)\rangle}$. Denoting with $P_{\mathcal{T}_{|\psi(A)\rangle}}$ the projector onto the tangent space at point $|\psi(A)\rangle$, (4.28) can be reformulated as the projective Schrödinger equation

$$P_{\mathcal{T}_{|\psi(A)\rangle}} (H - \lambda) |\psi(A)\rangle = 0. \quad (4.29)$$

Projector onto tangent space

We derive a diagrammatic expression for $P_{\mathcal{T}_{|\psi(A)\rangle}}$. We do this in the canonical gauge (4.20). Our starting point is a tangent space vector $|\psi(B; A)\rangle$ in the left gauge, so equal to (4.11) but with A_L instead of A . For each state in the superposition, we bring all tensors on the right of site n into right isometric form. The remaining full rank matrix C can be absorbed into the (for now unnormalized) perturbation tensor B and we end up with

$$|\psi(B; A)\rangle = \sum_n \cdots \rightarrow \boxed{A_L} \rightarrow \boxed{A_L} \rightarrow \boxed{B} \xleftarrow{n} \boxed{A_R} \leftarrow \boxed{A_R} \leftarrow \cdots. \quad (4.30)$$

⁶In the sense that the ground state minimizes the energy locally for each term in the Hamiltonian.

For any $Y \in \mathbb{C}^{D \times D}$ this state is left invariant under the gauge transformation

$$B \rightarrow B + A_L Y - Y A_R. \quad (4.31)$$

We fix the D^2 gauge parameters by the effective parametrization

$$\begin{array}{c} \text{---} \boxed{B} \text{---} \\ | \end{array} = \begin{array}{c} \text{---} \boxed{V_L} \text{---} \xrightarrow{D(d-1)} \boxed{X}^D \\ \downarrow d \end{array} \quad \text{with} \quad \begin{array}{c} \text{---} \boxed{V_L} \text{---} \\ | \quad \downarrow \\ | \quad \uparrow \\ \text{---} \boxed{\bar{A}_L} \text{---} \end{array} = 0. \quad (4.32)$$

This not only ensures that the tangent space vectors

$$|\psi(X; A)\rangle = \sum_n \dots \rightarrow \boxed{A_L} \xrightarrow{\downarrow} \boxed{A_L} \xrightarrow{\downarrow} \boxed{V_L} \xrightarrow{\downarrow} \boxed{X} \xleftarrow{\downarrow} \boxed{A_R} \xleftarrow{\downarrow} \boxed{A_R} \xleftarrow{\downarrow} \dots \quad (4.33)$$

are orthogonal to the original state $|\psi(A)\rangle$, but also that the overlap between two of them reduces to the overlap between the two parametrizations:

$$\langle\psi(\bar{Y}; \bar{A})|\psi(X; A)\rangle = |\mathbb{Z}|(\bar{Y}|X). \quad (4.34)$$

Finding the projection of an arbitrary translation invariant state in the Hilbert space, $|\varphi\rangle \in \mathcal{H}$, onto the tangent space of $|\psi(A)\rangle$, is equivalent to the following minimization problem:

$$\begin{aligned} \arg \min_X \| |\varphi\rangle - |\psi(X; A)\rangle \|^2 &= \arg \min_X [\langle\psi(\bar{X}; \bar{A})|\psi(X; A)\rangle - \langle\psi(\bar{X}; \bar{A})|\varphi\rangle \\ &\quad - \langle\varphi|\psi(X; A)\rangle + \langle\varphi|\varphi\rangle]. \end{aligned} \quad (4.35)$$

Setting the derivative of the square bracket with respect to \bar{X} to zero, we get the solution

$$X_\varphi = \partial_{\bar{X}} \langle\psi(\bar{X}; \bar{A})|\varphi\rangle / |\mathbb{Z}|. \quad (4.36)$$

The corresponding tangent space vector is

$$|\psi(X_\varphi; A)\rangle = P_{\mathcal{T}_{|\psi(A)\rangle}} |\varphi\rangle = \sum_n \dots \overbrace{\dots}^{\varphi} \begin{array}{c} \text{---} \boxed{\bar{A}_L} \text{---} \boxed{\bar{A}_L} \xrightarrow{\downarrow} \boxed{V_L} \xrightarrow{\downarrow} \dots \\ \dots \quad \dots \quad \dots \quad \dots \\ \text{---} \boxed{A_L} \text{---} \boxed{A_L} \xrightarrow{\downarrow} \boxed{V_L} \xrightarrow{\downarrow} \dots \\ \dots \quad \dots \quad \dots \quad \dots \end{array} \quad (4.37)$$

The columns of the matricized $A_L \in \mathbb{C}^{Dd \times D}$ and $V_L \in \mathbb{C}^{Dd \times D(d-1)}$ together form a unitary matrix. This allows us to insert

$$\begin{array}{c} \text{---} \boxed{\bar{V}_L} \text{---} \\ | \end{array} = \begin{array}{c} \text{---} \boxed{A_L} \text{---} \\ | \end{array} - \begin{array}{c} \text{---} \boxed{V_L} \text{---} \\ | \end{array}, \quad (4.38)$$

and draw the following final form of the tangent space projector:

$$P_{T_{|\psi(A)\rangle}} = \sum_n \left[\begin{array}{c} \cdots - \boxed{\bar{A}_L} - \boxed{\bar{A}_L} - \cdots \\ \cdots - \boxed{A_L} - \boxed{A_L} - \cdots \end{array} \right]_n \left| \begin{array}{c} \cdots - \boxed{\bar{A}_R} - \boxed{\bar{A}_R} - \cdots \\ \cdots - \boxed{A_R} - \boxed{A_R} - \cdots \end{array} \right| - \sum_n \left[\begin{array}{c} \cdots - \boxed{\bar{A}_L} - \boxed{\bar{A}_L} - \boxed{\bar{A}_L} - \cdots \\ \cdots - \boxed{A_L} - \boxed{A_L} - \boxed{A_L} - \cdots \end{array} \right]_n \left| \begin{array}{c} \cdots - \boxed{\bar{A}_R} - \boxed{\bar{A}_R} - \cdots \\ \cdots - \boxed{A_R} - \boxed{A_R} - \cdots \end{array} \right| . \quad (4.39)$$

Two-site Hamiltonian

Describing d -dimensional spins on an infinite chain, we assume that H is translational invariant and restricted to nearest-neighbor interaction:

$$H = \sum_{n \in \mathbb{Z}} h^{[n,n+1]} \text{ with } h^{[n,n+1]} = \cdots \mathbb{1} \otimes \mathbb{1} \otimes \underset{n, n+1}{h} \otimes \mathbb{1} \otimes \mathbb{1} \cdots, h = h^\dagger \in \mathbb{C}^{d^2 \times d^2}. \quad (4.40)$$

As an example for $d = 2$, we always have the transverse field Ising model (2.15) in mind, with

$$h = -J(\sigma^x \otimes \sigma^x) - \frac{g}{2}(\sigma^z \otimes \mathbb{1}) - \frac{g}{2}(\mathbb{1} \otimes \sigma^z). \quad (4.41)$$

Practically, we store h as a four leg tensor

$$\boxed{h} \in \mathbb{C}^{d \times d \times d \times d}. \quad (4.42)$$

Because of translation invariance and the isometric structure of the canonical form, the uMPS expectation value of H reduces to a local energy density e per lattice bond:

$$\langle \psi(\bar{A}) | H | \psi(A) \rangle = |\mathbb{Z}|e \text{ with } e = \boxed{h} \boxed{A_L} \boxed{A_C} \boxed{\bar{A}_L} \boxed{\bar{A}_C}. \quad (4.43)$$

VUMPS

We now solve the projected Schrödinger equation (4.29). Applying the Hamiltonian (4.40) and then the projector (4.39) to (4.20), gives the tangent space vector

$$P_{T_{|\psi(A)\rangle}} H | \psi(A) \rangle = | \psi(G; A) \rangle \text{ with } G = H_{\text{eff},1}(A_C) - A_L H_{\text{eff},0}(C). \quad (4.44)$$

The effective one site and zero site Hamiltonians act as

$$\boxed{H_{\text{eff},1}} = \boxed{L_h} + \boxed{h} \boxed{A_L} \boxed{A_C} \boxed{\bar{A}_L} + \boxed{h} \boxed{A_C} \boxed{A_R} \boxed{\bar{A}_R} + \boxed{R_h}, \quad (4.45)$$

(4.46)

All terms where h acts only on sites left/right of A_C or C , are additively summarized in the left/right boundary tensors

$$L_h = \begin{array}{c} \text{---} \\ | \quad | \\ \text{---} \end{array} = \begin{array}{c} A_L \quad A_L \\ | \quad | \\ h \\ | \quad | \\ \bar{A}_L \quad \bar{A}_L \end{array} \sum_{n=0}^{\infty} \left[\begin{array}{c} A_L \\ | \\ \bar{A}_L \end{array} \right]^n = (l_h | \sum_{n=0}^{\infty} [T_L]^n, \quad (4.47)$$

$$R_h = \begin{array}{c} \text{---} \\ | \quad | \\ \text{---} \end{array} = \begin{array}{c} \sum_{n=0}^{\infty} \left[\begin{array}{c} A_R \\ | \\ \bar{A}_R \end{array} \right]^n \\ | \quad | \\ A_R \quad A_R \\ | \quad | \\ \bar{A}_R \quad \bar{A}_R \end{array} = \sum_{n=0}^{\infty} [T_R]^n | r_h). \quad (4.48)$$

To compute L_h and R_h , we make explicit use of the primitivity property. For a general primitive transfer matrix $T = |r)(l| + \mathcal{O}(|\lambda_2|)$ with $|\lambda_2| < 1$, we can compute the infinite geometric sum by separating the peripheral projector and using convergence for the residual operator:

$$\begin{aligned} \sum_{n=0}^{\infty} T^n &= \left[\sum_{n=0}^{\infty} 1 \right] |r)(l| + \sum_{n=0}^{\infty} [T - |r)(l|] \\ &= |\mathbb{N}| |r)(l| + [\mathbb{1} - T + |r)(l|]^{-1}. \end{aligned} \quad (4.49)$$

For the left and right transfer matrices, $T_L = |r)(\mathbb{1}| + \mathcal{O}(|\lambda_2|)$ and $T_R = |\mathbb{1})(l| + \mathcal{O}(|\lambda_2|)$, the formally diverging term $\propto |\mathbb{N}|$ corresponds to the total energy of the left and right half infinite chain, since

$$(l_h | r) = (l | r_h) = e. \quad (4.50)$$

By a constant energy shift $\tilde{h} = h - e\mathbb{1}$, we can ensure that the current state has energy density $\tilde{e} = 0$ and avoid the extensive contribution. As a consequence, after having computed the nontrivial right and left eigenvectors r and l , we can compute L_h and R_h as the solution of the following systems of linear equations:

$$(L_h | [\mathbb{1} - T_L + |r)(l|] = (l_h |, \quad (4.51)$$

$$[\mathbb{1} - T_R + |\mathbb{1})(l|] |R_h) = |r_h). \quad (4.52)$$

The variational ground state optimum, corresponding to $G = 0$ in (4.44), simultaneously satisfies the following conditions for the tensors A_C , C , A_L , A_R :

O1) $|A_C\rangle$ ground state of $H_{\text{eff},1}$,

O2) $|C\rangle$ ground state of $H_{\text{eff},0}$,

O3) $A_C = A_L C = C A_R$.

One update of the VUMPS (acronym for *variational uniform matrix product states*) algorithm consists of

A1) $|A_C\rangle \rightarrow$ ground state of $H_{\text{eff},1}$,

A2) $|C\rangle \rightarrow$ ground state of $H_{\text{eff},0}$,

A3) A_L/A_R from right/left polar decompositions of A_C and C .

For a fixed bond dimension D , we bring a random, primitive tensor (with spectral radius one) into canonical form and repeat the steps A1)–A3) until convergence in gradient norm up to tolerance tol:

$$\mathcal{E}_{\text{VUMPS}} = \|G\|_2 = \|H_{\text{eff},1}(A_C) - A_L H_{\text{eff},0}(C)\|_2 < \text{tol}. \quad (4.53)$$

A few comments about the VUMPS algorithm:

- To make the implementation efficient, we solve the effective eigenvalue problems A1) and A2) with an iterative Lanczos method, which only needs to know the effect of $H_{\text{eff},1}$ and $H_{\text{eff},0}$ on $|A_C\rangle$ and $|C\rangle$, respectively. Previous tensors are used as initial guesses. In the same way, we use iterative Arnoldi methods to compute the eigenvectors r, l of the (non-Hermitian) transfer matrices T_L, T_R and to solve the linear equations (4.51), (4.52). As a consequence, the computational time complexity of the VUMPS algorithm scales as $\mathcal{O}(D^3)$.
- Before convergence, the canonical form $A_C = A_L C = C A_R$ is not exactly fulfilled. If it was, $r = CC^\dagger$ and $l = C^T \bar{C}$ would be the nontrivial right and left eigenvectors of T_L and T_R , needed for (4.51) and (4.52). Nevertheless, we can use them as initial guesses for the Arnoldi iterations.
- We still have to specify A3). In exact arithmetic, the solution of the minimization problems

$$\min_{A_L^\dagger A_L = \mathbb{1}} \|A_C - A_L C\|_2, \quad \min_{A_R A_R^\dagger = \mathbb{1}} \|A_C - C A_R\|_2 \quad (4.54)$$

is known: A_L is equal to the isometry in the right polar decomposition of $A_C C^\dagger$, A_R is equal to the isometry in the left polar decomposition of $C^\dagger A_C$. But this involves the square of the singular values of C , which might fall below machine precision. An alternative that is robust in finite precision arithmetic (and still close to optimal) is given by the following computation from separate polar decompositions of A_C and C :

$$\mathbb{C}^{Dd \times D} \ni A_C \stackrel{\text{rP}}{=} U_{L,1} P_{L,1} \text{ and } C \stackrel{\text{rP}}{=} U_{L,0} P_{L,0} \Rightarrow A_L = U_{L,1} U_{L,0}^\dagger, \quad (4.55)$$

$$\mathbb{C}^{D \times dD} \ni A_C \stackrel{\text{lP}}{=} P_{R,1} U_{R,1} \text{ and } C \stackrel{\text{lP}}{=} P_{R,0} U_{R,0} \Rightarrow A_R = U_{R,0}^\dagger U_{R,1}. \quad (4.56)$$

- In contrast to iDMRG, which successively grows the lattice by updated unit cells, VUMPS truly solves the variational problem in the sense of completely updating the state with each iteration and consequently keeping the translation invariance at any time.

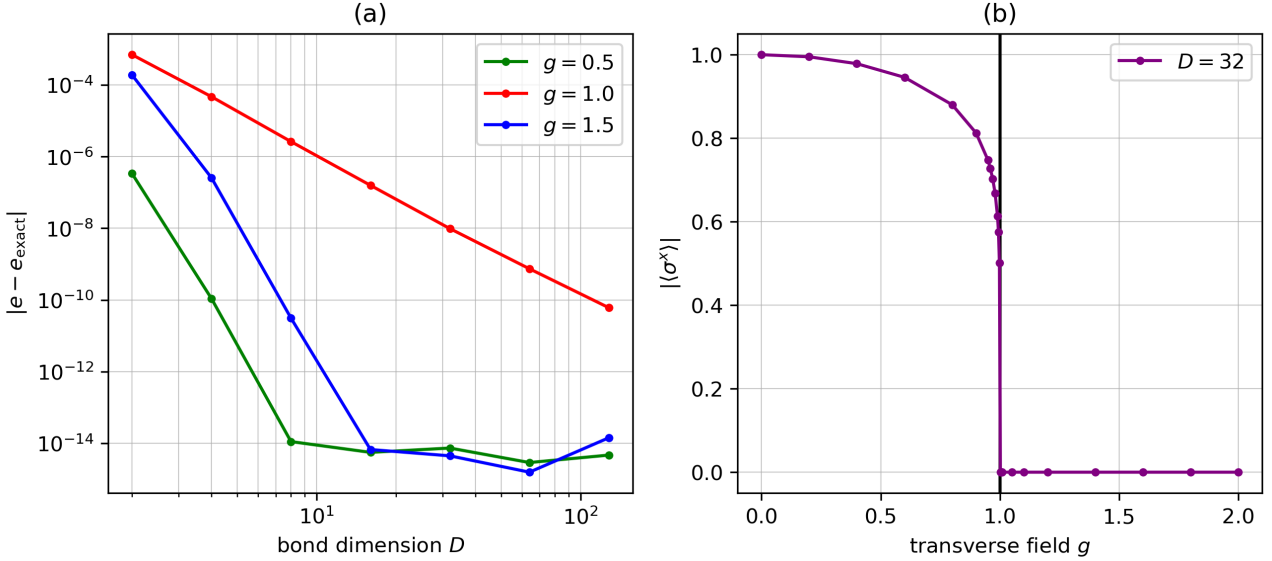


Figure 4.2: TFI benchmark for the VUMPS algorithm with tolerance 10^{-12} in gradient norm. In the left panel (a), we plot the energy density error $\Delta e = |e - e_{\text{exact}}|$ against increasing bond dimension on a log-log scale. In the gapped phases with representative transverse field values $g = 0.5$ and $g = 1.5$, the error falls below machine precision quickly. At the critical point $g = 1$, the error exhibits a power law scaling with D . In the right panel (b), we show the sharp transition to zero magnetization density at $g = 1$, obtained for $D = 32$.

Benchmark

We now benchmark the VUMPS algorithm on the TFI model, for which the ground state energy density can be exactly computed with Jordan-Wigner and Bogoliubov transformations (as summarized in section 2.3):

$$e_{\text{exact}} = -\frac{1}{2\pi} \int_{-\pi}^{\pi} dp \frac{\epsilon_p}{2} \stackrel{J=1}{=} -\frac{1}{2\pi} \int_{-\pi}^{\pi} dp \sqrt{g^2 - 2g \cos(p) + 1}. \quad (4.57)$$

For a tolerance of 10^{-12} in gradient norm (4.53), and different bond dimensions D , we run VUMPS to get an approximate ground state with energy density e . We plot the convergence of the energy error $\Delta e = |e - e_{\text{exact}}|$ against D on a log-log scale, for the three representative transverse field values $g = 0.5$ (ferromagnetic phase), $g = 1.0$ (critical point) and $g = 1.5$ (paramagnetic phase). The results are shown in the left part (a) of figure 4.2. In the gapped phases $g \neq 1$, the error falls below machine precision already at modest bond dimensions ($D \approx 16$). At the critical point $g = 1$, the error exhibits a power law scaling with D , in agreement with the theory of finite entanglement scaling at one-dimensional quantum critical points [PMTM09].

For our purposes, an energy accuracy of 10^{-8} and therefore a bond dimension of $D = 32$ is sufficient for all values of g . In the right panel (b) of figure 4.2, the magnetization density $m = |\langle \sigma^x \rangle|$ of the VUMPS ground state serves as an order parameter for the TFI quantum phase diagram. As expected from section 2.1, starting from $m = 1$ at $g = 0$, quantum fluctuations reduce m as g is increased and lead to a sharp drop to $m = 0$ at the critical point $g = 1$.

4.4 Variational plane wave excitations (VPWE)

Seeing the uMPS ground state $|\psi(A)\rangle$ as correlated background, we create a single quasiparticle excitation on top by inserting local tensor perturbations in a momentum plane wave superposition [HPW⁺12, VHV19b]:

$$|\psi_p(B; A)\rangle = \sum_{n \in \mathbb{Z}} e^{ipn} \cdots \rightarrow \boxed{A_L} \rightarrow \boxed{A_L} \xrightarrow{n} \boxed{B} \xleftarrow{n} \boxed{A_R} \leftarrow \boxed{A_R} \leftarrow \cdots. \quad (4.58)$$

Gauge fixing

Our ansatz (4.58) is a boosted version of the tangent space vector (4.30), with slightly modified gauge freedom:

$$B \rightarrow B + A_L Y - e^{-ip} Y A_R \quad (4.59)$$

leaves the state invariant for any $Y \in \mathbb{C}^{D \times D}$. Again, we fix the D^2 gauge parameters by the effective parametrization

$$\rightarrow \boxed{B} \leftarrow = \rightarrow \boxed{V_L} \xrightarrow{D} \boxed{X} \xleftarrow{D} \text{ with } \begin{array}{c} \rightarrow \boxed{V_L} \rightarrow \\ \downarrow \\ \rightarrow \boxed{A_L} \rightarrow \end{array} = 0. \quad (4.60)$$

This has two crucial implications. First, it ensures that the excitations

$$|\psi_p(X; A)\rangle = \sum_{n \in \mathbb{Z}} e^{ipn} \cdots \rightarrow \boxed{A_L} \rightarrow \boxed{A_L} \rightarrow \boxed{V_L} \xrightarrow{n} \boxed{X} \xleftarrow{n} \boxed{A_R} \leftarrow \boxed{A_R} \leftarrow \cdots \quad (4.61)$$

are orthogonal to the ground state by construction:

$$\langle \psi(\bar{A}) | \psi_p(X; A) \rangle = 0 \text{ for all } p, X. \quad (4.62)$$

Second, it implies that the overlap between two excitations is given by

$$\langle \psi_k(\bar{Y}; A) | \psi_p(X; A) \rangle = 2\pi\delta(p - k)(\bar{Y}|X). \quad (4.63)$$

For this we used the following relation, which reduces a double sum over $n, l \in \mathbb{Z}$ to a single one, for any quantity f that only depends on the distance $n - l$:

$$\sum_{n, l \in \mathbb{Z}} e^{ipn} e^{-ikl} f(n - l) \stackrel{m=n-l}{=} \sum_{l \in \mathbb{Z}} e^{i(p-k)l} \sum_{m \in \mathbb{Z}} e^{ipm} f(m) = 2\pi\delta(p - k) \sum_{m \in \mathbb{Z}} e^{ipm} f(m). \quad (4.64)$$

From (4.63) we can conclude that the gauge (4.60) orthogonalizes excitations with different momenta and removes zero-modes, i.e. nonzero tensors $B_0 = A_L Y - e^{-ip} Y A_R \neq 0$ that correspond to zero-states $|\psi_p(B_0; A)\rangle = 0$. As a consequence, for a fixed momentum p , the plane wave excitations (4.61) are well-defined for a variational minimization of the energy with respect to X :

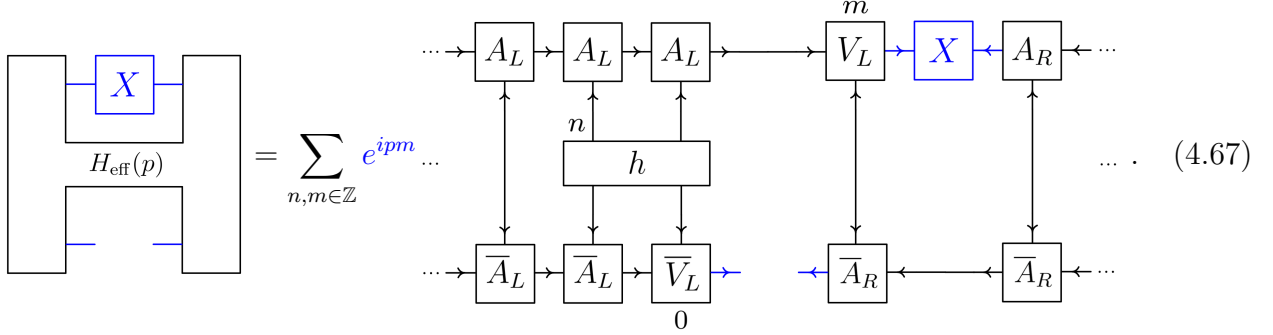
$$\arg \min_{X \in \mathbb{C}^{D(d-1) \times D}} \frac{\langle \psi_p(\bar{X}; \bar{A}) | H | \psi_p(X; A) \rangle}{\langle \psi_p(\bar{X}; \bar{A}) | \psi_p(X; A) \rangle}. \quad (4.65)$$

Effective Hamiltonian

Again making use of (4.64), the stationary condition (3.13) becomes

$$2\pi\delta(0) \partial_{\bar{X}} [(\bar{X}|H_{\text{eff}}(p)|X) - \lambda(\bar{X}|X)] = 0. \quad (4.66)$$

The effective Hamiltonian $H_{\text{eff}}(p)$ acts on X as follows:



The extensive tensor diagrams for all terms of the double sum (4.67) are shown in appendix C. Some terms vanish in the chosen gauge. In addition to the boundary tensors (4.47) and (4.48), there are also terms involving infinite geometric sums of the mixed transfer matrices

$$T_{RL} = \sum_s A_R^s \otimes \bar{A}_L^s = |C^\dagger| (C^T| + \mathcal{O}(|\lambda_2|)) \text{ with } |\lambda_2| < 1, \quad (4.68)$$

$$T_{LR} = \sum_s A_L^s \otimes \bar{A}_R^s = |C| (\bar{C}| + \mathcal{O}(|\lambda_2|)) \text{ with } |\lambda_2| < 1. \quad (4.69)$$

We explain how these terms can be calculated by picking out one of them:

$$\begin{aligned} & e^{-ip} \left[\begin{array}{c} A_L \\ h \\ \bar{A}_L \end{array} \right] \xrightarrow{\quad} \left[\begin{array}{c} B \\ h \\ \bar{A}_L \end{array} \right] \xrightarrow{\quad} \left[\begin{array}{c} \sum_{l=0}^{\infty} \left[\begin{array}{c} e^{-ip} \\ A_R \\ \bar{A}_L \end{array} \right]^l \\ A_R \\ \bar{V}_L \end{array} \right] \\ & = e^{-ip} \underbrace{\left(l_B \mid \sum_{l=0}^{\infty} [e^{-ip} T_{RL}]^l T_{A_R, \bar{V}_L} \right)}_{=: (L_B |}. \end{aligned} \quad (4.70)$$

As for (4.47) and (4.48), we calculate the infinite geometric sum by splitting off the peripheral projector (multiplied by a phase) and using convergence for the residual operator:

$$\begin{aligned} \sum_{l=0}^{\infty} [e^{-ip} T_{RL}]^l &= \left[\sum_{l=0}^{\infty} e^{-ipl} \right] |C^\dagger| (C^T| + \sum_{l=0}^{\infty} [e^{-ip} T_{RL} - e^{-ip} |C^\dagger| (C^T|)]^l \\ &= \left[\sum_{l=0}^{\infty} e^{-ipl} \right] |C^\dagger| (C^T| + [\mathbb{1} - e^{-ip} T_{RL} + e^{-ip} |C^\dagger| (C^T|)]^{-1}. \end{aligned} \quad (4.71)$$

The geometric sum $\sum_{l=0}^{\infty} e^{-ipl}$ is divergent. But thanks to the gauge fixing, there is no contribution in the subspace $|C^\dagger\rangle (C^T|$ anyways:

$$(4.72)$$

With this the boundary tensor $(L_B|$ is obtained from the solution of the following system of linear equations:

$$(L_B| [\mathbb{1} - e^{-ip} T_{RL} + e^{-ip} |C^\dagger\rangle (C^T|] = e^{-ip} (l_B| . \quad (4.73)$$

Having implemented the whole action of $H_{\text{eff}}(p)$ on X with an iterative Arnoldi method, the optimization (4.66) for the lowest-lying excitation with momentum p boils down to an iterative ground state search:

$$H_{\text{eff}}(p)|X\rangle = \epsilon_p |X\rangle , \quad (4.74)$$

where ϵ_p is the energy difference to the ground state.

Topological excitations

We can also target single topological domain wall excitations with our ansatz (4.61), by choosing A_L and $A_R \rightarrow \tilde{A}_R$ from the two orthogonal symmetry broken ground states. The only difference in the algorithm concerns the mixed transfer matrices $T_{\tilde{R}L}$ and $T_{L\tilde{R}}$. Since they have spectral radius strictly smaller than one (otherwise the two symmetry broken ground states would not be orthogonal), the corresponding infinite geometric sums can be computed with the full inverse:

$$\sum_{l=0}^{\infty} [e^{-ip} T_{\tilde{R}L}]^l = [\mathbb{1} - e^{-ip} T_{\tilde{R}L}]^{-1} . \quad (4.75)$$

As a second peculiarity, multiplying \tilde{A}_R with a phase $e^{i\phi}$ shifts the momentum $p \rightarrow p + \phi$. We fix it unambiguously by ensuring that the dominant eigenvalue of $T_{\tilde{R}L}$ is positive. [VHV19b]

Benchmark

In total, we have presented an algorithm that variationally finds elementary quasiparticle excitations on top of a VUMPS ground state. These excitations may be of local or topological nature. They describe plane waves with definite momentum p and excitation energy ϵ_p . By solving the effective Hamiltonian eigenequation (4.74) with an iterative Lanczos method for multiple momenta p within the first Brillouin zone $(-\pi, \pi]$, we can infer a dispersion relation. For the TFI model, we can compare it to the exact one:

$$\epsilon_p \stackrel{J=1}{=} 2\sqrt{g^2 - 2g \cos(p) + 1} . \quad (4.76)$$

The result is shown in figure 4.3, again for the transverse field values $g = 0.5$ (symmetry broken phase), $g = 1.0$ (critical point) and $g = 1.5$ (unordered phase). Within the given energy

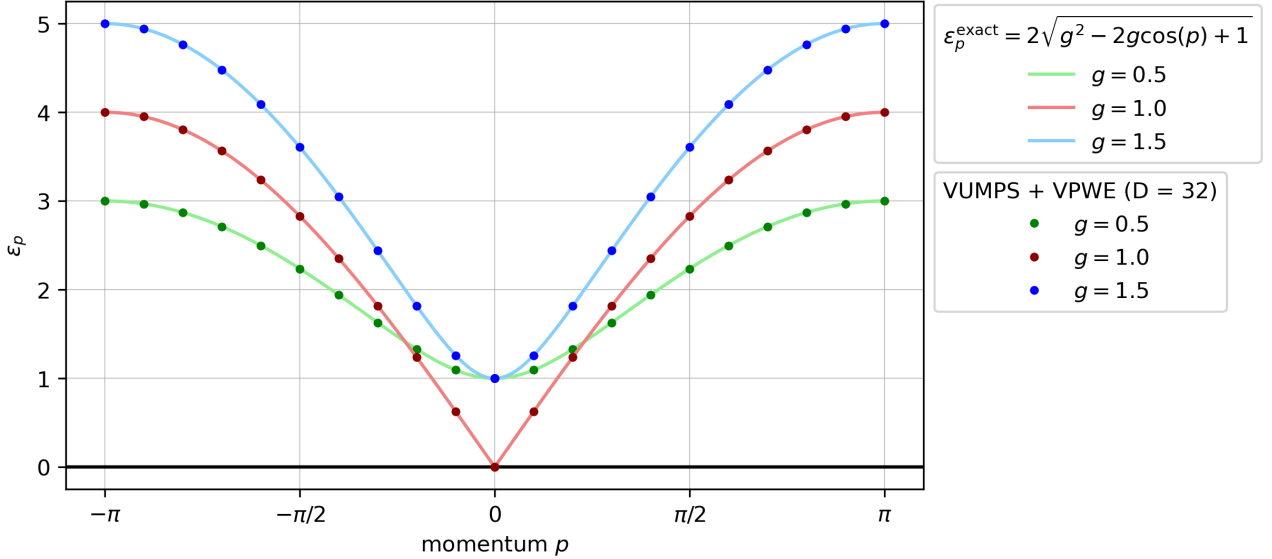


Figure 4.3: TFI benchmark for variational plane wave excitations (VPWE) on top of a uMPS ground state. Optimization of the quasiparticle ansatz $|\psi_p(X; A)\rangle$ for the lowest-lying excitation of the Hamiltonian boils down to the ground state equation $H_{\text{eff}}(p)|X\rangle = \epsilon_p|X\rangle$. We solve it with an iterative Lanczos method for multiple momenta p within the first Brillouin zone. The results lie on the exact dispersion curve for all three values of g , even at criticality.

resolution, all optimized pairs (p, ϵ_p) lie precisely on the dispersion curve. The persistence of sharp quasiparticle excitations at criticality is a special feature of the TFI model, due to its exact mapping to free fermions, as discussed in section 2.3. In general, the excitations of critical quantum many body systems have a more complex, collective structure.

Chapter 5

Matrix product states (MPS)

Compared to the previous chapter, where we worked in the thermodynamic limit, we now restrict the spin chain to a finite size N . Moreover, we explicitly break translation invariance by imposing open boundary conditions and allowing the tensors to be site-dependent:

$$A^{[n]} \in \mathbb{C}^{D_{n-1} \times d \times D_n} \text{ with } D_0 = D_N = 1. \quad (5.1)$$

For computational basis indices s_1, \dots, s_N , the finite matrix product $A^{[1]s_1} \dots A^{[N]s_N}$ defines the probability amplitude of the d^N dimensional *matrix product state* (MPS)

$$|\psi(A^{[1]}, \dots, A^{[N]})\rangle = \sum_{\{s_n\}} A^{[1]s_1} A^{[2]s_2} \dots A^{[N]s_N} |s_1 \dots s_N\rangle = \dots \boxed{A^{[1]}} \dots \boxed{A^{[2]}} \dots \dots \boxed{A^{[N]}} \dots \quad (5.2)$$

Analogous to uMPS, for a fixed set of bond dimensions $\{D_n\}_{n=1}^{N-1}$, we can define a complex manifold of tensors that is biholomorphic to the manifold of corresponding MPS. This was rigorously established in [HMOV14]. The necessary restriction (in analogy to primitivity for uMPS) is now to tensors with positive definite *virtual density matrices*. They are defined recursively via

$$\begin{aligned} l^{[0]} &= 1, \quad l^{[n]} = \sum_{s_n} (A^{[n]s_n})^\dagger l^{[n-1]} A^{[n]s_n}, \\ r^{[N]} &= 1, \quad r^{[n-1]} = \sum_{s_n} A^{[n]s_n} r^{[n]} (A^{[n]s_n})^\dagger, \end{aligned} \quad (5.3)$$

for $n = 1, \dots, N$. The gauge group is now the product $\prod_{n=1}^N \mathrm{GL}(D_n, \mathbb{C})$ with the following transformation leaving the MPS invariant:

$$B^{[n]s_n} = (S^{[n-1]})^{-1} A^{[n]s_n} S^{[n]} \text{ with } S^{[0]} = S^{[N]} \in \mathbb{C}. \quad (5.4)$$

The group elements $\{\{\alpha \mathbb{1}_{D_n}\}_{n=1}^N | \alpha \in \mathbb{C}\}$ act trivially on the tensors $\{A^{[n]}\}$ and therefore we have to quotient out $\mathrm{GL}(1, \mathbb{C})$. Since the gauge group is a direct product containing $\mathrm{GL}(D_N, \mathbb{C})$ with $D_N = 1$, we end up with $\prod_{n=1}^{N-1} \mathrm{GL}(D_n, \mathbb{C})$ as the effective gauge group of the MPS manifold. In summary,

$$\mathcal{A}_{\{D_n\}} = \left\{ \bigoplus_{n=1}^N \mathbb{C}^{D_{n-1} \times d \times D_n} \mid l^{[n]}, r^{[n]} > 0 \text{ for all } n \right\} / \prod_{n=1}^{N-1} \mathrm{GL}(D_n, \mathbb{C}) \quad (5.5)$$

is biholomorphic to

$$\mathcal{M}_{\{D_n\}} = \left\{ |\psi(A^{[1]}, \dots, A^{[N]})\rangle \in \mathbb{C}^{d^N} \mid \{A^{[n]}\} \in \mathcal{A}_{\{D_n\}} \right\}. \quad (5.6)$$

In section 5.2 we will variationally optimize ground states within $\mathcal{M}_{\{D_n\}}$, using the *density matrix renormalization group* (DMRG) algorithm. Then, in section 5.3, we will construct quasiparticle excitations on top, by optimizing (a parametrized version of) the tangent space vector

$$\begin{aligned} |\psi(B; A)\rangle &= \sum_{n, \alpha_{n-1}, s_n, \beta_n} B_{\alpha_{n-1}, \beta_n}^{[n]s_n} \left[\partial_{A_{\alpha_{n-1}, \beta_n}^{[n]s_n}} |\psi(A)\rangle \right] \\ &= \sum_n \cdots \boxed{A^{[1]}} \cdots \boxed{A^{[n-1]}} \boxed{B^{[n]}} \boxed{A^{[n+1]}} \cdots \boxed{A^{[N]}} \cdots . \end{aligned} \quad (5.7)$$

But let us first bring the MPS into canonical form, which can always be achieved within the gauge freedom. Note that in this chapter A and B always have to be understood as a set of tensors $\{A^{[n]}\}_{n=1}^N$ and $\{B^{[n]}\}_{n=1}^N$.

5.1 Intrinsic canonical form

Our starting point is the general MPS form (5.2). We initialize the dummy matrix $L^{[N+1]} = ((1)) \in \mathbb{C}^{1 \times 1}$ and successively perform the following LQ decompositions from right to left, i.e. for $n = N, \dots, 1$:

$$\boxed{A^{[n]}} \rightarrow \boxed{L^{[n+1]}} \xrightarrow{\text{LQ}} \boxed{L^{[n]}} \leftarrow \boxed{A_R^{[n]}} \leftarrow , \quad (5.8)$$

where we extract the *right isometric* $A_R^{[n]}$. Since we make the LQ decompositions unique (with positive entries on the main diagonal of the lower triangular matrices $L^{[n]}$), the final $L^{[1]} \in \mathbb{C}^{1 \times 1}$ is positive and equal to the norm of the MPS. In total, the normalized MPS in right isometric form reads

$$|\psi(A)\rangle = \leftarrow \boxed{A_R^{[1]}} \leftarrow \boxed{A_R^{[2]}} \leftarrow \cdots \leftarrow \boxed{A_R^{[N]}} \leftarrow . \quad (5.9)$$

Now, we start from the left end of the chain, with dummy matrix $C^{[0]} = ((1)) \in \mathbb{C}^{1 \times 1}$, and perform the following SVDs for $n = 1, \dots, N$:

$$\rightarrow \boxed{C^{[n-1]}} \leftarrow \boxed{A_R^{[n]}} \leftarrow \xrightarrow{\text{SVD}} \rightarrow \boxed{A_L^{[n]}} \rightarrow \boxed{C^{[n]}} \leftarrow \boxed{V^{[n]}} \leftarrow , \quad (5.10)$$

with *left isometric tensor* $A_L^{[n]}$ and normalized, diagonal, positive semidefinite *center matrix* $C^{[n]}$. To stay consistent with the right isometric form, we redefine for all $n < N$:

$$\leftarrow \boxed{A_R^{[n+1]}} \leftarrow \rightarrow \rightarrow \leftarrow \boxed{V^{[n]}} \leftarrow \boxed{A_R^{[n+1]}} \leftarrow , \quad \leftarrow \boxed{A_R^{[n]}} \leftarrow \rightarrow \rightarrow \leftarrow \boxed{A_R^{[n]}} \leftarrow \boxed{V^{[n]\dagger}} \leftarrow . \quad (5.11)$$

Sometimes it is convenient to contract $A_L^{[n]}$ and $C^{[n]}$ (or equivalently $C^{[n-1]}$ and $A_R^{[n]}$) into a normalized *center tensor* $A_C^{[n]}$. With this can write the MPS in the following three equivalent

ways, for any site n in the chain:

$$\begin{aligned}
 |\psi(A)\rangle &= \rightarrow [A_L^{[1]}] \rightarrow \dots \rightarrow [A_L^{[n-1]}] \rightarrow [A_C^{[n]}] \leftarrow [A_R^{[n+1]}] \leftarrow \dots \leftarrow [A_R^{[N]}] \leftarrow \\
 &= \rightarrow [A_L^{[1]}] \rightarrow \dots \rightarrow [A_L^{[n-1]}] \rightarrow [A_L^{[n]}] \rightarrow [C^{[n]}] \leftarrow [A_R^{[n+1]}] \leftarrow \dots \leftarrow [A_R^{[N]}] \leftarrow \\
 &= \rightarrow [A_L^{[1]}] \rightarrow \dots \rightarrow [A_L^{[n-1]}] \rightarrow [C^{[n-1]}] \leftarrow [A_R^{[n]}] \leftarrow [A_R^{[n+1]}] \leftarrow \dots \leftarrow [A_R^{[N]}] \leftarrow .
 \end{aligned} \tag{5.12}$$

This is the *canonical form* for MPS, the finite analog of (4.20). In particular, it gives direct access to the Schmidt values, on the diagonal of $C^{[n]}$ for a bipartition at bond n . This clarifies the restriction of the tensor manifold to positive definite virtual density matrices (5.3). In canonical form, they simply become $l^{[n]} = (C^{[n]})^2$ and $r^{[n]} = \mathbb{1}$, so that positive definiteness becomes equivalent to full Schmidt rank.

At this point, let us also specify the values of the bond dimensions $\{D_n\}_{n=1}^{N-1}$, appearing in the tensor dimensions as

$$A_L^{[n]}, A_R^{[n]}, A_C^{[n]} \in \mathbb{C}^{D_{n-1} \times d \times D_n}, C^{[n]} \in \mathbb{C}^{D_n \times D_n}. \tag{5.13}$$

In principle, any state $|\psi\rangle \in \mathbb{C}^{d^N}$ can be brought into right isometric MPS form (5.9) with successive LQ decompositions. In the generic case, the bond dimensions then satisfy $D_n = \min(d^n, d^{N-n})$ and thus grow exponentially from both sides until they reach $d^{\lfloor N/2 \rfloor}$ in the middle of the chain. However, the area law (4.26) tells us that ground states of local, gapped Hamiltonians can be faithfully approximated using bond dimensions that remain non-extensive in system size. Accordingly, we impose an upper bound D_{\max} in practical computations:

$$D_n = \min(d^n, d^{N-n}, D_{\max}). \tag{5.14}$$

5.2 Density matrix renormalization group (DMRG)

To minimize the Hamiltonian energy for the MPS in canonical form (5.12), we want to optimize one center tensor at a time, while keeping all the other isometric tensors fixed. An obvious choice for the center tensor is $A_C^{[n]}$, which leads to the *one site density matrix renormalization group* algorithm. Dependent on the chosen initial state, this variational method is quite prone to getting stuck. The bond dimensions stay fixed throughout the whole optimization, so one is restricted to a single, potentially suboptimal manifold. To circumvent this, we enlarge the center by $A_R^{[n+1]}$ to a two-site tensor which we call $\theta_2^{[n,n+1]}$:

$$|\psi(A)\rangle = \rightarrow [A_L^{[1]}] \rightarrow \dots \rightarrow [A_L^{[n-1]}] \rightarrow [A_L^{[n]}] \rightarrow [C^{[n]}] \leftarrow [A_R^{[n+1]}] \leftarrow [A_R^{[n+2]}] \leftarrow \dots \leftarrow [A_R^{[N]}] \leftarrow . \tag{5.15}$$

This is the variational state for the *two site density matrix renormalization group* algorithm [Sch11]. Let us next express the Hamiltonian in a form that matches the MPS structure.

MPO Hamiltonian

In the same way we can represent any state $|\psi\rangle \in \mathbb{C}^{d^N}$ as an MPS, we can represent any Hamiltonian $H \in \mathbb{C}^{d^N \times d^N}$ as a *matrix product operator* (MPO). More precisely, we can find N four leg tensors

$$W^{[n]} \in \mathbb{C}^{\chi_{n-1} \times \chi_n \times d \times d} \text{ with } \chi_0 = \chi_N = 1, \quad (5.16)$$

such that

$$H = \sum_{\{s_n\}} \sum_{\{\tilde{s}_n\}} W^{[1]s_1, \tilde{s}_1} W^{[2]s_2, \tilde{s}_2} \dots W^{[N]s_N, \tilde{s}_N} |s_1 \dots s_N\rangle \langle \tilde{s}_1 \dots \tilde{s}_N| = \dots - \boxed{W^{[1]}} - \boxed{W^{[2]}} - \dots - \boxed{W^{[N]}} - \dots \quad (5.17)$$

The key limitation for efficient algorithms involving such MPOs lies in the bond dimensions χ_n . In the worst case, they scale exponentially in system size N . This is not the case for local Hamiltonians, which we demonstrate for the transverse field Ising model. Since our MPS (5.12) has open boundary conditions by construction, they are the most natural choice for the Hamiltonian as well.

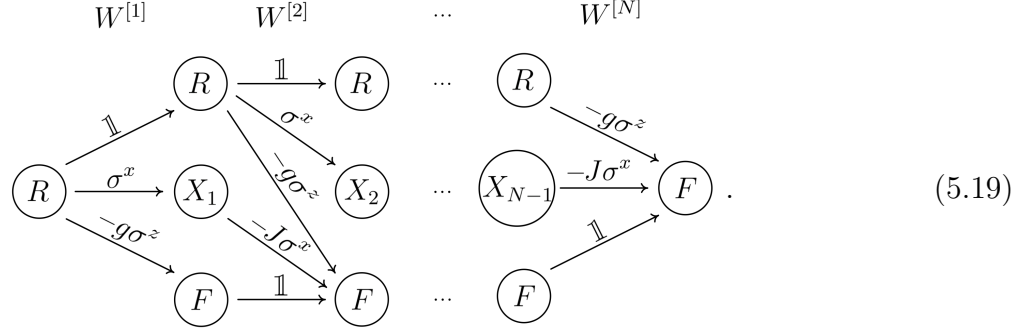
1) Open boundary conditions (OBC)

We start from the Hamiltonian in the normal form, namely as a sum of Kronecker products involving N spin operators each:

$$\begin{aligned} H = -J \sum_{n=1}^{N-1} \sigma_n^x \sigma_{n+1}^x - g \sum_{n=1}^N \sigma_n^z &= \sigma^x \otimes (-J\sigma^x) \otimes \mathbb{1} \otimes \dots \otimes \mathbb{1} \\ &\quad + (-g\sigma^z) \otimes \mathbb{1} \otimes \dots \otimes \mathbb{1} \\ &\quad + \mathbb{1} \otimes \sigma^x \otimes (-J\sigma^x) \otimes \mathbb{1} \otimes \dots \otimes \mathbb{1} \\ &\quad + \mathbb{1} \otimes (-g\sigma^z) \otimes \mathbb{1} \otimes \dots \otimes \mathbb{1} \\ &\quad + \dots . \end{aligned} \quad (5.18)$$

To derive the corresponding MPO, it is useful to start a so called *final state machine* (FSM) [MZMP16]. It is a graph whose nodes represent states and whose directed edges indicate transitions between those states. In the *ready state* R no nontrivial operator has yet been applied, in the *final state* F a whole nontrivial action has been completed. For every summand in the Hamiltonian, there is one path from the leftmost ready state to the rightmost final state, consisting of N transitions. Every transition adds a spin operator to the Kronecker product. As an example, let us consider the interaction term $-J\sigma_1^x \otimes \sigma_2^x$ between the first two spins. We transition from R to X_1 by applying σ^x on the first site. The transition from X_1 to F completes the interaction with the application of the operator $-J\sigma^x$ on site 2. The rest of the path consists of F to F transitions under application of the identity $\mathbb{1}$. In total we get the

following FSM:



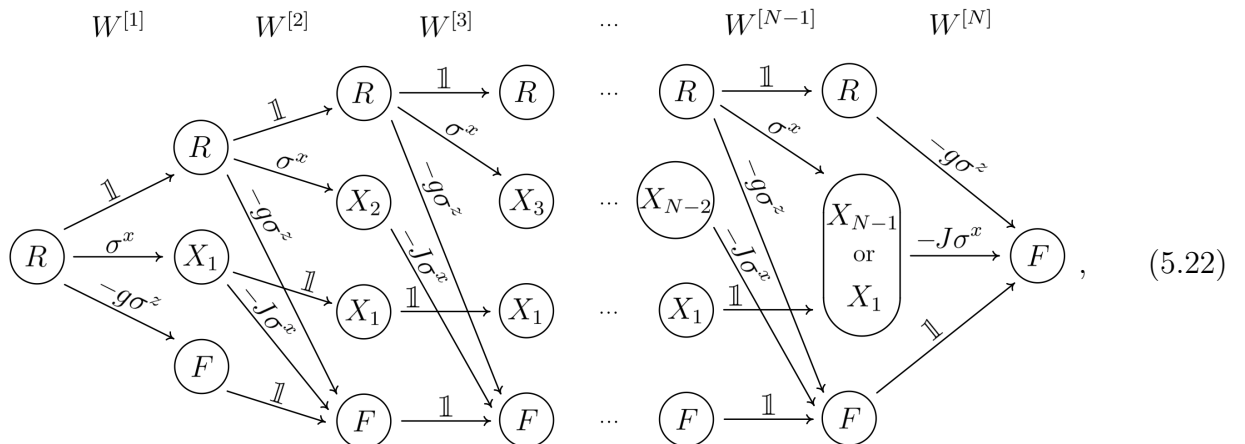
Seeing the four leg tensor $W^{[n]}$ as matrix (virtual legs) with spin operators (physical legs) as entries, the matrix lines are indexed by the states before the transition n , the columns by the states afterwards, and the matrix elements are defined by the transition operators. This gives us the following MPO tensors for the Hamiltonian (5.18):

$$\begin{array}{c} W^{[1]} \\ \left(\begin{array}{ccc} \mathbb{1} & \sigma^x & -g\sigma^z \\ 0 & 0 & -J\sigma^x \\ 0 & 0 & \mathbb{1} \end{array} \right), \end{array} \quad \begin{array}{c} W^{[2]}, \dots, W^{[N-1]} \\ \left(\begin{array}{ccc} \mathbb{1} & \sigma^x & -g\sigma^z \\ 0 & 0 & -J\sigma^x \\ 0 & 0 & \mathbb{1} \end{array} \right), \end{array} \quad \begin{array}{c} W^{[N]} \\ \left(\begin{array}{c} -g\sigma^z \\ -J\sigma^x \\ \mathbb{1} \end{array} \right). \end{array} \quad (5.20)$$

2) Periodic boundary conditions (PBC)

With regard to the quasiparticle excitations we will create later, we would like to have MPS eigenstates with a definite momentum. In order to commute with the translation operator, the Hamiltonian must have periodic boundary conditions (PBC). In principle, we could also construct the MPS with PBC. But the resulting closed loop in the virtual legs would prevent a canonical form, making the optimization significantly harder. As a practical compromise, we take the Hamiltonian to be periodic and try to restore momentum as a good quantum number for our MPS with open boundaries. The Hamiltonian, finite state machine and MPO tensors for PBC are:

$$H = -J \sum_{n=1}^{N-1} \sigma_n^x \sigma_{n+1}^x - g \sum_{n=1}^N \sigma_n^z - J \sigma_N^x \sigma_1^x, \quad (5.21)$$



$$W^{[1]}, \quad W^{[2]}, \quad W^{[3]}, \dots, W^{[N-2]}, \quad W^{[N-1]}, \quad W^{[N]}$$

$$\begin{pmatrix} \mathbb{1} & \sigma^x & 0 & -g\sigma^z \\ 0 & 0 & \mathbb{1} & -J\sigma^x \\ 0 & 0 & 0 & \mathbb{1} \end{pmatrix}, \quad \begin{pmatrix} \mathbb{1} & \sigma^x & 0 & -g\sigma^z \\ 0 & 0 & 0 & -J\sigma^x \\ 0 & 0 & \mathbb{1} & 0 \\ 0 & 0 & 0 & \mathbb{1} \end{pmatrix}, \quad \begin{pmatrix} \mathbb{1} & \sigma^x & -g\sigma^z \\ 0 & 0 & -J\sigma^x \\ 0 & \mathbb{1} & 0 \\ 0 & 0 & \mathbb{1} \end{pmatrix}, \quad \begin{pmatrix} -g\sigma^z \\ -J\sigma^x \\ \mathbb{1} \end{pmatrix}. \quad (5.23)$$

DMRG

We are now ready to formulate the *density matrix renormalization group* (DMRG) algorithm [Sch11]. The optimization (3.11) over a single center tensor boils down to an effective eigenvalue equation (3.16). For the MPS (5.15) with two-site center tensor $\theta_2^{[n,n+1]}$ and the MPO Hamiltonian (5.17) the effective Hamiltonian acts as

$$H_{\text{eff},2}^{[n,n+1]} \left| \theta_2^{[n,n+1]} \right\rangle = \begin{array}{c} \text{Diagram showing the effective Hamiltonian } H_{\text{eff},2}^{[n,n+1]} \text{ acting on the center tensor } \theta_2^{[n,n+1]}. \text{ The diagram shows a central } \theta_2^{[n,n+1]} \text{ tensor connected to } A_L^{[n-1]}, W^{[n]}, \text{ and } A_R^{[n+1]}. \text{ To the left is the environment } L^{[n-1]} \text{ (with tensors } A_L^{[1]}, \dots, A_L^{[n-1]} \text{ and } W^{[1]}, \dots, W^{[n-1]}), \text{ and to the right is the environment } R^{[n+2]} \text{ (with tensors } A_R^{[n+2]}, \dots, A_R^{[N]} \text{ and } W^{[n+2]}, \dots, W^{[N]}). \text{ The diagram is enclosed in a dashed box.} \end{array} . \quad (5.24)$$

We initialize the MPS with tensors $\{C^{[n]}\}_{n=0}^{N-1}$ and $\{A_R^{[n]}\}_{n=1}^N$. Since our two-site algorithm allows dynamical growth of entanglement, we can start from a product state, such as $| \Rightarrow \rangle$ with $C^{[n]} = ((1)) \in \mathbb{C}^{1 \times 1}$ and $A_R^{[n]\uparrow} = A_R^{[n]\downarrow} = ((1/\sqrt{2})) \in \mathbb{C}^{1 \times 1}$. To not compute recurrent parts of the network over and over again, it is good practice to store partial contractions as environment tenors $L^{[n]}$ and $R^{[n]}$. We initialize $L^{[0]} = R^{[N+1]} = (((1))) \in \mathbb{C}^{1 \times 1 \times 1}$ and compute $R^{[n]}$ for all $n = N, \dots, 3$ from $\{A_R^{[n]}\}_{n=N}^3$ and $\{W^{[n]}\}_{n=N}^3$. Then we sweep through the chain from left to right ($n = 1, \dots, N-1$) and back from right to left ($n = N-2, \dots, 1$) while performing the following updates:

- A1) With the current $\theta_2^{[n,n+1]} = C^{[n-1]} A_R^{[n]} A_R^{[n+1]}$ as initial guess, compute the ground state $\tilde{\theta}_2^{[n,n+1]}$ of $H_{\text{eff},2}^{[n,n+1]}$ using an iterative Lanczos method.
- A2) Split and truncate $\tilde{\theta}_2^{[n,n+1]}$ by performing an SVD. Keep only singular values larger than ϵ and maximally D_{\max} of them:

$$\rightarrow \boxed{\tilde{\theta}_2^{[n,n+1]}} \xleftarrow{\text{SVD}} \min(\#\{\tilde{C}_\alpha^{[n]} > \epsilon\}, D_{\max}) \rightarrow \boxed{\tilde{A}_L^{[n]}} \rightarrow \boxed{\tilde{C}^{[n]}} \rightarrow \boxed{\tilde{A}_R^{[n+1]}} \leftarrow . \quad (5.25)$$

From this update the MPS according to:

$$A_R^{[n]} \rightarrow (C^{[n-1]})^{-1} \tilde{A}_L^{[n]} \tilde{C}^{[n]} \mathbf{1}, \quad C^{[n]} \rightarrow \tilde{C}^{[n]}, \quad A_R^{[n+1]} \rightarrow \tilde{A}_R^{[n+1]}. \quad (5.26)$$

- A3) Update the environments $L^{[n]}$ and $R^{[n+1]}$ using $\tilde{A}_L^{[n]}$ and $\tilde{A}_R^{[n+1]}$ respectively and move to the next site.

¹In general one should avoid inverting small singular values. In this case the inversion in $\tilde{A}_R^{[n]} = (C^{[n-1]})^{-1} \tilde{A}_L^{[n]} \tilde{C}^{[n]}$ is effectively undone after computing $\tilde{\theta}_2^{[n,n+1]} = C^{[n-1]} \tilde{A}_R^{[n]} \tilde{A}_R^{[n+1]}$ at a later point.

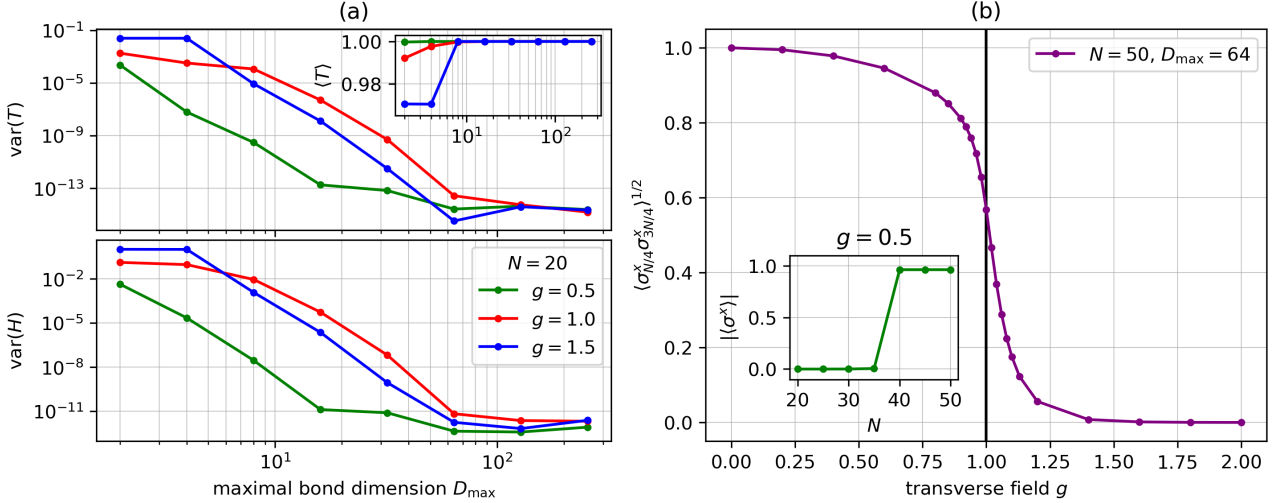


Figure 5.1: TFI benchmark for the DMRG algorithm with periodic Hamiltonian. For the left plots (a), we take a chain of length $N = 20$ and perform 10 DMRG ground state sweeps with a singular value cutoff $\epsilon = 10^{-14}$ and various maximal bond dimensions D_{\max} . Even though the MPS has OBC, the variances of the PBC Hamiltonian and the translation operator fall below 10^{-10} for $D_{\max} \gtrsim 64$. This restores momentum as a good quantum number, with value zero for the ground state (concluded from the inset plot that converges to $\langle T \rangle = 1$). In the inset of the right panel (b), we show that for system sizes $N \lesssim 35$ (at $g = 0.5$), DMRG is able to resolve the exponentially small energy splitting $\delta E_{\pm} = \mathcal{O}(g^N)$ between the symmetric superpositions $\frac{1}{\sqrt{2}}(|\Rightarrow\rangle \pm |\Leftarrow\rangle)$. For $N = 50$, we plot the magnetization order parameter $m = \langle \sigma_{N/4}^x \sigma_{3N/4}^x \rangle^{1/2}$ against g . Compared to the sharp transition in the infinite case, m goes to zero smoothly around $g = 1$.

Benchmark

For the TFI Hamiltonian (5.23) with PBC and $N = 20$, we run 10 of the just described DMRG sweeps with a singular value cutoff $\epsilon = 10^{-14}$. Of the final ground state approximation, we compute the translation expectation value

$$\langle \psi(\bar{A}) | T | \psi(A) \rangle = \begin{array}{c} \text{---} \\ \text{---} \end{array} \boxed{A_R^{[1]}} \dots \boxed{A_R^{[N-1]}} \boxed{A_R^{[N]}} \begin{array}{c} \text{---} \\ \text{---} \end{array}, \quad (5.27)$$

its variance, and the variance of the Hamiltonian. In the left panels (a) of figure 5.1 we plot the results against the maximal bond dimension D_{\max} . Even though the MPS has OBC, the variances of the PBC Hamiltonian and the translation operator fall below 10^{-10} for $D_{\max} \gtrsim 64$. This restores momentum as a good quantum number, with a value zero for the ground state.

5.3 Variational quasiparticle excitations (VQPE)

Completely analogous to the uniform case (4.58), but without the explicit momentum phase, we create a quasiparticle excitation above an MPS ground state $|\psi(A)\rangle$ by inserting local tensor perturbations $\{B^{[n]} \in \mathbb{C}^{D_{n-1} \times d \times D_n}\}_{n=1}^N$ for the center tensors $\{A_C^{[n]}\}_{n=1}^N$ in canonical form [VDVH⁺²¹]:

$$|\psi(B; A)\rangle = \sum_{n=1}^N \rightarrow [A_L^{[1]}] \rightarrow \cdots \rightarrow [A_L^{[n-1]}] \rightarrow [B^{[n]}] \leftarrow [A_R^{[n+1]}] \leftarrow \cdots \leftarrow [A_R^{[N]}] \leftarrow . \quad (5.28)$$

This can be interpreted as a tangent space vector, by applying the definition (5.7) to the left isometric tensors $\{A_L^{[n]}\}_{n=1}^N$ and then, for each term in the sum, moving the full rank center matrix from the very right to the perturbation tensor and absorbing it therein.

Gauge fixing

For any set of matrices $\{Y^{[n]} \in \mathbb{C}^{D_n \times D_n}\}_{n=1}^N$, the state (5.28) does not change under the additive gauge transformation

$$B^{[n]} \rightarrow B^{[n]} + A_L^{[n]} Y^{[n]} - Y^{[n-1]} A_R^{[n]} \text{ with } Y^{[0]} = Y^{[N]} \in \mathbb{C}. \quad (5.29)$$

We fix the $\sum_{n=1}^N D_n^2$ gauge parameters by setting $B^{[n]} = 0$ if $D_{n-1}d = D_n$ and

$$\text{if } D_{n-1}d > D_n : \quad \begin{array}{c} \boxed{B^{[n]}} \\ \downarrow \end{array} = \begin{array}{c} \xrightarrow{D_{n-1}} \boxed{V_L^{[n]}} \xrightarrow{D_n-D_n} \\ \downarrow d \end{array} \quad \text{with} \quad \begin{array}{c} \rightarrow \boxed{V_L^{[n]}} \rightarrow \\ \downarrow \\ \rightarrow \boxed{A_L^{[n]}} \rightarrow \end{array} = 0. \quad (5.30)$$

This ensures that the individual states $|\psi(X^{[n]}; A)\rangle$ in the superposition

$$|\psi(X; A)\rangle = \sum_{n=1}^N |\psi(X^{[n]}; A)\rangle = \sum_{n=1}^N \rightarrow [A_L^{[1]}] \rightarrow \cdots \rightarrow [A_L^{[n-1]}] \rightarrow [V_L^{[n]}] \rightarrow [X^{[n]}] \leftarrow [A_R^{[n+1]}] \leftarrow \cdots \leftarrow [A_R^{[N]}] \leftarrow \quad (5.31)$$

are orthogonal to the ground state and pairwise to each other:

$$\langle \psi(\bar{A}) | \psi(X^{[n]}; A) \rangle = 0, \quad \langle \psi(\bar{Y}^{[m]}; \bar{A}) | \psi(X^{[n]}; A) \rangle = \delta_{nm} (\bar{Y}^{[n]} | X^{[n]}). \quad (5.32)$$

From the latter relation it follows that the map $X \mapsto |\psi(X; A)\rangle$ is injective with

$$\langle \psi(\bar{X}; \bar{A}) | \psi(X; A) \rangle = \sum_n (\bar{X}^{[n]} | X^{[n]}). \quad (5.33)$$

Effective Hamiltonian

Equation (5.33) further implies an identity norm matrix in the effective eigenvalue equation (3.16). We solve it for $X^{[n]}$ by solving

$$\partial_{\overline{B}^{[n]}} (\overline{B} | H_{\text{eff}} | B) = \lambda | B^{[n]} | \quad (5.34)$$

for $B^{[n]} = V_L^{[n]} X^{[n]}$.² For the action of the effective Hamiltonian,

$$(\overline{B} | H_{\text{eff}} | B) = \sum_{n=1}^N \left[\begin{array}{c} \text{Diagram 1: } L_B^{[n-1]} \xrightarrow{\text{W}^{[n]}} R^{[n+1]} \\ \text{Diagram 2: } L^{[n-1]} \xrightarrow{\text{W}^{[n]}} R^{[n+1]} \\ \text{Diagram 3: } L_B^{[n-1]} \xrightarrow{\text{W}^{[n]}} R_B^{[n+1]} \end{array} \right],$$

we compute the following boundary tensors iteratively starting from $L^{[0]} = R^{[N+1]} = (((1))) \in \mathbb{C}^{1 \times 1 \times 1}$ and $L_B^{[0]} = R_B^{[N+1]} = 0$:

$$\begin{aligned} L^{[n]} &= L^{[n-1]} \xrightarrow{\text{A}_L^{[n]}} \text{W}^{[n]} \xrightarrow{\text{A}_L^{[n]}} ; \quad L_B^{[n]} = L^{[n-1]} \xrightarrow{\text{W}^{[n]}} \text{B}^{[n]} \xrightarrow{\text{A}_L^{[n]}} + L_B^{[n-1]} \xrightarrow{\text{W}^{[n]}} \text{A}_R^{[n]} \xrightarrow{\text{A}_R^{[n]}} \quad (n = 1, \dots, N-1), \\ R^{[n]} &= \text{A}_R^{[n]} \xrightarrow{\text{W}^{[n]}} R^{[n+1]} ; \quad R_B^{[n]} = \text{A}_R^{[n]} \xrightarrow{\text{W}^{[n]}} \text{B}^{[n]} \xrightarrow{\text{A}_R^{[n]}} + \text{A}_L^{[n]} \xrightarrow{\text{W}^{[n]}} R_B^{[n+1]} \quad (n = N, \dots, 2). \end{aligned} \quad (5.35)$$

After having solved (5.34) with Lanczos for several algebraically smallest energy eigenvalues, we try to restore momentum as a good quantum number by diagonalizing the translation operator within each degenerate eigenspace. The successful result for $N = 20$ and $D_{\max} = 64$ is shown in figure 5.2 (a). All excitations have a definite momentum $2\pi k/N$ for $k \in \{-\frac{N}{2} + 1, \dots, \frac{N}{2}\}$ and the corresponding energies agree with exact diagonalization. We also plot the single particle dispersion obtained from the exact mapping to free fermions in the odd parity sector. In the paramagnetic phase with representative transverse field value $g = 1.5$, the lowest-lying excitations for all covered momenta lie perfectly on the dispersion curve. At the critical point $g = 1$ this is only roughly the case, as the distinction between different fermion parity sectors becomes more delicate for finite sizes. In the ferromagnetic phase, shown here for $g = 0.5$, the lowest-lying excitations are topological domain walls, which are not accessible with a periodic Hamiltonian.

²We implement the effective matrix-vector multiplication by transforming $X \rightarrow B = \{V_L^{[n]} X^{[n]}\}$, computing $\tilde{B}^{[n]} = \partial_{\overline{B}^{[n]}} (\overline{B} | H_{\text{eff}} | B)$, and transforming back to $\tilde{X} = \{\overline{V}_L^{[n]} \tilde{B}^{[n]}\}$.

Effective translation operator

Knowing that momentum is a good quantum number, we can also directly target it by including the Hermitian sum of the translation operator in the effective eigenequation:

$$\left[H_{\text{eff}} - \alpha \left(e^{-i\frac{2\pi}{N}k} T_{\text{eff}} + e^{i\frac{2\pi}{N}k} T_{\text{eff}}^\dagger \right) \right] |B\rangle = \epsilon_k |B\rangle. \quad (5.36)$$

The value for $\alpha > 0$ is chosen heuristically. It should be large enough to select the correct momentum sector, but not so large that it overrides the actual energy minimization. The tensor networks of the translation expectations values can be drawn as

$$\begin{aligned} (\bar{B}|T_{\text{eff}}|B) &= \\ \begin{array}{c} \text{---} \\ \text{---} \end{array} &+ \sum_{n=2}^N \left[\begin{array}{c} \text{---} \\ \text{---} \end{array} \right. \end{aligned} \quad (5.37)$$

$$\begin{aligned} (\bar{B}|T_{\text{eff}}^\dagger|B) &= \\ \sum_{n=1}^{N-1} \left[\begin{array}{c} \text{---} \\ \text{---} \end{array} \right. &+ \left. \begin{array}{c} \text{---} \\ \text{---} \end{array} \right] + \left. \begin{array}{c} \text{---} \\ \text{---} \end{array} \right] + \left. \begin{array}{c} \text{---} \\ \text{---} \end{array} \right]. \end{aligned} \quad (5.38)$$

The boundary tensors are specified in appendix C. The recursive principle of summing up the terms that

- (i) apply $B^{[n]}$ to the identity boundary,
- (ii) transfer the boundary for which all $B^{[m < n]}$ already have been applied,

is the same as for H_{eff} . The results for the TFI model, again for the values $g = 0.5$, $g = 1.0$ and $g = 1.5$ are shown in figure 5.2 (b). The crucial difference to (a) lies in the direct access to the whole dispersion relation, in the sense that we don't have to compute multiple excitations of the same momentum to reach the first excitation of other momenta.

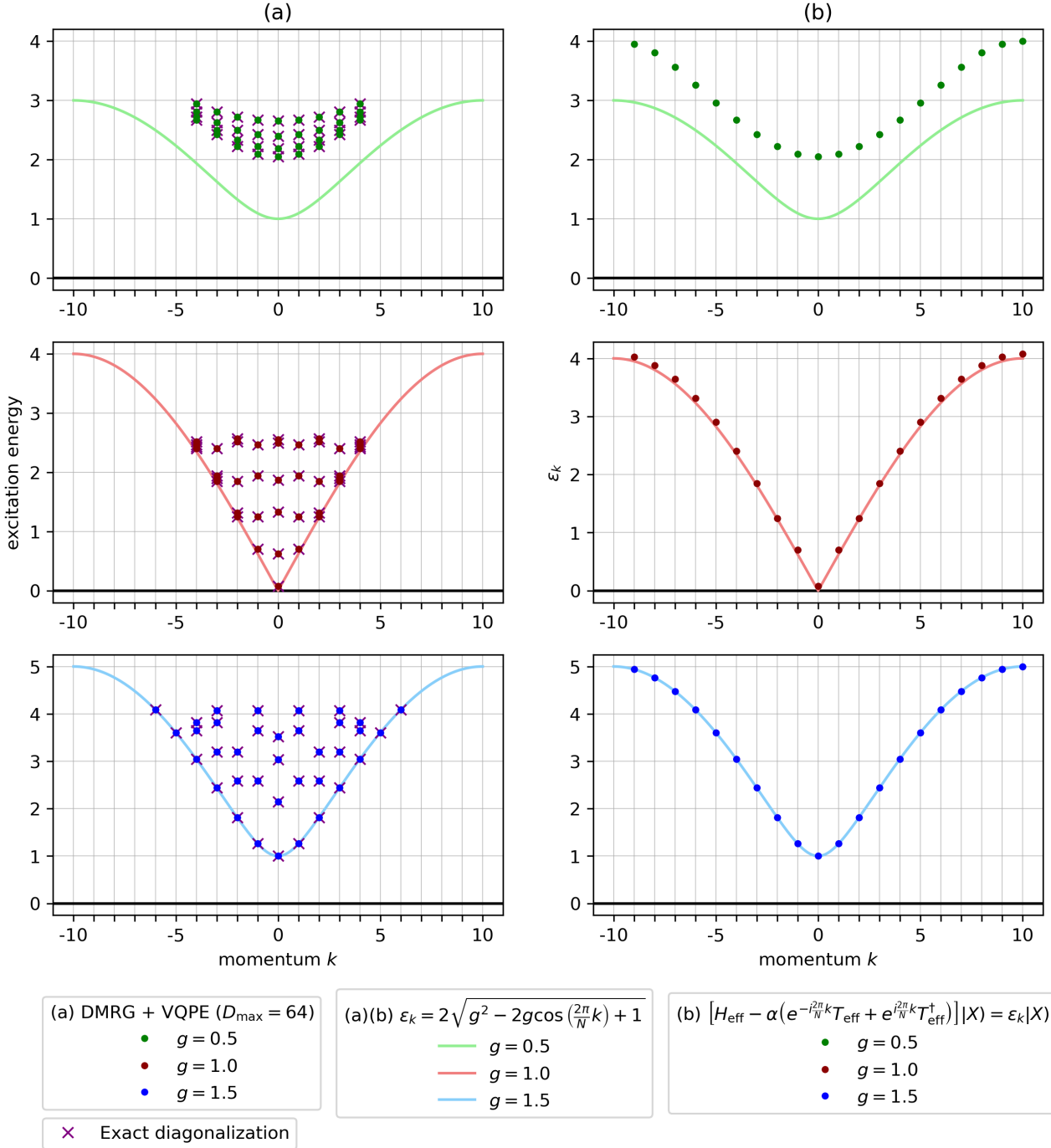


Figure 5.2: TFI benchmark for variational quasiparticle excitations on top of a finite MPS ground state. We choose PBC for the Hamiltonian, chain length $N = 20$ and maximal bond dimension $D_{\max} = 64$. On the left side (a), we first diagonalize the Hamiltonian and afterwards the translation operator within each energy-degenerate eigenspace. We compare the results to exact diagonalization and the single particle dispersion obtained from the Jordan-Wigner mapping to free fermions (in the odd parity sector). The lowest-lying domain wall excitations in the ferromagnetic phase $g < 1$ are not eigenstates of the periodic Hamiltonian. The right side (b) shows the benchmark for quasiparticle excitations variational in energy and momentum. We include the Hermitian translation operator $-\alpha(e^{-i2\pi k/N}T_{\text{eff}} + e^{i2\pi k/N}T_{\text{eff}}^\dagger)$ directly in the effective eigenvalue equation. This frees us from computing multiple excitations of the same momentum, whose energies lie below the first excitation of other momenta.

Local energies and OBC

Going from periodic to open boundary conditions for the Hamiltonian, it does no longer commute with the translation operator. As a consequence, the excitations cannot be momentum eigenstates anymore. Nevertheless, we expect standing wave configurations of the very same dressed particle [VDVH⁺21]. This can be understood easiest in the single particle picture, known from the perturbative approach in section 2.2. For the effective Hamiltonian

$$H_{\text{eff}} = \mu \sum_n |n\rangle \langle n| - t \sum_n (|n\rangle \langle n+1| + |n+1\rangle \langle n|), \quad (5.39)$$

we want to compare the local energies, i.e. the expectation values of

$$h_{n,n+1} = \frac{\mu}{2} |n\rangle \langle n| + \frac{\mu}{2} |n+1\rangle \langle n+1| - t (|n\rangle \langle n+1| + |n+1\rangle \langle n|) \quad (5.40)$$

for the respective eigenstates. For both boundary conditions, they can be labeled by a wave number p such that

$$H_{\text{eff}} = \sum_p \epsilon_p |p\rangle \langle p| \text{ with } \epsilon_p = \mu - 2t \cos(p). \quad (5.41)$$

For the TFI model with large g and $J = 1$, on-site energy and hopping take the values $\mu = 2g$ and $t = 1$.

1) PBC: The eigenstates are plane waves

$$|p\rangle = \frac{1}{\sqrt{N}} \sum_n e^{ipn} |n\rangle \text{ with } p = \frac{2\pi}{N} k \text{ and } k = 0, \pm 1, \dots, \pm \left(\frac{N}{2} - 1 \right), \frac{N}{2}. \quad (5.42)$$

While the pure momentum states $|\pm p\rangle$ have constant local energy $\langle h_{n,n+1} \rangle = \epsilon_p/N = \epsilon_{-p}/N$, their equal weighted superpositions show spatial oscillations:

$$\begin{aligned} |p+\rangle &= \frac{1}{\sqrt{2}} (|p\rangle + |-p\rangle) = \sqrt{\frac{2}{N}} \sum_n \cos(pn) |n\rangle, \\ \langle h_{n,n+1} \rangle_+ &= \left[\mu \cos^2 \left(\frac{2\pi kn}{N} \right) + \mu \cos^2 \left(\frac{2\pi k(n+1)}{N} \right) - 4t \cos \left(\frac{2\pi kn}{N} \right) \cos \left(\frac{2\pi k(n+1)}{N} \right) \right] / N, \\ |p-\rangle &= \frac{1}{\sqrt{2}} (|p\rangle - |-p\rangle) = i \sqrt{\frac{2}{N}} \sum_n \sin(pn) |n\rangle, \\ \langle h_{n,n+1} \rangle_- &= \left[\mu \sin^2 \left(\frac{2\pi kn}{N} \right) + \mu \sin^2 \left(\frac{2\pi k(n+1)}{N} \right) - 4t \sin \left(\frac{2\pi kn}{N} \right) \sin \left(\frac{2\pi k(n+1)}{N} \right) \right] / N. \end{aligned}$$

2) OBC: For Dirichlet "vanishing edge" conditions $\psi_0 = \psi_{N+1} = 0$, the solutions are standing waves with nodes at the boundaries. They provide a finer resolution in wave numbers k , which are confined to half the Brillouin zone:

$$\begin{aligned} |p\rangle &= \sqrt{\frac{2}{N+1}} \sum_n \sin(pn) |n\rangle \text{ with } p = \frac{\pi}{N+1} k \text{ and } k = 1, \dots, N, \\ \langle h_{n,n+1} \rangle &= \left[\mu \sin^2 \left(\frac{\pi kn}{N+1} \right) + \mu \sin^2 \left(\frac{\pi k(n+1)}{N+1} \right) - 4t \sin \left(\frac{\pi kn}{N+1} \right) \sin \left(\frac{\pi k(n+1)}{N+1} \right) \right] / (N+1). \end{aligned}$$

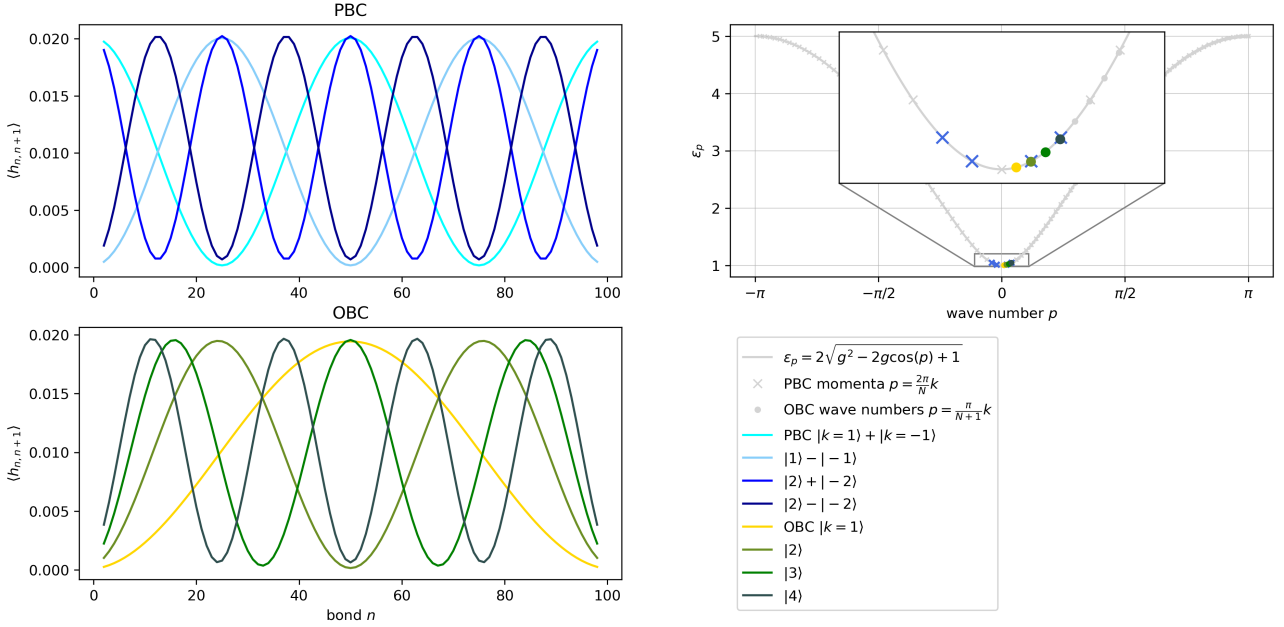


Figure 5.3: TFI benchmark for the quasiparticle excitation waves with PBC and OBC. For $g = 1.5$, $N = 100$ and $D_{\max} = 64$ we compute the four lowest-lying MPS quasiparticle excitations. For OBC the local energies describe standing wave configurations with nodes at the boundary and corresponding wave numbers confined to half the Brillouin zone. For PBC the momenta are distributed symmetrically in both halves of the Brillouin zone and the superpositions of $\pm k$ eigenstates show periodic oscillations in the local energies, without nodes.

For an MPS quasiparticle excitation (5.28), a local energy expectation value leads to the double sum

$$\langle \psi(\overline{B}; \overline{A}) | h^{[n, n+1]} | \psi(B; A) \rangle = \sum_{m, \tilde{m}} \langle \psi(\overline{B}^{[\tilde{m}]}; \overline{A}) | h^{[n, n+1]} | \psi(B^{[m]}; A) \rangle. \quad (5.43)$$

We efficiently combine the terms where $B^{[m]}$ and/or $\overline{B}^{[\tilde{m}]}$ are at positions $m, \tilde{m} \notin \{n, n+1\}$ in the following environment tensors, all computed recursively starting from zero tensors at $n = 0$ or $n = N + 1$:

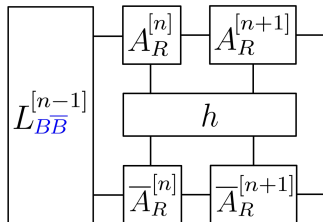
$$\begin{aligned}
 L_{\overline{B}\overline{B}}^{[n]} &= \begin{array}{c} \text{---} \\ \text{---} \end{array} \left(\begin{array}{c} B^{[n]} \\ \overline{B}^{[n]} \end{array} \right) + \begin{array}{c} \text{---} \\ \text{---} \end{array} \left(\begin{array}{c} A_R^{[n]} \\ \overline{A}_R^{[n]} \end{array} \right) \quad (n = 1, \dots, N-2), \\
 R_B^{[n]} &= \begin{array}{c} \text{---} \\ \text{---} \end{array} \left(\begin{array}{c} B^{[n]} \\ \overline{A}_R^{[n]} \end{array} \right) + \begin{array}{c} \text{---} \\ \text{---} \end{array} \left(\begin{array}{c} A_L^{[n]} \\ \overline{A}_R^{[n]} \end{array} \right) R_B^{[n+1]}, \\
 R_{\overline{B}}^{[n]} &= \begin{array}{c} \text{---} \\ \text{---} \end{array} \left(\begin{array}{c} A_R^{[n]} \\ \overline{B}^{[n]} \end{array} \right) + \begin{array}{c} \text{---} \\ \text{---} \end{array} \left(\begin{array}{c} A_R^{[n]} \\ \overline{A}_L^{[n]} \end{array} \right) R_{\overline{B}}^{[n+1]},
 \end{aligned} \quad (5.44)$$

$$R_{\overline{B}\overline{B}}^{[n]} = B^{[n]} \left(R_{\overline{B}}^{[n+1]} + \overline{A}_L^{[n]} R_{\overline{B}}^{[n+1]} \right) + A_L^{[n]} \left(R_B^{[n+1]} + \overline{B}^{[n]} R_B^{[n+1]} \right) \quad (n = N, \dots, 3).$$

With these boundary tensors the higher level tensor diagram reads

$$\langle \psi(\overline{B};\overline{A}) | h^{[n,n+1]} | \psi(B;A) \rangle$$

三



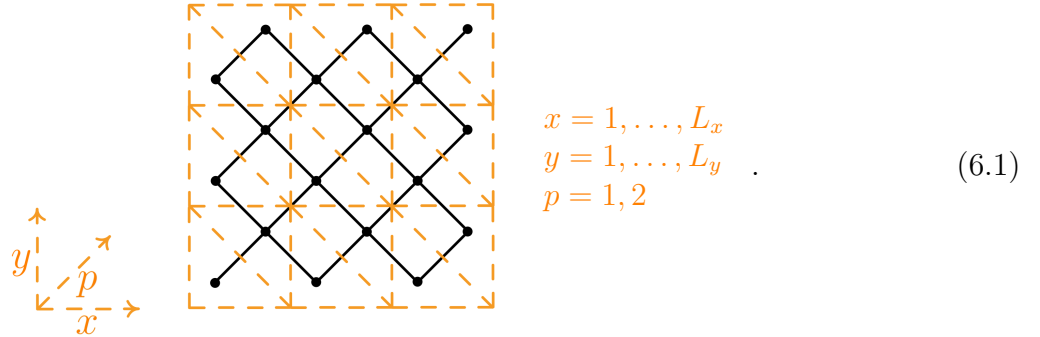
(5.45)

At $g = 1.5$, for $N = 100$ and $D_{\max} = 64$, we contract these networks for the four lowest-lying MPS quasiparticle excitations, both for PBC and OBC. The results meet the expectations, as demonstrated in figure 5.3. The bond energies show the correct spatial oscillations and reveal the wave numbers. The corresponding total energies lie on the analytical dispersion curve.

Chapter 6

Isometric projected entangled pair states (isoPEPS)

We consider a *diagonal square lattice*, obtained from a 45-degree rotation of the conventional square lattice. Formally, it is defined as an $L_x \times L_y$ square *Bravais lattice* (rescaled by $\sqrt{2}$), plus a two-spin *basis* indexed by p :



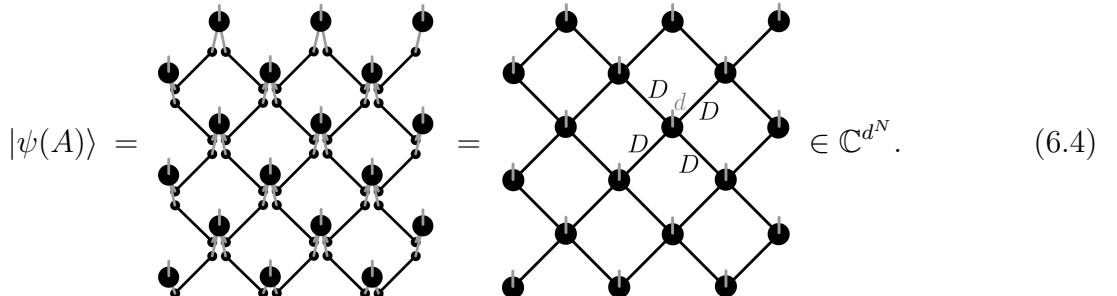
Between all nearest neighbors of the $N = 2L_x L_y$ sites, we distribute pairs of maximally entangled D -dimensional ancilla spins:

$$\text{---} = \sum_{\alpha=1}^D |\alpha\alpha\rangle \in \mathbb{C}^D \otimes \mathbb{C}^D. \quad (6.2)$$

At each site, we then apply the following projection onto a single d -dimensional physical spin:

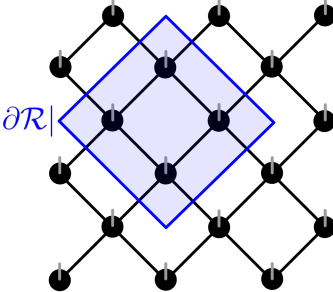
$$\text{---} = \sum_{s,\alpha,\beta,\gamma,\delta} A_{\alpha\beta\gamma\delta}^s |s\rangle (\alpha\beta\gamma\delta| \in \mathbb{C}^{d \times D^4}. \quad (6.3)$$

This constructs a *projected entangled pair state* (PEPS) [VC04] characterized by the five leg tensor $A \in \mathbb{C}^{d \times D \times D \times D \times D}$:



Even though the ancilla spins are only locally entangled, the resulting correlations in the physical PEPS can be long-ranged. This is a consequence of *entanglement swapping*, that is implemented through the sequence of projections applied to the entangled pairs. Nevertheless, the local connectivity of tensors with finite bond dimension enforces the *area law*. Specifically,

the total amount of entanglement between a subregion \mathcal{R} of spins and its complement is upper bounded by the size of the boundary $|\partial\mathcal{R}|$:



$$S(\psi_A) = -\text{tr}[\rho_{\mathcal{R}} \log \rho_{\mathcal{R}}] \leq |\partial\mathcal{R}| \log D. \quad (6.5)$$

Although not rigorously proven in two dimensions, it is conjectured that ground states of local, gapped Hamiltonians fulfill a generalization of (4.26) with the form of (6.5), i.e. that PEPS can faithfully represent 2D ground states [CPGSV21].

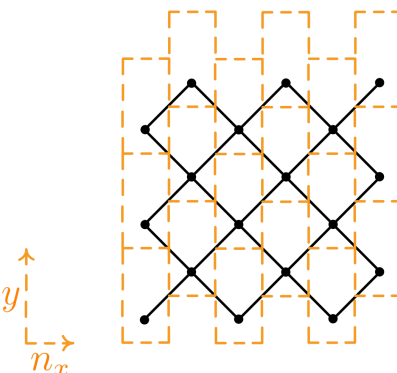
Note that we impose open boundary conditions, which reduce the number of nearest neighbors at the edges and require the affected tensors to be adjusted in dimensions accordingly—for example, by taking slices of the bulk tensor A . As we will specify in the following section, we allow the tensors to be site-dependent anyway.

6.1 Imposed canonical form and Yang-Baxter move

By cutting a single leg, one cannot disconnect the tensor network (6.4) into two disjoint parts free from any loops. This makes it impossible to bring a general PEPS into canonical form as we know it for MPS. Even if one removes inter-loops by cutting multiple legs, the remaining intra-loops still prevent the subsystems from being orthonormalized. In particular, one cannot isolate an orthogonality center with ingoing legs only within the PEPS gauge freedom. To circumvent this, we impose an isometric form, restricting the variational class to a strict PEPS subset: the *isometric projected entangled pair states* (isoPEPS). They were introduced by [ZP20] and computationally investigated in more technical detail by [LZP22], both for the conventional square lattice. In our work, we adopt the rotated version developed in the Master's thesis [Sap24, SKZP25].

Imposed canonical form

Being more convenient for indexing the isometric tensors, we introduce columns $n_x = 2(x-1)+p$ in our lattice (6.1):



$$n_x = 1, \dots, 2L_x \\ y = 1, \dots, L_y \quad . \quad (6.6)$$

We choose one *orthogonality column* $n_x^c \in \{0, 1, \dots, 2L_x\}$ and demand the A -tensors for $n_x \leq n_x^c$ to be left isometric and those for $n_x > n_x^c$ to be right isometric, in the following way:

$$A_L^{[n_x \leq n_x^c, y]} = \begin{array}{c} D_{lu} \\ \diagdown \\ d \\ \diagup \\ D_{ld} \end{array} \quad \text{with} \quad \begin{array}{c} D_{ru} \\ \diagup \\ d \\ \diagdown \\ D_{rd} \end{array} = \begin{array}{c} \swarrow \\ \searrow \end{array}, \quad (6.7)$$

$$A_R^{[n_x > n_x^c, y]} = \begin{array}{c} D_{lu} \\ \diagup \\ d \\ \diagdown \\ D_{ld} \end{array} \quad \text{with} \quad \begin{array}{c} D_{ru} \\ \diagup \\ d \\ \diagdown \\ D_{rd} \end{array} = \begin{array}{c} \searrow \\ \swarrow \end{array}. \quad (6.8)$$

Between $A_L^{[n_x^c]}$ and $A_R^{[n_x^c+1]}$ we then insert a column $C^{[n_x^c]}$ of rank-4 auxiliary tensors $C^{[n_x^c, n_y]}$ for $n_y = 1, \dots, 2L_y - 1$. We complete the ingoing arrows from left and right with vertical arrows pointing towards a single *orthogonality center* (n_x^c, n_y^c) . In other words, there is a normalized center tensor $C_C^{[n_x^c, n_y^c]}$, connected to *up isometries* $C_U^{[n_x^c, n_y > n_y^c]}$ from above and to *down isometries* $C_D^{[n_x^c, n_y < n_y^c]}$ from below:

$$C_U^{[n_x^c, n_y > n_y^c]} = \begin{array}{c} \chi_u \\ D_l \rightarrow \bullet \leftarrow D_r \end{array} \quad \text{with} \quad \begin{array}{c} \chi_u \\ \uparrow \\ \chi_d \\ \downarrow \end{array} = \begin{array}{c} \nearrow \\ \searrow \end{array}, \quad (6.9)$$

$$C_C^{[n_x^c, n_y^c]} = \begin{array}{c} \chi_u \\ D_l \rightarrow \bullet \leftarrow D_r \end{array} \quad \text{with} \quad \begin{array}{c} \chi_u \\ \downarrow \\ \chi_d \\ \uparrow \end{array} = 1, \quad (6.10)$$

$$C_D^{[n_x^c, n_y < n_y^c]} = \begin{array}{c} \chi_u \\ D_l \rightarrow \bullet \leftarrow D_r \end{array} \quad \text{with} \quad \begin{array}{c} \chi_u \\ \downarrow \\ \chi_d \\ \uparrow \end{array} = \begin{array}{c} \swarrow \\ \searrow \end{array}. \quad (6.11)$$

A set of tensors (6.7)–(6.11) defines an *isometric projected entangled pair state* (isoPEPS):

$$|\psi(A_L, C, A_R)\rangle = \begin{array}{c} \text{Diagram showing a 3x3 grid of spins with arrows indicating left (down) and right (up) isometries. The center spin is labeled } C_C^{[3,3]}. \text{ The top row is labeled } A_R^{[6,3]}, \text{ the bottom row } A_L^{[1,1]}, \text{ and the left column } A_L^{[1,1]}, A_L^{[2]}, A_L^{[3]}, \text{ and the right column } A_R^{[4]}, A_R^{[5]}, A_R^{[6]}. \text{ The center column is labeled } C_U^{[3,5]}, \text{ the middle row } C_D^{[3,1]}, \text{ and the rightmost column } A_R^{[6,3]}. \end{array} . \quad (6.12)$$

As in all diagrams in this chapter, we draw the diagonal lattice with $L_x = L_y = 3$ and $N = 2L_x L_y = 18$ spins. For the orthogonality center we exemplarily choose $(n_x^c, n_y^c) = (3, 3)$. Note that we generally refer to both the indices n_x^c and (n_x^c, n_y^c) , as well as the corresponding

tensors $C^{[n_x^c]}$ and $C_C^{[n_x^c, n_y^c]}$, as the orthogonality column and orthogonality center, respectively.

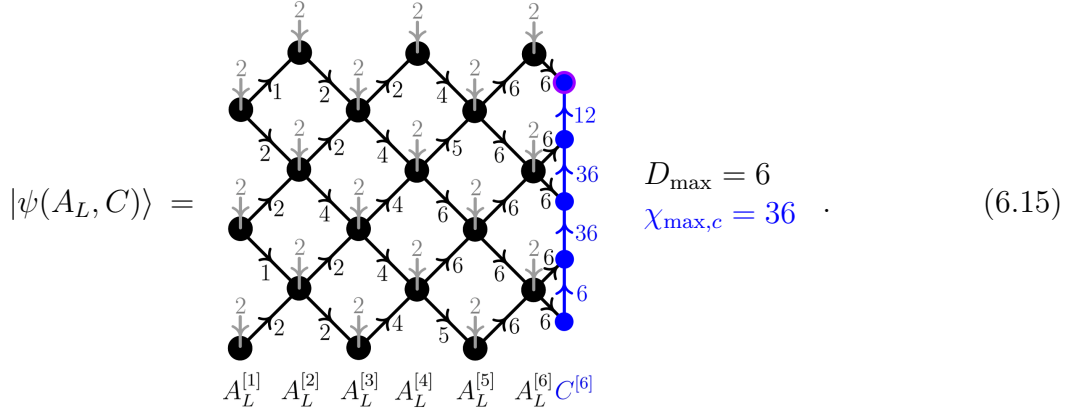
Following the analogy with physical MPS in chapter 5, the orthogonality column $C^{[n_x^c]}$ can be interpreted as an MPS, with d and u the virtual legs and rl the "physical" leg (the quotation marks indicate it is not an actual spin degree of freedom). We refer to this as a *column MPS* (cMPS). In addition to the dimension constraints set by the boundaries and the isometric conditions (ingoing \geq outgoing), we impose upper bounds D_{\max} and $\chi_{\max,c}$ for the virtual lattice and column legs:

$$D_{ld}, D_{lu}, D_{rd}, D_{ru}, D_l, D_r \leq D_{\max}, \quad \chi_d, \chi_u \leq \chi_{\max,c}. \quad (6.13)$$

In this thesis, we work with $D_{\max} \leq 6$ and

$$\chi_{\max,c} = 6D_{\max}. \quad (6.14)$$

To get an intuition for how the bond dimensions grow to their maximum value, we show a possible distribution for $D_{\max} = 6$ and orthogonality column on the very right:

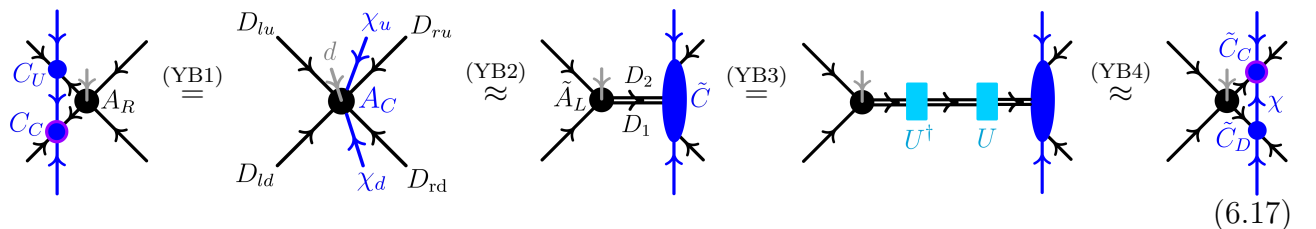


Yang-Baxter move

The orthogonality center can be moved up/down error-free by performing a QR decomposition of C_C and absorbing the normalized triangular matrix into the isometry above/below. Moving the orthogonality column left/right is a more involved, in general error-prone procedure. On the column level, it aims at solving the problem

$$C^{[n_x]} A_R^{[n_x+1]} \approx \tilde{A}_L^{[n_x+1]} \tilde{C}^{[n_x+1]}. \quad (6.16)$$

One approach is to variationally minimize $\|C^{[n_x]} A_R^{[n_x+1]} - \tilde{A}_L^{[n_x+1]} \tilde{C}^{[n_x+1]}\|_2$ by sweeping over the individual tensors $\tilde{A}_L^{[n_x+1,y]}$ and $\tilde{C}^{[n_x+1,n_y]}$ (for shift to the right). Achieving accuracy close to optimal while being much faster, we instead employ a sequential tripartite contraction-decomposition scheme, referred to as *Yang-Baxter move* due to its diagrammatic resemblance to the Yang-Baxter equation:



- (YB1) Contract C_C , C_U and A_R into a single normalized tensor A_C .
- (YB2) Perform a truncated SVD of $A_C \in \mathbb{C}^{(D_{ld}D_{lu}d) \times (\chi_d D_{rd}D_{ru}\chi_u)}$. Extract the new left isometry \tilde{A}_L and multiply singular value matrix and right isometry to a new center tensor \tilde{C} :

$$A_C \xrightarrow{\text{tSVD}} \tilde{A}_L \tilde{C} \quad \text{with } \tilde{A}_L \in \mathbb{C}^{(D_{ld}D_{lu}d) \times \mathbb{D}}, \tilde{C} \in \mathbb{C}^{\mathbb{D} \times (\chi_d D_{rd}D_{ru}\chi_u)}, \quad (6.18)$$

$$\mathbb{D} = \min(D_{ld}D_{lu}d, \chi_d D_{rd}D_{ru}\chi_u, D_{\max}^2).$$

Split the leg of dimension \mathbb{D} into two legs of dimensions D_1, D_2 as evenly as possible under minimization of $\mathbb{D} - D_1 D_2 \geq 0$.

- (YB3) The decomposition $A_C \approx \tilde{A}_L \tilde{C}$ has the gauge freedom $\tilde{A}_L \rightarrow \tilde{A}_L U^\dagger$, $\tilde{C} \rightarrow U \tilde{C}$ for any unitary $U \in \mathbb{C}^{D_1 D_2 \times D_1 D_2}$. In anticipation of the truncated splitting (6.22) of \tilde{C} into \tilde{C}_D and \tilde{C}_C , we choose U as their *disentangler*. More precisely, we solve the variational problem

$$\arg \min_{U \in \text{GL}(D_1 D_2, \mathbb{C})} \mathcal{L}(U \tilde{C}) \quad (6.19)$$

for a cost function \mathcal{L} whose minimization leads to a smaller truncation error

$$\mathcal{E}_{\text{trunc}}(U \tilde{C}) = \|U \tilde{C} - (\tilde{C}_D)_{[:,:\chi]} S_{[:,\chi,:]} V_{[:,\chi,:]} \|_2 = \left(\sum_{\mu > \chi} S_\mu^2 \right)^{1/2}. \quad (6.20)$$

In [SKZP25] it was found that directly using $\mathcal{E}_{\text{trunc}}$ as cost function does not yield the smallest global error for shifting the whole orthonormality column (6.16). The best results were obtained with the Rényi-entropy

$$\mathcal{R}_\alpha(U \tilde{C}) = \frac{1}{1-\alpha} \log \text{tr}_u \left[\left(\text{tr}_d |U \tilde{C}|(\overline{U \tilde{C}}|)^\alpha \right) \right] = \frac{1}{1-\alpha} \log \left(\sum_\mu S_\mu^{2\alpha} \right), \quad (6.21)$$

for $\alpha = 1/2$. The partial traces are taken over all down, up legs of dimensions $D_1 \chi_d D_{rd}, D_{ru} \chi_u D_2$. Note that $\mathcal{E}_{\text{trunc}}$ is upper bounded by \mathcal{R}_α for all $\alpha < 1$. For a detailed description of the Riemannian Trust-Region Method (TRM), used to solve (6.19) for $\mathcal{R}_{\alpha=1/2}$, we refer the reader to [SKZP25, LZP22].

- (YB4) Split $\tilde{C} \in \mathbb{C}^{(D_1 \chi_d D_{rd}) \times (D_{ru} \chi_u D_2)}$ into down isometric \tilde{C}_D and normalized \tilde{C}_C via truncated SVD:

$$\tilde{C} \xrightarrow{\text{tSVD}} \tilde{C}_D \tilde{C}_C \quad \text{with } \tilde{C}_D \in \mathbb{C}^{(D_1 \chi_d D_{rd}) \times \chi}, \tilde{C}_C \in \mathbb{C}^{\chi \times (D_{ru} \chi_u D_2)}, \quad (6.22)$$

$$\chi = \min(D_1 \chi_d D_{rd}, D_{ru} \chi_u D_2, \chi_{\max,c}).$$

Starting from C_C at $(n_x, 1)$, we can shift the whole orthogonality column to the right and end up with \tilde{C}_C at $(n_x + 1, 2L_y - 1)$ by repeating (YB1)–(YB4) L_y times, each (apart from the last one) followed by moving C_C up to the next site. Depending on the parity of n_x , the decomposition at the very bottom or top reduces to a bipartition, so steps (YB3) and (YB4) are omitted in that case. To instead move the center from top to bottom, i.e. from $(n_x, 2L_y - 1)$ to $(n_x + 1, 1)$, one just has to reverse the direction of the final truncated SVD in (YB4). Since the respective shifts to the left result from mirroring along the y-axis, they don't have to be implemented separately.

6.2 Boundary compression

Column MPO Hamiltonian

We can write any Hamiltonian $H = H^\dagger \in \mathbb{C}^{d^{2L_x L_y} \times d^{2L_x L_y}}$ with nearest-neighbor interactions as a sum of zig-zag MPOs $h^{[n_x, n_x+1]}$ that act nontrivially only on two adjacent columns of physical sites:

$$H = \sum_{n_x=1}^{2L_x-1} \mathbb{1}^{[1]} \otimes \cdots \otimes \mathbb{1}^{[n_x-1]} \otimes h^{[n_x, n_x+1]} \otimes \mathbb{1}^{[n_x+2]} \otimes \cdots \otimes \mathbb{1}^{[2L_x]},$$

$h^{[n_x, n_x+1]} =$

for n_x odd ,

for n_x even .

(6.23)

For the TFI model (2.1) with OBC, the MPO tensors $W^{[n_x, n_y]}$ are given by

$$\begin{aligned} & W^{[n_x, 1]} \quad W^{[n_x, 2]}, \dots, W^{[n_x, 2L_y-1]} \quad W^{[n_x, 2L_y]} \\ & (\mathbb{1} \quad \sigma^x \quad -g^{[n_x, 1]}\sigma^z), \quad \begin{pmatrix} \mathbb{1} & \sigma^x & -g^{[n_x, n_y]}\sigma^z \\ 0 & 0 & -J\sigma^x \\ 0 & 0 & \mathbb{1} \end{pmatrix}, \quad \begin{pmatrix} -g^{[n_x, 2L_y]}\sigma^z \\ -J\sigma^x \\ \mathbb{1} \end{pmatrix}. \end{aligned} \quad (6.24)$$

For all spins that are involved in two MPOs (all except the leftmost and rightmost), the transverse field strengths have to be halved:

$$g^{[n_x, n_y]} = \begin{cases} g & \text{if } n_x = 1, n_y \text{ odd} \\ g & \text{if } n_x = 2L_x - 1, n_y \text{ even} \\ g/2 & \text{else} \end{cases} \quad (6.25)$$

For an isoPEPS (6.12), we now develop two different ways to compute the expectation value E of a Hamiltonian (6.23). Without performing any contractions, it has the diagrammatic representation

$$E = \begin{array}{c} \text{Diagram 1} \end{array} + \begin{array}{c} \text{Diagram 2} \end{array} + \begin{array}{c} \text{Diagram 3} \end{array} + \begin{array}{c} \text{Diagram 4} \end{array} + \begin{array}{c} \text{Diagram 5} \end{array} . \quad (6.26)$$

1) Yang-Baxter energy

One way to compute (6.26) is to move the orthogonality column with Yang-Baxter moves right next to every column MPO in the sum, and to use the isometry condition for all A_L, A_R tensors on which the MPO does not act:

$$E_{\text{YB}} = \sum_{n_x=1}^{2L_x-1} \quad \begin{array}{c} \text{Diagram showing a 2D grid of tensors with a central vertical column highlighted in green, representing the orthogonality column.} \\ \left(\begin{array}{c|c} \overline{A}_L^{[n_x]} \overline{A}_L^{[n_x+1]} & \overline{C}^{[n_x+1]} \\ h^{[n_x, n_x+1]} & C^{[n_x+1]} \\ \hline A_L^{[n_x]} A_L^{[n_x+1]} & \end{array} \right) \end{array} \quad . \quad (6.27)$$

2) Boundary compression energy

In section 6.3, we want to take the derivative of (6.26) with respect to tensors on the orthogonality column in order to find the ground state. This requires an alternative computation of the energy, where we keep the orthogonality column fixed at n_x^c . We additively summarize all terms where $h^{[n_x, n_x+1]}$ acts left ($n_x < n_x^c$) and right ($n_x > n_x^c$) of the orthogonality column into environments $L_h^{[n_x^c]}$ and $R_h^{[n_x^c+1]}$, respectively. They are defined more precisely below. The third contribution comes from $h^{[n_x^c, n_x^c+1]}$ acting on $A_L^{[n_x^c]}$ and $A_R^{[n_x^c+1]}$, which enclose the orthogonality column:

$$E_{\text{bc}} = \quad \begin{array}{c} \text{Diagram showing three separate parts: } L_h^{[n_x^c]}, \text{ a central column with tensors, and } R_h^{[n_x^c+1]}. \\ + \quad \begin{array}{c} \text{Diagram showing a 2D grid of tensors with a central vertical column highlighted in green, representing the orthogonality column.} \\ \left(\begin{array}{c|c} \overline{A}_L^{[n_x^c]} & \overline{C}^{[n_x^c]} \\ h_L^{[n_x^c, n_x^c+1]} & C^{[n_x^c]} \\ \hline A_L^{[n_x^c]} & \end{array} \right) \end{array} \quad + \quad \begin{array}{c} \text{Diagram showing a 2D grid of tensors with a central vertical column highlighted in green, representing the orthogonality column.} \\ \left(\begin{array}{c|c} \overline{A}_R^{[n_x^c+1]} & \overline{C}^{[n_x^c+1]} \\ h_R^{[n_x^c, n_x^c+1]} & C^{[n_x^c+1]} \\ \hline A_R^{[n_x^c+1]} & \end{array} \right) \end{array} \end{array} \quad . \quad (6.28)$$

Boundary MPS

We initialize $L_h^{[1]} = R_h^{[2L_x]} = 0$ and define the rest of the energy environments recursively as

$$\left(\begin{array}{c} | \\ L_h^{[n_x]} \end{array} \right) = \left(\begin{array}{c} | \\ \overline{A}_L^{[n_x-1]} \overline{A}_L^{[n_x]} \\ h^{[n_x-1, n_x]} \\ A_L^{[n_x-1]} A_L^{[n_x]} \end{array} \right) + \left(\begin{array}{c} | \\ \overline{A}_L^{[n_x]} \\ A_L^{[n_x]} \end{array} \right) \quad (n_x = 2, \dots, 2L_x), \quad (6.29)$$

$$\left| \begin{array}{c} R_h^{[n_x]} \end{array} \right) = \left| \begin{array}{c} | \\ \overline{A}_R^{[n_x]} \overline{A}_R^{[n_x+1]} \\ h^{[n_x, n_x+1]} \\ A_R^{[n_x]} A_R^{[n_x+1]} \end{array} \right) + \left| \begin{array}{c} | \\ \overline{A}_R^{[n_x]} \\ A_R^{[n_x]} \end{array} \right| R_h^{[n_x+1]} \quad (n_x = 2L_x - 1, \dots, 1). \quad (6.30)$$

Since up to a horizontal left \leftrightarrow right flip of the A_R -tensors, $R_h^{[n_x]}$ has the same structure as $L_h^{[n_x]}$, it is enough to concentrate on the latter from now on. In the same way, after a vertical down \leftrightarrow up flip of all involved tensors, $L_h^{[n_x]}$ for odd n_x is in identical form to $L_h^{[n_x]}$ for even n_x (the version drawn above):

$$\left(\begin{array}{c} | \\ L_h^{[n_x]} \end{array} \right) = \left(\begin{array}{c} | \\ \overline{A}_L^{[n_x-1]} \overline{A}_L^{[n_x]} \\ h^{[n_x-1, n_x]} \\ A_L^{[n_x-1]} A_L^{[n_x]} \end{array} \right) + \left(\begin{array}{c} | \\ \overline{A}_L^{[n_x]} \\ A_L^{[n_x]} \end{array} \right) \quad (n_x \text{ odd}). \quad (6.31)$$

Interpreting the open ket and bra lattice legs as a double "physical" leg, we can treat $L_h^{[n_x]}$ as a *boundary MPS* (bMPS).

In principle, we can compute $L_h^{[n_x]}$ exactly by allowing a maximal bMPS bond dimension of

$$\chi_{\max,b}^{\text{exact}} = D_{\max}^{2(L_y-1)}. \quad (6.32)$$

Due to the exponential growth of $\chi_{\max,b}^{\text{exact}}$ with L_y (e.g. $\chi_{\max,b}^{\text{exact}} = 1,048,576$ for $L_y = 6$ and $D_{\max} = 4$), the exact contraction becomes infeasible in practice. As a consequence, we need a method that efficiently compresses $L_h^{[n_x]}$ to a moderate bond dimension $\chi_{\max,b}$, without loosing too much information about the effective Hamiltonian. For the DMRG² algorithm in section 6.3, we take

$$\chi_{\max,b} = 6D_{\max}^2. \quad (6.33)$$

Variational boundary compression

The standard procedure for compressing a bMPS is variational optimization [Orú14]. For $(L_h|$ in (6.29), we denote the first term (that newly applies h to the identity boundary) as $(L_h^{\text{new}}|$, and the second term (that transfers the boundary of all hs that already have been applied) as $(L_h^{\text{transfer}}|$. With this we can formulate one local update of $\theta_2^{[n_y, n_y+1]}$, a two-site tensor of $(L_h|$, as the minimization problem

$$\arg \min_{\theta_2^{[n_y, n_y+1]}} \left\| (L_h(\theta_2)| - (L_h^{\text{new}}| - (L_h^{\text{transfer}}|) \right\|_2^2. \quad (6.34)$$

Taking the derivative of the norm cost function with respect to $\bar{\theta}_2$ gives the solution

$$\theta_2^{[n_y, n_y+1]} = (L_h^{\text{new}} | \partial_{\bar{\theta}_2} L_h(\bar{\theta}_2)) + (L_h^{\text{transfer}} | \partial_{\bar{\theta}_2} L_h(\bar{\theta}_2)) = \|\mathcal{L}_h\| \cdot \xrightarrow{\text{tSVD}} \frac{\chi_{\max,b}}{\|\mathcal{L}_h\|} \cdot \|\mathcal{L}_h\| \cdot \cdot \cdot . \quad (6.35)$$

Note that θ_2 contains the global norm $\|\mathcal{L}_h\|$. We extract it before performing the truncated SVD, that splits $\theta_2^{[n_y, n_y+1]}$ into $U^{[n_y]}$, $S^{[n_y]}$ and $V^{[n_y+1]}$ and allows moving to the next site. We start from an initial random guess for $(L_h|$ and sweep up and down with the local updates (6.35) until the θ_2 s do not change significantly anymore. The most expensive part regarding computational runtime is the SVD with complexity

$$\mathcal{O}(D_{\max}^6 \chi_{\max,b}^3). \quad (6.36)$$

Bulk-weighted boundary compression

Apart from the identity contractions of the A_L s left of h , the variational boundary compression (6.35) is a general PEPS procedure that does not explicitly use the isometric structure. We now want to develop a new compression method that does so, by weighting the boundary truncations according to the singular values contained in the orthogonality column. To be precise, we require $(L_h|$ and $(L_h^{\text{new}}| + (L_h^{\text{transfer}}|$ to (approximately) have the same expectation value with the double orthogonality column $|C\bar{C}\rangle$ right next to them. Due to the isometric structure, the latter contains the entire information about the right bulk:

$$\left(\begin{array}{c|c} \overline{A}_L^{[n_x-1]} \overline{A}_L^{[n_x]} & \overline{C}^{[n_x]} \\ \hbar^{[n_x-1, n_x]} & C^{[n_x]} \\ \hline A_L^{[n_x-1]} A_L^{[n_x]} & \end{array} \right) + \left(\begin{array}{c|c} L_h^{[n_x-1]} & \overline{A}_L^{[n_x]} \\ \hbar & \overline{C}^{[n_x]} \\ \hbar^{[n_x]} & C^{[n_x]} \\ \hbar^{[n_x]} & \end{array} \right) \approx \left(\begin{array}{c|c} L_h^{[n_x]} & \overline{C}^{[n_x]} \\ \hbar & C^{[n_x]} \\ \hbar^{[n_x]} & \end{array} \right). \quad (6.37)$$

We first bring $(L_h^{\text{new}}|$, $(L_h^{\text{transfer}}|$ and $|C\bar{C}\rangle$ in bMPS form with single tensor per site, via QR decomposition and leg merging:

$$\text{Diagram showing the QR decomposition and leg merging process: } \text{PEPS} \xrightarrow{\text{QR}} \text{Simplified PEPS} \xrightarrow{\text{QR}} \text{bMPS} \xrightarrow{\text{absorb}} \text{bMPS} \quad (6.38)$$

We take $|C\bar{C}\rangle$ in its thereby achieved down isometric form and discard its global norm. We reformulate (6.37) as finding an $(L_h|$ that (a) has down isometric form, (b) global norm $\|L_h\|$, (c) maximal bond dimension $\chi_{\max,b}$ and (d) fulfills

$$\left(\begin{array}{c} \text{green arrows} \\ \text{blue arrows} \end{array} \right) + \left(\begin{array}{c} \text{blue arrows} \\ \text{blue arrows} \end{array} \right) \approx \|L_h\| \cdot \left(\begin{array}{c} \text{green arrows} \\ \text{blue arrows} \\ \text{green arrows} \\ \text{blue arrows} \end{array} \right) \quad (6.39)$$

From top to bottom, we compute the expectation values $(L_h^{\text{new}}|C\bar{C})$ and $(L_h^{\text{transfer}}|C\bar{C})$ site per site and save all partial contractions. Then, from bottom to top, i.e. for every $n_y =$

$1, \dots, 2L_y - 2$, we perform the following three steps, where we compactly denote "new" as "1" and "transfer" as "2", and omit the index n_y for the tensors $L_h^{1[n_y]}$, $L_h^{2[n_y]}$ and $C\bar{C}^{[n_y]}$:

- 1) Cut the two legs connecting L_h^1 and L_h^2 with $C\bar{C}$. Perform a "stacked QR decomposition" to split off a common down isometric Q . More precisely, stack the columns of L_h^1 and L_h^2 into a single matrix $(L_h^1 L_h^2)$, perform an ordinary QR decomposition $(L_h^1 L_h^2) = QR$, and split the triangular matrix $R = (R_1 R_2)$ such that $QR_1 = L_h^1$ and $QR_2 = L_h^2$. Diagrammatically:

$$\text{stacked QR} \quad L_h^1 \xrightarrow{\text{C}\bar{C}} R_1 \quad L_h^2 \xrightarrow{\text{C}\bar{C}} R_2 \quad (6.40)$$

- 2) Absorb the triangular matrices R_1 and R_2 into the partial expectation values $L_h^1 C$ and $L_h^2 C$, which then have same dimensions and can be summed up to $L_h C$. Decompose $L_h C = USV$ with SVD and truncate to $\chi_{\max,b}$ (if the dimension of S exceeds $\chi_{\max,b}$). Between U and S , insert an identity $U_{[:,\chi_{\max,b},:]}^\dagger U_{[:,\chi_{\max,b},:]} = \mathbb{1}_{\chi_{\max,b}}$:

$$L_h^1 C + L_h^2 C = L_h C \xrightarrow{\text{tSVD}} S = U \xrightarrow{\text{C}\bar{C}} V \quad (6.41)$$

- 3) Insert back $U_{[:,\chi_{\max,b},:]} S_{[:,\chi_{\max,b},:\chi_{\max,b}]} V_{[:,\chi_{\max,b},:]}$ $\approx L_h C = L_h^1 C + L_h^2 C$. Contraction of Q and $U_{[:,\chi_{\max,b},:]}$ gives the common bMPS tensor L_h . Absorb $U_{[:,\chi_{\max,b},:]}^\dagger R_1$ and $U_{[:,\chi_{\max,b},:]}^\dagger R_2$ into L_h^1 and L_h^2 of the next site $n_y + 1$:

$$L_h C = \tilde{L}_h^1 R_1 + \tilde{L}_h^2 R_2 \quad (6.42)$$

On the last site $n_y = 2L_y - 1$, R_1 and R_2 are vectors and their sum contains the global norm $\|L_h\|$. The corresponding unit vector plays the role of U :

$$R_1 + R_2 = L_h \quad (6.43)$$

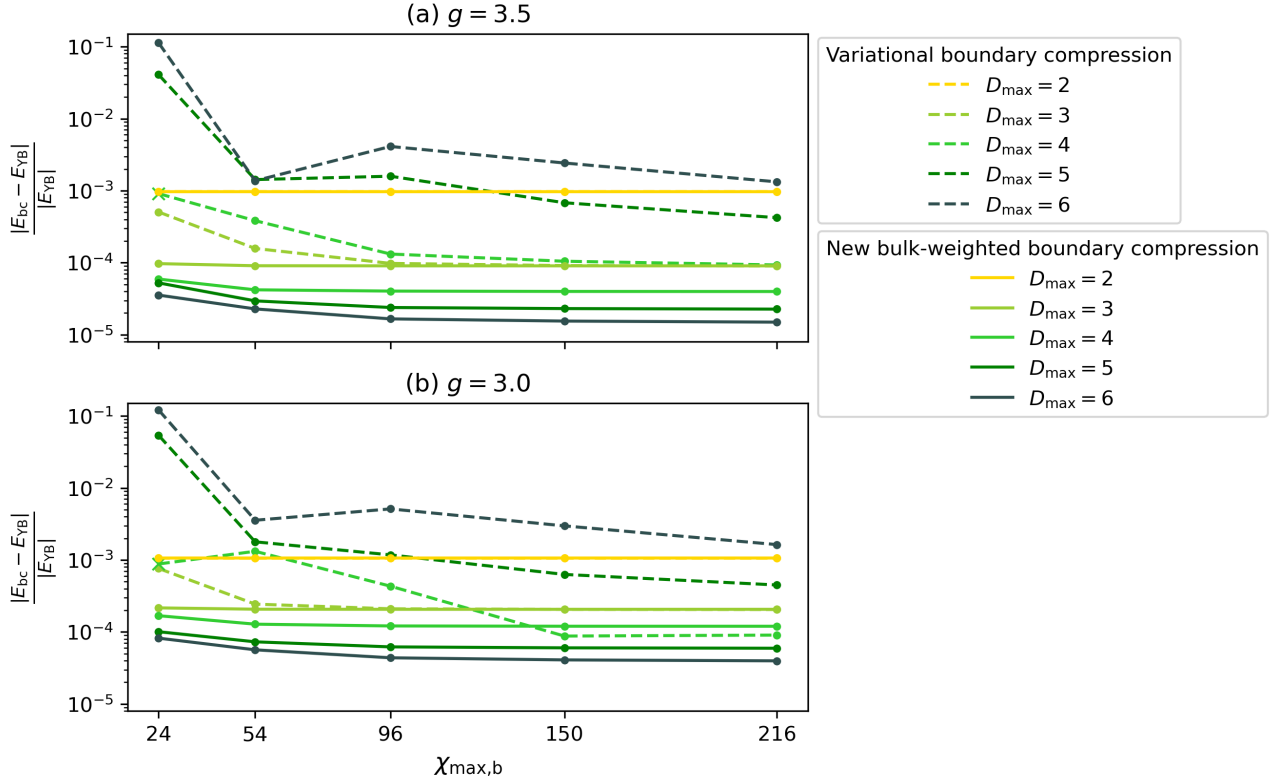


Figure 6.1: Benchmark for the bulk-weighted boundary compression (6.37) in comparison to the standard variational compression (6.35). For the orthogonality column on the right side of the isoPEPS, we compress all left bMPS (6.29) and compute the expectation value E_{bc} according to (6.28). For converged bMPS, we expect E_{bc} to equal E_{YB} (6.27) up to the error collected by the latter from sweeping through the state with Yang-Baxter moves. For isoPEPS with $L_x = L_y = 6$ and bond dimensions $D_{\max} = 2, 3, 4, 5, 6$, we plot the relative energy differences against increasing boundary bond dimensions $\chi_{\max,b} = 6D_{\max}^2$. A bullet \bullet indicates that $E_{bc} - E_{YB} > 0$, while a cross \times indicates that $E_{bc} - E_{YB} < 0$ (appears only twice for $D_{\max} = 4, \chi_{\max,b} = 24$). The new bulk-weighted compression converges much faster than the variational one. For the former, the converged energy differences get smaller with growing D_{\max} (as the YB errors do). For the latter, increasing $D_{\max} > 4$ even worsens the energies, as all states in the growing variational space are weighted equally. We work with approximate ground states—obtained from imaginary time TEBD²—in the paramagnetic phase of the TFI model. At (a) $g = 3.5$ (closer to a product state) slightly smaller energy differences are reached than at (b) $g = 3.0$ (closer to the critical point).

The stacked QR decomposition (6.40) has the highest asymptotic runtime complexity of

$$\mathcal{O}(D_{\max}^6 \chi_{\max,b}^3). \quad (6.44)$$

Benchmark

We now compare the performances of the two presented boundary compression methods. We apply them to approximate ground states obtained from a second order imaginary time TEBD² algorithm. The core idea is to implement the ground state projector $\lim_{t \rightarrow \infty} e^{-tH}$ in terms of local two-site gates. For this, we split time into N small steps δt and apply successive Suzuki-Trotter decompositions to the sum of column MPOs $H = \sum_{n_x} h^{[n_x, n_x+1]}$ (6.23):

$$|\psi_0\rangle \propto \lim_{N \rightarrow \infty} (e^{-\delta t H})^N |\psi_{\text{init}}\rangle, \quad (6.45)$$

$$e^{-\delta t H} \underset{\text{Suzuki-Trotter}}{=} \left(\prod_{n_x=1}^{2L_x-1} e^{-\frac{\delta t}{2} h^{[n_x, n_x+1]}} \right) \left(\prod_{n_x=2L_x-1}^1 e^{-\frac{\delta t}{2} h^{[n_x, n_x+1]}} \right) + \mathcal{O}(\delta t^3). \quad (6.46)$$

For each column evolution $e^{-\frac{\delta t}{2} h^{[n_x, n_x+1]}}$, we can then apply the well-established 1D TEBD scheme [Vid04]. It splits h into $h_{\text{odd}} + h_{\text{even}}$, where $h_{\text{odd}}/h_{\text{even}}$ is the sum of mutually commuting two-site gates acting on odd/even bonds. Another second order trotterization gives

$$e^{-\frac{\delta t}{2} h} \underset{\text{Suzuki-Trotter}}{=} e^{-\frac{\delta t}{4} h_{\text{odd}}} e^{-\frac{\delta t}{2} h_{\text{even}}} e^{-\frac{\delta t}{4} h_{\text{odd}}} + \mathcal{O}(\delta t^3). \quad (6.47)$$

For further details we refer to [Sap24], whose implementation we apply for $\delta t = 0.05$ and $N = 100$.

For converged boundaries L_h and R_h , we expect E_{bc} (6.28) and E_{YB} (6.27) to be equal up to the energy error collected by the Yang-Baxter moves in E_{YB} . In figure 6.1, we plot the relative energy difference $|E_{\text{bc}} - E_{\text{YB}}|/|E_{\text{YB}}|$ against $\chi_{\max,b}$ for $D_{\max} = 2, 3, 4, 5, 6$. We conclude:

- The Yang-Baxter error gets smaller for larger bond dimension D_{\max} and we expect the converged energy difference between E_{YB} and E_{bc} to behave the same way. For the new bulk-weighted boundary compression (6.37), this can be observed for all considered values of D_{\max} . Convergence is reached quickly for increasing bMPS bond dimension $\chi_{\max,b}$.
- In contrast, the standard variational boundary compression (6.35) does not converge within the covered range of $\chi_{\max,b}$ for $D_{\max} > 4$. The energies even get worse from $D_{\max} = 4$ to 5 and from 5 to 6. This can be intuitively understood as follows: Each "physical" bMPS leg has dimension up to D_{\max}^2 , so the variational space in which we do the optimization grows as $D_{\max}^{2(2L_y-1)}$. Since all states in the space are weighted equally by the variational compression, capturing a smaller fraction for larger D_{\max} leads to worse results. This was the main motivation for introducing the bulk-weighted compression scheme.

For completeness we note: when the boundaries (6.29) are not compressed additively, but each column MPO term is compressed and transferred separately, the changes in figure 6.1 are minor.

6.3 Density matrix renormalization group squared (DMRG²)

To optimize the isoPEPS (6.12) for the ground state of a Hamiltonian (6.23), we perform an algorithm that can be broken down into a high level sweep of column updates in x-direction, which unfold to a two-site DMRG in y-direction. Referring to this quadratic structure, it is called *density matrix renormalization group squared* (DMRG²) algorithm [LZP22]:

1) Zero-column DMRG in x -direction

Optimize the orthogonality column (which does not have any physical legs), while keeping all left and right isometric columns fixed. One update at center n_x corresponds to finding the ground state column $\tilde{C}^{[n_x]}$ of the effective Hamiltonian $H_{\text{eff},0}^{[n_x]}$ (with DMRG in y-

direction as described in point 2 below):

The diagram illustrates the decomposition of the effective Hamiltonian $H_{\text{eff},0}$ into three components: L_h , h , and R_h . The total system is represented by a green rectangle labeled $H_{\text{eff},0}$. It is decomposed into a left part L_h (green rectangle), a central part h (green rectangle), and a right part R_h (green rectangle). The central part h is further decomposed into \bar{A}_L , C , and \bar{A}_R tensors. Below the decomposition, it is indicated that this leads to the ground state. At the bottom, two equivalent representations of the state are shown: $\tilde{C}^{[n_x-1]} \tilde{A}_R^{[n_x]} A_R^{[n_x+1]}$ and $A_L^{[n_x]} \tilde{C}^{[n_x]} A_R^{[n_x+1]}$, both approximated by \approx YB and \approx YB.

$$(6.48)$$

Move the updated orthogonality column right/left to $n_x + 1/n_x - 1$ with YB move. This indirectly also updates the involved isometric column to $\tilde{A}_L^{[n_x+1]}/\tilde{A}_R^{[n_x]}$. Compress the new bMPS $\tilde{L}_h^{[n_x+1]}/\tilde{R}_h^{[n_x]}$. The bulk-weighted boundary compression (6.37) seems to be sensitive also to propagated changes of C and we find that going from local to global boundary updates stabilizes the algorithm vastly. With the described steps, repeatedly sweep $n_x = 0, \dots, 2L_x$ left to right and back, until isoPEPS and energy converge.

2) Two-site DMRG in y -direction

Perform the well-established 1D two-site DMRG as presented in section 5.2, but for the cMPS instead of a physical MPS. For an update of center n_y , start an iterative Lanczos algorithm with initial guess $\theta_2^{[n_y, n_y+1]}$ to find the ground state $\tilde{\theta}_2^{[n_y, n_y+1]}$ of the effective Hamiltonian. The action of the latter results from leaving out $\bar{\theta}_2^{[n_y, n_y+1]}$ in E_{bc} (6.28):

The diagram illustrates the decomposition of the effective Hamiltonian $H_{\text{eff},2}$ into components U , S , and V . The total system is represented by a green rectangle labeled $H_{\text{eff},2}$. It is decomposed into a left part U (green rectangle), a central part S (green rectangle), and a right part V (green rectangle). The central part S is further decomposed into $\tilde{U}^{[n_y]} \tilde{S}^{[n_y]} \tilde{V}^{[n_y+1]}$. Below the decomposition, it is indicated that this leads to the ground state. At the bottom, two equivalent representations of the state are shown: $\tilde{U}^{[n_y]} \tilde{S}^{[n_y]} \tilde{V}^{[n_y+1]}$ and $\tilde{S}^{[n_y]} \tilde{V}^{[n_y+1]} V^{[n_y+2]}/U^{[n_y-1]} \tilde{U}^{[n_y]} \tilde{S}^{[n_y]}$, both approximated by \approx tSVD and \approx $x_{\max,b}$.

$$(6.49)$$

The truncated SVD $\tilde{\theta}_2^{[n_y, n_y+1]} \approx \tilde{U}^{[n_y]} \tilde{S}^{[n_y]} \tilde{V}^{[n_y+1]}$ allows to move one site up/down and perform the next ground state search with guess $\tilde{S}^{[n_y]} \tilde{V}^{[n_y+1]} V^{[n_y+2]}/U^{[n_y-1]} \tilde{U}^{[n_y]} \tilde{S}^{[n_y]}$. Sweep up and down along $n_y = 1, \dots, 2L_y - 2$ until the center tensors do not change significantly anymore.

The multiplications with the effective boundary Hamiltonians have the maximum runtime complexity of

$$\mathcal{O}(D_{\max}^5 \chi_{\max,c}^3 \chi_{\max,b}). \quad (6.50)$$

Benchmark

In figures 6.2–6.6 we run DMRG² in the paramagnetic phase of the TFI model, for $N = 72$ spins on a diagonal square lattice with $L_x = L_y = 6$. Relative to an MPS reference, we track the energy error before (●) and after (×) every column update (6.48). For the final state, we additionally compute the expectation value E_{YB} (—). We can draw the following conclusions:

- What we found for the energy expectation value (6.28) in the previous section (figure 6.1) also holds for its minimization with effective Hamiltonians (6.49): For $D_{\max} \geq 4$, the newly developed bulk-weighted boundary compression (6.37) leads to significantly smaller errors than the variational compression (6.35). The latter even gets worse from $D_{\max} = 4$ to 5 and from 5 to 6. We recall our understanding: the dimension of the variational space in which the optimization is performed grows as $D_{\max}^{2(2L_y-1)}$, while the maximal allowed bMPS bond dimension is $\chi_{\max,b} = 6D_{\max}^2$. Because the variational compression weights all states in the space equally, capturing a shrinking fraction with growing D_{\max} yields worse results. This highlights the necessity of the improved bulk-weighted boundary compression method.
- The variational power of the isoPEPS is largest when the orthogonality column is located at the center of the lattice, from where the energies increase towards the edges. This can be explained by the enlarged bond dimension $\chi_{\max,c} = 6D_{\max}$ on the orthogonality column, which adds the most degrees of freedom to the isometric tensors when positioned in their middle. This effect is smoothed out when reducing $\chi_{\max,c}$, as demonstrated in figure 6.4 for $\chi_{\max,c} = 3D_{\max}$. The final expectation value E_{YB} , which is obtained by moving the orthogonality column through the entire state, is almost not affected by the reduction of $\chi_{\max,c}$.

The further discussion refers to DMRG² with the bulk-weighted boundary compression.

- Deep in the paramagnetic phase ($g = 3.5$), increasing the isoPEPS bond dimension beyond $D_{\max} = 4$ does not further lower the energies. This changes, at least for $D_{\max} = 5$, when moving closer to the critical point: at $g = 3.0$, the finite system is still in the paramagnetic phase but already shows increased ground state entanglement.
- For figures 6.2–6.5 we choose a bMPS bond dimension $\chi_{\max,b} = 6D_{\max}^2$. The fast convergence of the expectation value in figure 6.1 suggests that a smaller bond dimension already yields comparably good results. In figure 6.6 we halve the value to $\chi_{\max,b} = 3D_{\max}^2$. For $D_{\max} = 2, 3, 4$, the differences relative to figure 6.5 are indeed minor. For $D_{\max} = 5$, the final expectation value gets slightly worse. Note that smaller errors observed for some energies after column DMRG (×) can be misleading. In fact, the errors have negative sign, indicating an inaccurate compression of the effective Hamiltonian, as the true ground state has the lowest energy in the full Hilbert space.

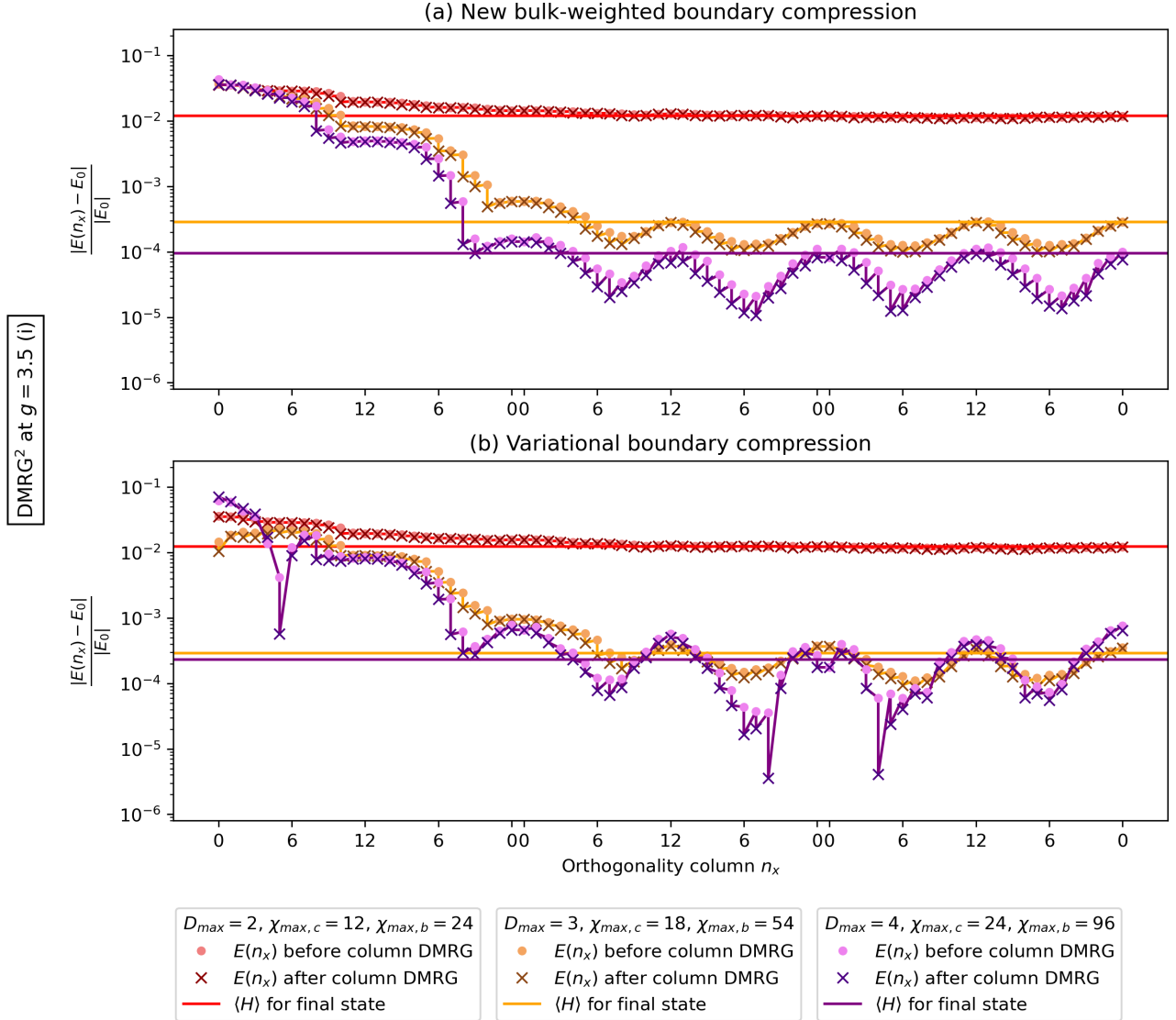


Figure 6.2: TFI Benchmark for DMRG² with (a) the new bulk-weighted boundary compression and (b) variational boundary compression. We optimize an isoPEPS on a diagonal square lattice with $L_x = L_y = 6$ for the ground state of the TFI model at $g = 3.5$. Relative to an MPS reference (E_0), we plot the energy error before (●) and after (✖) every column update (6.48), and the final error for the expectation value $\langle H \rangle = E_{\text{YB}}$ (—). While for $D_{\max} = 2, 3$ both boundary compression methods reach the same energies, the new bulk-weighted compression outperforms the variational one for $D_{\max} = 4$. As can be seen in figure 6.3, $D_{\max} = 5, 6$ do not lower the energies further. We choose $\chi_{\max,b} = 6D_{\max}^2$ and a relatively high orthogonality column bond dimension $\chi_{\max,c} = 6D_{\max}$. The latter enlarges the variational power when the orthogonality column is located at the center of the lattice, from where the energies increase towards the edges. Reducing $\chi_{\max,c}$ smooths out these differences, as can be observed in figure 6.4 for $\chi_{\max,c} = 3D_{\max}$.

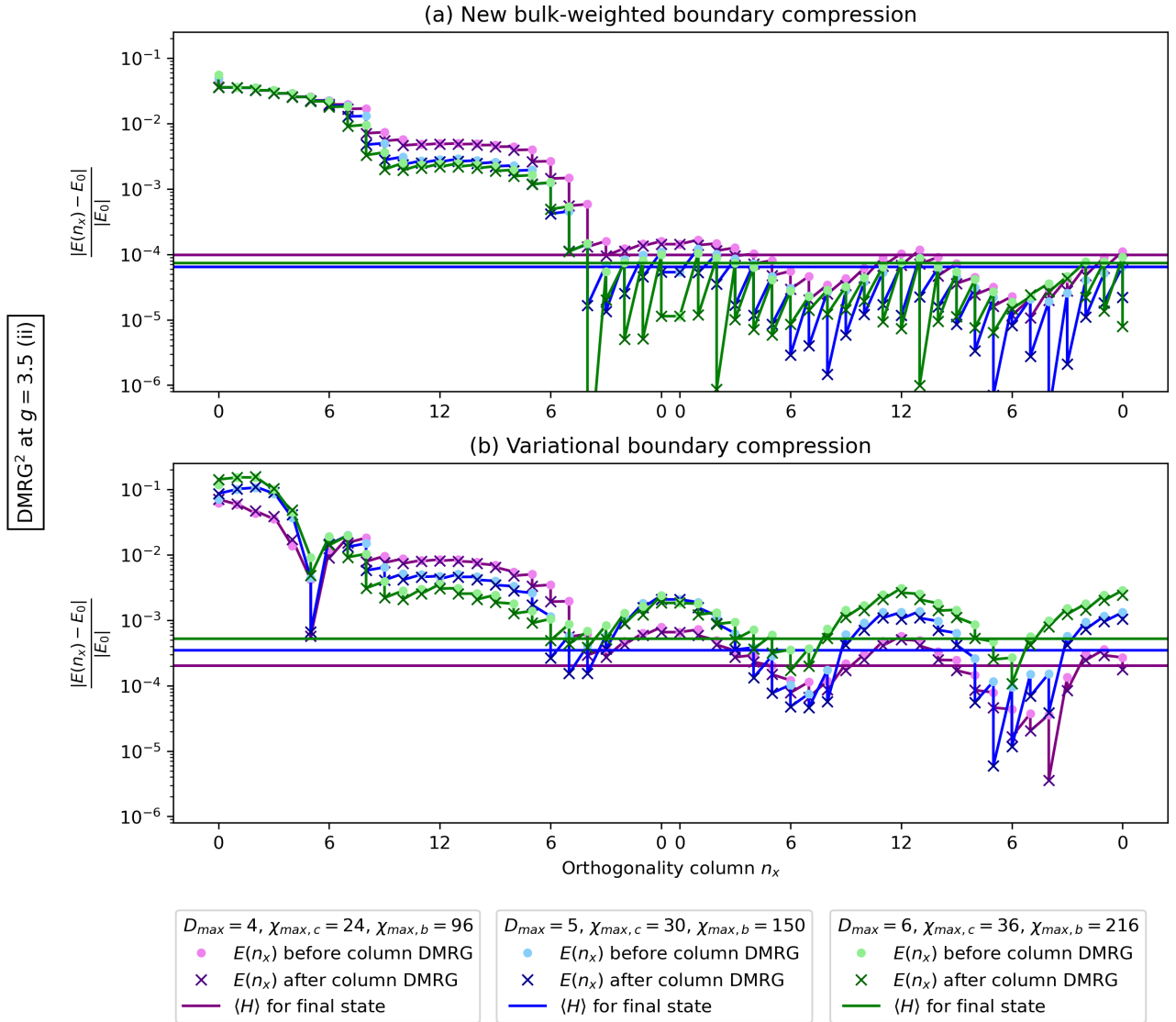


Figure 6.3: Continuation of figure 6.2 for $D_{\max} = 5, 6$. The data for $D_{\max} = 4$ is plotted again for reference. For (a) the new bulk-weighted boundary compression, the final energy errors remain close to the value obtained for $D_{\max} = 4$. For (b) variational compression, the bMPS with bond dimensions $\chi_{\max,b} = 6D_{\max}^2$ capture the effective Hamiltonian worse and worse for $D_{\max} > 4$.

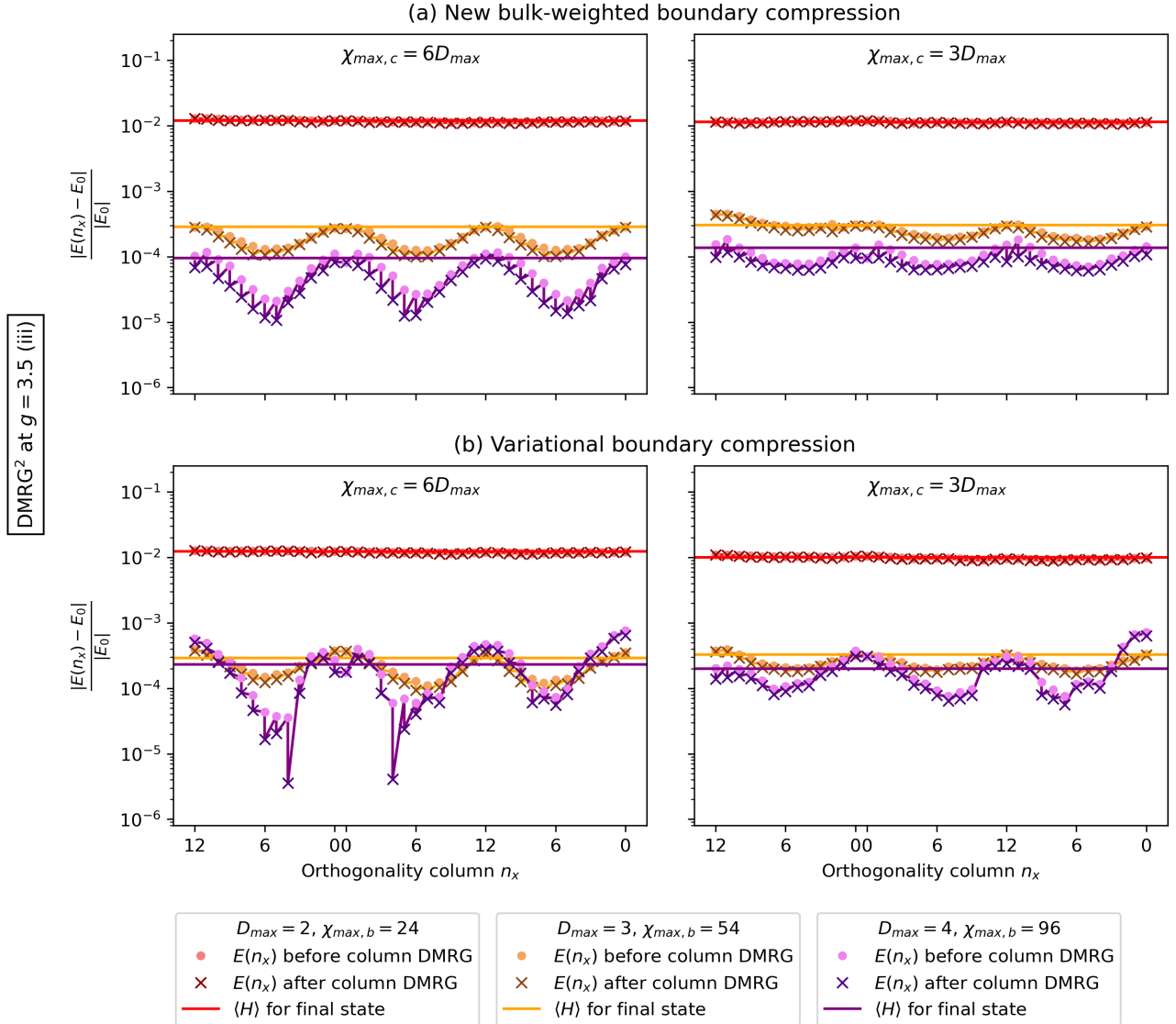


Figure 6.4: DMRG² with reduced bond dimension on the orthogonality column. We halve the value from $\chi_{max,c} = 6D_{max}$ in figure 6.2 to $\chi_{max,c} = 3D_{max}$ and compare the second half of the three column sweeps. As expected, the reduction smooths out the differences in variational power between the orthogonality column positioned at the center vs. at the edges.

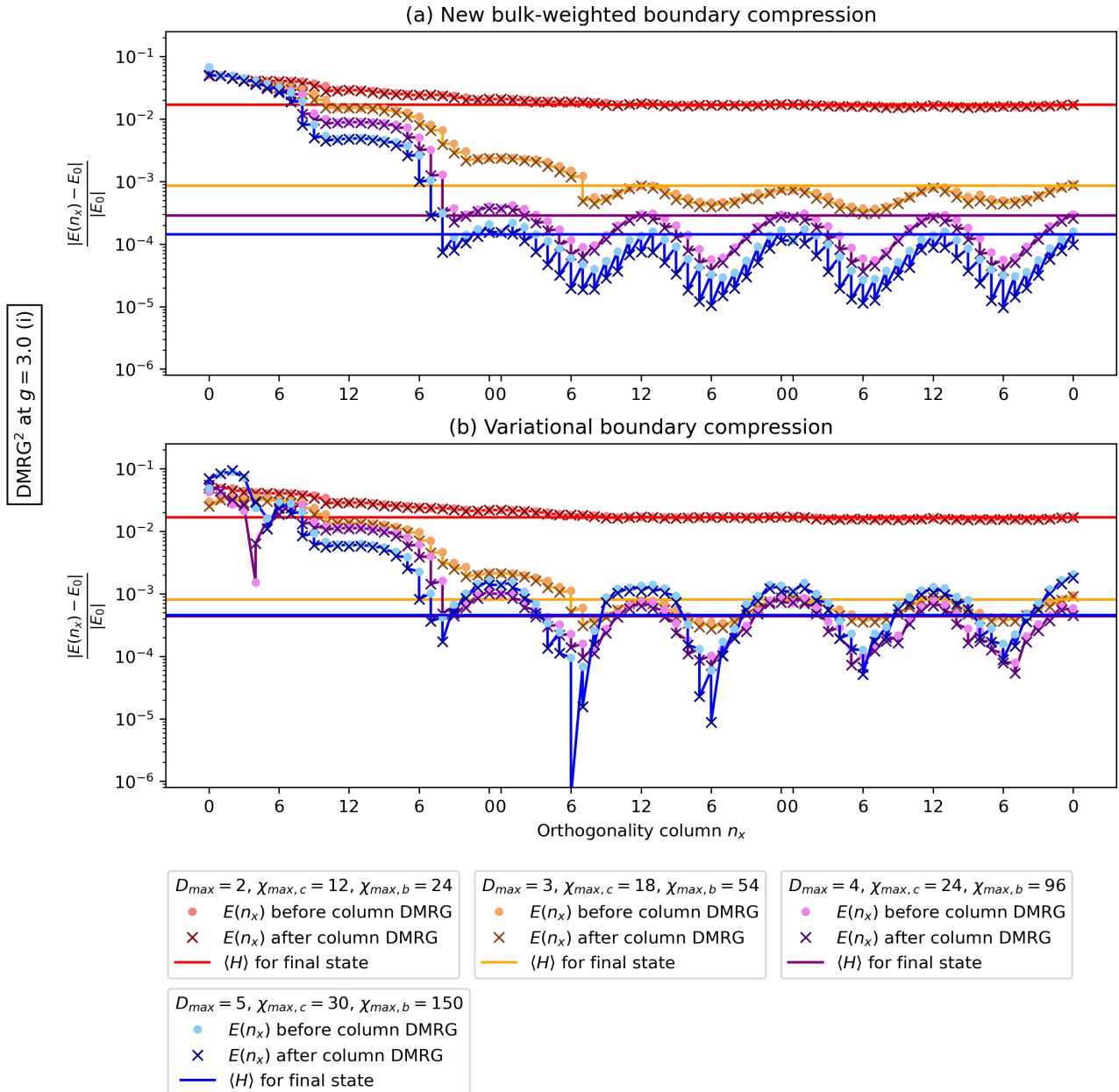


Figure 6.5: DMRG² closer to the critical point. We move from $g = 3.5$ in figure 6.2 to $g = 3.0$ in this figure. The critical point in the thermodynamic limit is $g_c \approx 3.044$, but for the chosen diagonal square lattice with OBC remains in the paramagnetic phase. Nevertheless, the increased ground state entanglement allows $D_{\max} = 5$ to further lower the energy compared to $D_{\max} = 4$, at least when using (a) the new bulk-weighted boundary compression. For (b) the standard variational boundary compression, the final expectation value errors for $D_{\max} = 4$ and 5 are on the same level and higher than the ones for (a).

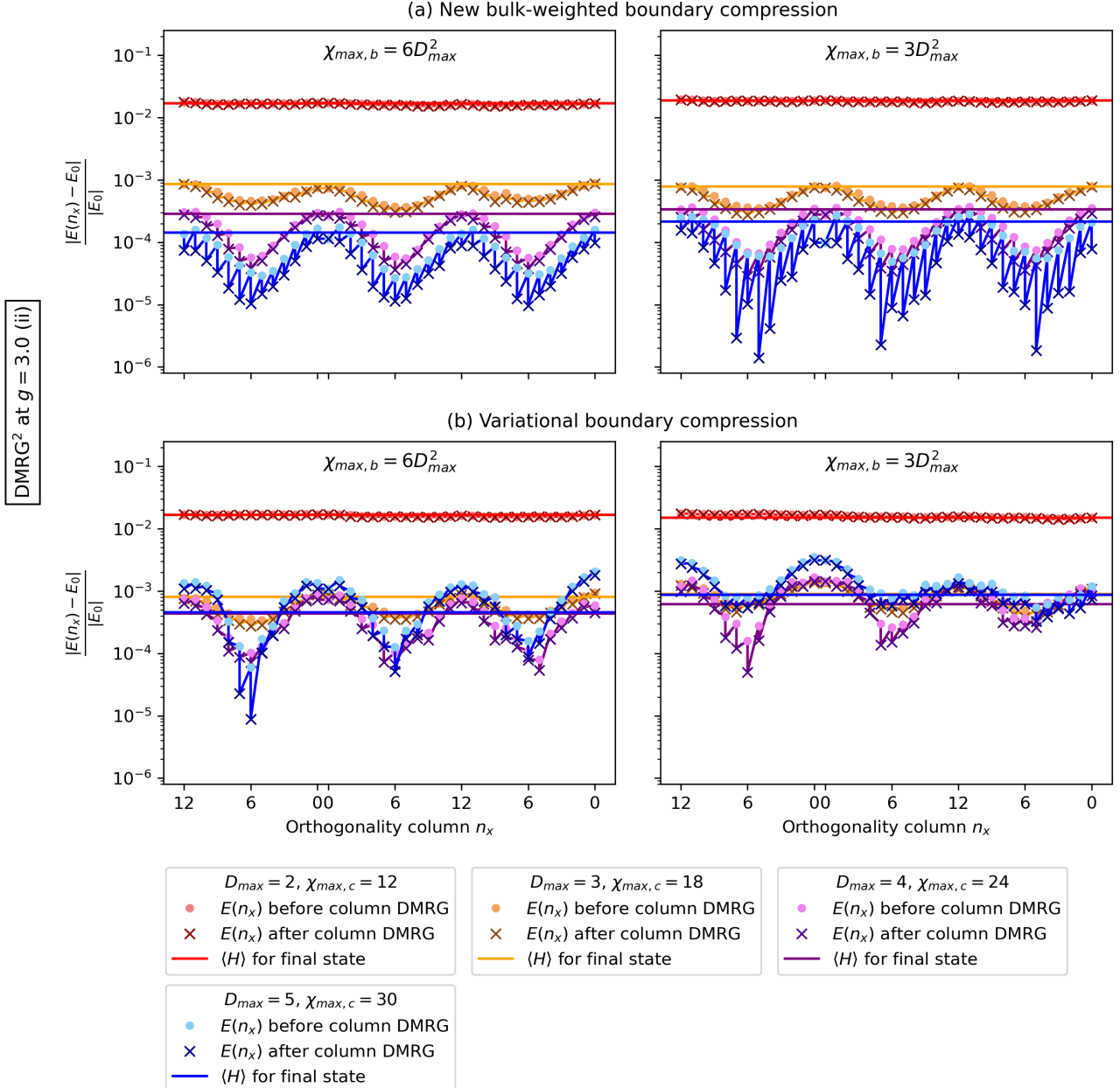


Figure 6.6: DMRG² with reduced bMPS bond dimension. We halve the value from $\chi_{\max,b} = 6D_{\max}^2$ in figure 6.5 to $3D_{\max}^2$ and compare the second half of the three column sweeps. While for $D_{\max} = 2, 3, 4$ the differences are minor, the final expectation value $\langle H \rangle$ (—) is slightly worse for $D_{\max} = 5$. In (a), the smaller errors for some effective ground state energies (\times) can be misleading. In fact, the errors have negative sign, indicating an inaccurate compression of the effective Hamiltonian, as the true ground state has the lowest energy (E_0) in the full Hilbert space.

6.4 Variational quasiparticle excitations

In a similar fashion as for MPS in section 5.3, we want to create quasiparticle excitations against the correlated isoPEPS ground state vacuum. Again (but as we will see, less strictly), a tangent space vector serves as orientation. It results from small deviations from the isoPEPS that has, by our convention, the orthogonality column on the very right:

$$|\psi(A_L, C)\rangle = \begin{array}{c} \text{Diagram of a 2D PEPS lattice with black circles at vertices and blue circles at vertical edges, representing the state } |\psi(A_L, C)\rangle. \\ A_L^{[1]} \quad A_L^{[2]} \quad A_L^{[3]} \quad A_L^{[4]} \quad A_L^{[5]} \quad A_L^{[6]} \quad C^{[6]} \end{array} . \quad (6.51)$$

In contrast to the MPS (5.12) with $C^{[N]} = ((1)) \in \mathbb{C}^{1 \times 1}$, the orthogonality column $C^{[2L_x]} \in \mathbb{C}^{D_{\max}^{2L_y-1} \times 1}$ in (6.51) is nontrivial. As a consequence, we additionally have to take into account the derivative with respect to each of its components when building the tangent space vector:

$$\begin{aligned} & |\psi(B, D; A_L, C)\rangle \\ &= \sum_{n_x, y} \sum_{s, \alpha, \beta, \gamma, \delta} B_{\alpha \beta \gamma \delta}^{[n_x, y] s} \left[\partial_{(A_L^{[n_x, y]})^s_{\alpha \beta \gamma \delta}} |\psi(A_L, C)\rangle \right] + \sum_{n_y} \sum_{d, l, r, u} D_{dlru}^{[n_y]} \left[\partial_{C_{dlru}^{[2L_x, n_y]}} |\psi(A_L, C)\rangle \right] \\ &= \sum_{n_x, y} \begin{array}{c} \text{Diagram of a 2D PEPS lattice with black circles at vertices and blue circles at vertical edges, with a purple circle labeled } B^{[n_x, y]} \text{ at the } (x, y) \text{ site.} \end{array} + \sum_{n_y} \begin{array}{c} \text{Diagram of a 2D PEPS lattice with black circles at vertices and blue circles at vertical edges, with a purple circle labeled } D^{[n_y]} \text{ at the } (2L_x, y) \text{ site.} \end{array} . \end{aligned} \quad (6.52)$$

Parametrization of the ansatz

We now parametrize the tangent space vector (6.52)—for a given ground state equivalently the perturbation tensors B, D —by a joint collection of tensors X , such that the individual states in the superposition

$$|\psi(X; A_L, C)\rangle = \sum_{n_x, y} |\psi(X^{[n_x, y]}; A_L, C)\rangle + \sum_{n_y} |\psi(X^{[n_y]}; A_L, C)\rangle \quad (6.53)$$

fulfill the following orthogonality conditions:

- 1) Ground state $\langle \psi(\bar{A}_L, \bar{C}) | \psi(X^{[n_x, y]}; A_L, C) \rangle = \langle \psi(\bar{A}_L, \bar{C}) | \psi(X^{[n_y]}; A_L, C) \rangle = 0$.
- 2) Pairwise
 - a) $\langle \psi(\bar{X}^{[n_x, y]}; \bar{A}_L, \bar{C}) | \psi(X^{[n_y]}; A_L, C) \rangle = 0$,
 - b) $\langle \psi(\bar{X}^{[\tilde{n}_x, \tilde{y}]}; \bar{A}_L, \bar{C}) | \psi(X^{[n_x, y]}; A_L, C) \rangle = \delta_{n_x, \tilde{n}_x} \delta_{y, \tilde{y}} (\bar{X}^{[n_x, y]} | X^{[n_x, y]})$,
 - c) $\langle \psi(\bar{X}^{[\tilde{n}_y]}; \bar{A}_L, \bar{C}) | \psi(X^{[n_y]}; A_L, C) \rangle = \delta_{n_y, \tilde{n}_y} (\bar{X}^{[n_y]} | X^{[n_y]})$.

Property 1) enforces the physical requirement that the quasiparticle ansatz must be orthogonal to the ground state vacuum in order to describe a genuine excitation eigenstate. Property 2) makes the norm matrix equal the identity, which simplifies the variational eigenvalue problem and improves numerical stability. For MPS, it is a nice feature that these properties can be ensured exactly within the gauge freedom. This is not the case for isoPEPS. Fixing the gauge in general only removes null-vectors, which makes the effective norm matrix positive definite (invertible). For (6.52), A_L -perturbations of the form

$$B_0 = A_L(X_d \otimes \mathbb{1}_u) + A_L(\mathbb{1}_d \otimes X_u) \quad \text{with } X_d \in \mathbb{C}^{D_{rd} \times D_{rd}}, X_u \in \mathbb{C}^{D_{ru} \times D_{ru}} \quad (6.55)$$

can be subtracted on the next column. Since $(X_d, X_u) = (\alpha \mathbb{1}_d, \beta \mathbb{1}_u)$ and $(\beta \mathbb{1}_d, \alpha \mathbb{1}_u)$ give the same B_0 , we effectively have $D_{rd}^2 + D_{ru}^2 - 1$ gauge parameters per tensor¹. However, to meet the desired properties (6.54) (to be precise, for now only 1, 2a and orthogonality of 2b), we have to project out deviation tensors of the form

$$B_0^+ = A_L X_{du} \quad \text{with } X_{du} \in \mathbb{C}^{D_{rd} D_{ru} \times D_{rd} D_{ru}} \quad (6.56)$$

This fixes $D_{rd}^2 D_{ru}$ parameters and is as restrictive as (6.55) if $D_{rd} = 1$ or $D_{ru} = 1$, and more restrictive than (6.55) if $D_{rd}, D_{ru} \geq 2$. In principle, we would like to span the whole tangent space and stick to gauging out (6.55), but for the excitation ansatz the practical benefits of (6.54) prevail. To remove (6.56), we set $B^{[n_x, y]} = 0$ if $D_{ld} D_{lu} d = D_{rd} D_{ru}$ and

$$\text{if } D_{ld} D_{lu} d - D_{rd} D_{ru} > 0 : B^{[n_x, y]} = V_L^{[n_x, y]} X^{[n_x, y]} \quad \text{with} \quad \overline{A}_L^{[n_x, y]} = 0. \quad (6.57)$$

To make sure that the missing part of 2b), $\langle \psi(\overline{X}^{[n_x, y]}) | \psi(X^{[n_x, y]}) \rangle = (\overline{X}^{[n_x, y]} | X^{[n_x, y]})$, holds, we (approximately) move the orthogonality column right next to $X^{[n_x, y]}$ with YB moves, and absorb the two adjacent $C^{[n_x]}$ -tensors (that together are normalized) therein. Compared to (6.57) this enlarges the variational space:

$$\text{if } D_{ld} D_{lu} d - D_{rd} D_{ru} > 0 : B^{[n_x, y]} = V_L^{[n_x, y]} X^{[n_x, y]} \quad \text{with} \quad \overline{A}_L^{[n_x, y]} = 0. \quad (6.58)$$

¹Due to the closed loops in the virtual legs, there may be further gauge transformations that are not as obvious to write down as (6.55).

It remains to fix the gauge for the excitations D on the orthogonality column $C^{[2Lx]}$, which we treat as a cMPS for this purpose. After having brought it into canonical form, the steps are completely analogous to the one we described for the MPS in equations (5.30)–(5.33), when we assign $C_D^{[n_y]}$ the role of $A_L^{[n]}$. Accordingly, we set $D^{[n_y]} = 0$ if $\chi_d D_l D_r = \chi_u$ and

$$\text{if } \chi_d D_l D_r - \chi_u > 0 : D^{[n_y]} = \begin{array}{c} \rightarrow \\ \leftarrow \end{array} \quad \text{with} \quad \overline{C}_D^{[n_y]} = 0. \quad (6.59)$$

This guarantees 2c) and the second equality of 1) in (6.54). In total, the parametrizations (6.58) and (6.59) ensure that the desired properties (6.54) are fulfilled by the corresponding excitation ansatz $|\psi(X; A_L, C)\rangle$. The latter has the diagrammatic representation

$$|\psi(X; A_L, C)\rangle = \sum_{n_x, y} \text{Diagram} + \sum_{n_y} \text{Diagram} . \quad (6.60)$$

We investigate the variational power of (6.60) to capture low-energy excitations in two steps:

- 1) Overlap optimization² with the exact wavefunction or an MPS,
- 2) Diagonalization of the effective Hamiltonian.

In the following we omit the explicit ground state reference (A_L, C) in $|\psi(X; A_L, C)\rangle$ and write isoPEPS instead of ψ when we want to clearly distinguish our ansatz from an exact wavefunction or MPS.

From wavefunction overlap

After having computed a full excitation wavefunction $|\psi\rangle$ with exact diagonalization (ED), the optimal local perturbation of the ground state isoPEPS at site $[n_x, y]$, in order to approximate $|\psi\rangle$, is given by

$$X_\psi^{[n_x, y]} = \partial_{\overline{X}^{[n_x, y]}} \langle \text{isoPEPS}(\overline{X}) | \psi \rangle = \text{Diagram} . \quad (6.61)$$

²There are two equivalent ways to define the optimization: (i) $\arg \min_X \| \text{isoPEPS}(X) - \psi \|^2$, where normalization is implicit in the cost function, or (ii) $\arg \max_X \langle \text{isoPEPS}(\overline{X}) | \psi \rangle$ subject to $\langle \text{isoPEPS}(\overline{X}) | \text{isoPEPS}(X) \rangle = 1$. In the latter case a Lagrange multiplier enforces normalization, and both formulations lead to the stationarity condition $X = \partial_{\overline{X}} \langle \text{isoPEPS}(\overline{X}) | \psi \rangle$.

Excitations on the orthogonality column are obtained analogously, by leaving the legs of $\overline{X}^{[n_y]}$ open. The achieved overlap does not need to be computed separately, but is equal to the squared norm of the optimized parameters:

$$\begin{aligned}
 \langle \text{isoPEPS}(\overline{X}) | \psi \rangle &= \sum_{n_x, y} \langle \text{isoPEPS}(\overline{X}^{[n_x, y]}) | \psi \rangle + \sum_{n_y} \langle \text{isoPEPS}(\overline{X}^{[n_y]}) | \psi \rangle \\
 &= \sum_{n_x, y} (\overline{X}^{[n_x, y]} | \underbrace{\partial_{\overline{X}^{[n_x, y]}} \langle \text{isoPEPS}(\overline{X}) | \psi \rangle}_{=|X^{[n_x, y]}\rangle} + \sum_{n_y} (\overline{X}^{[n_y]} | \underbrace{\partial_{\overline{X}^{[n_y]}} \langle \text{isoPEPS}(\overline{X}) | \psi \rangle}_{=|X^{[n_y]}\rangle} \\
 &= \sum_{n_x, y} \|X^{[n_x, y]}\|^2 + \sum_{n_y} \|X^{[n_y]}\|^2 = \|X\|^2.
 \end{aligned} \tag{6.62}$$

This approach is restricted to small systems of $N \lesssim 20$ spin-1/2s and thus to $L_x, L_y \lesssim 3$ for the diagonal square lattice.

From MPS overlap

For larger systems, where ED is no longer feasible, we can instead wind an MPS through the square lattice and run DMRG + VQPE. The corresponding isoPEPS excitations to maximize the overlap are given by

$$X_{\text{MPS}}^{[n_x, y]} = \sum_{n=1}^{2L_x L_y} \partial_{\overline{X}^{[n_x, y]}} \langle \text{isoPEPS}(\overline{X}) | \text{MPS}(B^{[n]}) \rangle = \sum_{n=1}^{2L_x L_y} \text{Diagram} \tag{6.63}$$

For each term in the sum, we contract the isoPEPS tensors column per column with the MPS tensors, separately from left and from right until we reach the open legs. In this way, the intermediate boundary tensors carry $2L_y - 1$ open legs of maximal dimension D_{\max} . The required memory scales exponentially as $\mathcal{O}(D_{\max}^{2L_y-1})$, which is the key limitation of this procedure. The interaction range of the Hamiltonian is $L_y + 1$ for our choice of MPS winding. Accordingly, the required virtual bond dimension of the MPS, which appears as additional factor in the boundary dimension, increases with L_y . We go up to a parameter combination of $L_x = L_y = 5$, $D_{\max}^{\text{MPS}} = 256$ and $D_{\max} = 3$. Relation (6.62) again holds, providing the achieved overlap without extra computation.

From effective Hamiltonian

Finally, we optimize the excitation parameters X energetically by solving the eigenvalue problem $H_{\text{eff}}|X\rangle = \lambda|X\rangle$. We implement the matrix-vector multiplication $|\tilde{X}\rangle = H_{\text{eff}}|X\rangle$ by performing a conversion

$$X = \{X^{[n_x, y]}, X^{[n_y]}\}_{n_x, y, n_y} \rightarrow B = \{B^{[n_x, y]}\}_{n_x, y}, \tag{6.64}$$

computing

$$|\tilde{B})^{[n_x,y]} = \partial_{\overline{B}^{[n_x,y]}} \langle \psi(\overline{B}) | H | \psi(B) \rangle \quad (6.65)$$

and transforming back to $|\tilde{X}\rangle$ with the inverse of (6.64). Latter we can do locally thanks to the orthogonality conditions (6.54). For all $n_x = 1, \dots, 2L_x - 1$, we take the B -tensors as already defined in (6.58):

$$B^{[n_x,y]} = V_L^{[n_x,y]} X^{[n_x,y]} \quad (n_x = 1, \dots, 2L_x - 1). \quad (6.66)$$

On the last column $n_x = 2L_x$, we additionally include the excitations on the orthogonality column:

$$\begin{array}{c} \text{Diagram 1} \\ B^{[2L_x,y]} \end{array}
 =
 \begin{array}{c} \text{Diagram 2} \\ V_L^{[2L_x,y]} X^{[2L_x,y]} \end{array}
 +
 \begin{array}{c} \text{Diagram 3} \\ A_L^{[2L_x,y]} \frac{X^{[2y-1]}}{V_D^{[2y-1]}} \end{array}
 +
 \begin{array}{c} \text{Diagram 4} \\ A_L^{[2L_x,y]} \frac{X^{[2y]}}{V_D^{[2y]}} \end{array} . \quad (6.67)$$

Inversely, the two excitation types can be separated by contracting $B^{[2L_x,y]}$ with $\overline{V}_L^{[2L_x,y]} / \overline{A}_L^{[2L_x,y]}$, which projects out the $A_L^{[2L_x,y]} / V_L^{[2L_x,y]}$ terms. On the cMPS, the analogous orthonormality properties of the C_{Ds} and V_{Ds} can be used to extract $X^{[2y-1]}$ and $X^{[2y]}$.

Moreover, with the help of a finite state machine (FSM), we can capture the sum in y-direction with a single set of MPO-like tensors that have doubled vertical bond dimension:

$$\begin{aligned}
B^{[n_x]} &= \sum_{y=1}^{L_y} B^{[n_x, y]} = A_U^{[n_x, y+1]} - A_D^{[n_x, y-1]} \\
&\quad \downarrow \text{FSM} \\
&\chi_d \begin{pmatrix} \chi_u & \chi_u \\ A_D^{[n_x, 1]} & B^{[n_x, 1]} \end{pmatrix}, \quad \chi_d \begin{pmatrix} \chi_u & \chi_u \\ A_D^{[n_x, y]} & B^{[n_x, y]} \\ 0 & A_U^{[n_x, y]} \end{pmatrix}_{y=2, \dots, L_y-1}, \quad \chi_d \begin{pmatrix} \chi_u \\ B^{[n_x, L_y]} \\ A_U^{[n_x, L_y]} \end{pmatrix}.
\end{aligned} \tag{6.68}$$

With (6.68), the isoPEPS excitation ket (6.60) has the compact diagrammatic representation

$$|\psi(B)\rangle = \sum_{n_x=1}^{2L_x} |\psi(B^{[n_x]})\rangle = \text{Diagram 1} + \text{Diagram 2} + \dots + \text{Diagram 10}. \quad (6.69)$$

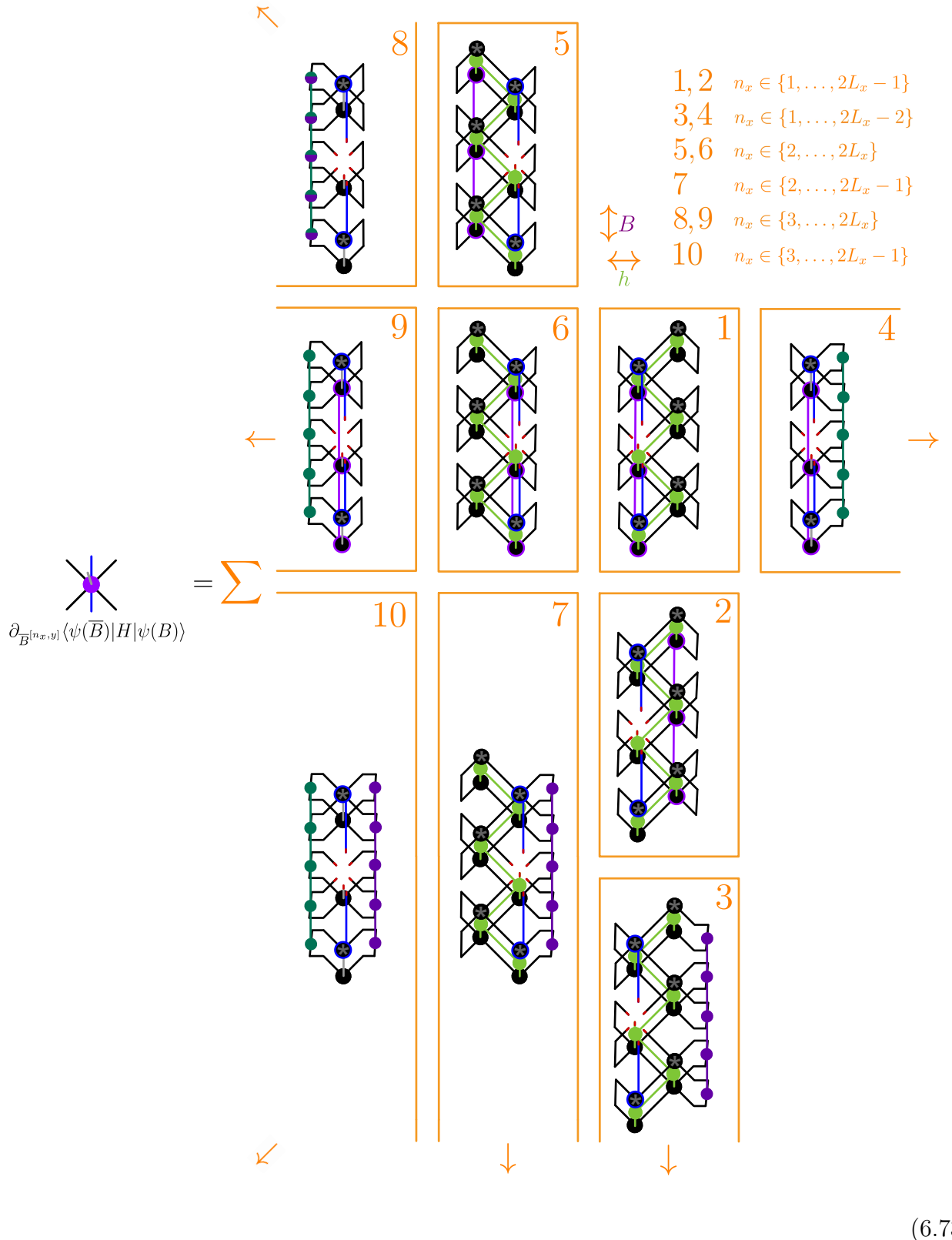
In accordance with this notation, we draw the bra derivative in (6.65) as

$$\partial_{\bar{B}^{[n_x,y]}} \langle \psi(\bar{B}) | = \text{Diagram 1} = \text{Diagram 2}. \quad (6.70)$$

Sandwiching the Hamiltonian (6.23) between (6.69) and (6.70), gives an action of the effective Hamiltonian as specified on the next page in equation (6.73). The terms that vanish due to the orthogonality properties implied by (6.58) and (6.59) are already omitted. The double sum over $H = \sum_{\tilde{n}_x} h^{[\tilde{n}_x, \tilde{n}_x+1]}$ and $|\psi(B)\rangle = \sum_{n'_x} |\psi(B^{[n'_x]})\rangle$ is covered by the rows and columns of the orange boxes. In the upper right corner we specify for which bra excitation columns n_x each of the 10 terms appears. Besides the bMPS (6.29) and (6.30), that only contain hs , we newly introduce right and left boundaries that only contain Bs and both hs and Bs , respectively:

$$\left| R_B^{[n_x]} \right\rangle = \left| \bar{A}_R^{[n_x]} \right\rangle + \left| \bar{A}_R^{[n_x]} \right\rangle \left| R_B^{[n_x+1]} \right\rangle; \quad (6.71)$$

$$\left(L_{Bh}^{[n_x]} \right) = \left(\begin{array}{c} \bar{A}_L^{[n_x-1]} \bar{A}_L^{[n_x]} \\ h^{[n_x-1, n_x]} \\ B^{[n_x-1]} A_R^{[n_x]} \end{array} \right) + \left(\begin{array}{c} \bar{A}_L^{[n_x-1]} \bar{A}_L^{[n_x]} \\ h^{[n_x-1, n_x]} \\ A_L^{[n_x-1]} B^{[n_x]} \end{array} \right) + \left(\begin{array}{c} L_h^{[n_x-1]} \bar{A}_L^{[n_x]} \\ B^{[n_x]} \end{array} \right) + \left(\begin{array}{c} L_{Bh}^{[n_x-1]} \bar{A}_L^{[n_x]} \\ A_R^{[n_x]} \end{array} \right) \Rightarrow \quad (6.72)$$



Local energies

For isoPEPS excitations optimized directly from an exact wavefunction or an MPS, the overlap (6.62) serves as success measure. When diagonalizing the effective Hamiltonian, the eigenenergy can be compared to the one obtained for MPS. In addition, for both the approaches, we aim to visualize the nearest-neighbor (NN) bond energies $\langle h_{n,m} \rangle$ with

$$h_{n,m} = -\frac{g}{2}(\sigma_n^z \otimes \mathbb{1}_m) - \frac{g}{2}(\mathbb{1}_n \otimes \sigma_m^z) - J(\sigma_n^x \otimes \sigma_m^x) \quad n, m \text{ NN.} \quad (6.74)$$

To compute them for the excited isoPEPS (6.69), we implement the expectation value of a general two-column MPO $h^{[n_x, n_x+1]}$ (which we fill up with identities around the respective two-site operator in practice). In x-direction the problem is equivalent to calculating the local MPS energies (5.45). The expansion in y-direction turns the boundary tensors (5.44) into bMPS $|R_B^{[n_x]} \rangle, |\overline{R}_{\overline{B}}^{[n_x]} \rangle, |R_{BB}^{[n_x]} \rangle, |L_{BB}^{[n_x]} \rangle$ and the additions into additive compressions:

$$\left| R_B^{[n_x]} \right\rangle \stackrel{(6.71)}{=} \left| \overline{A}_R^{[n_x]} \right\rangle + \left| \overline{A}_R^{[n_x]} \right\rangle \left| R_B^{[n_x+1]} \right\rangle ; \quad \left| R_{\overline{B}}^{[n_x]} \right\rangle = \left| \overline{B}^{[n_x]} \right\rangle + \left| \overline{B}^{[n_x]} \right\rangle \left| R_{\overline{B}}^{[n_x+1]} \right\rangle ;$$

$$(6.75)$$

$$\left| R_{BB}^{[n_x]} \right\rangle = \left| \overline{B}^{[n_x]} \right\rangle + \left| \overline{A}_L^{[n_x]} \right\rangle \left| R_{\overline{B}}^{[n_x+1]} \right\rangle + \left| \overline{B}^{[n_x]} \right\rangle \left| R_B^{[n_x+1]} \right\rangle + \left| \overline{A}_L^{[n_x]} \right\rangle \left| R_{BB}^{[n_x+1]} \right\rangle ;$$

$$(6.76)$$

$$\left(L_{BB}^{[n_x]} \right) = \left(\overline{B}^{[n_x]} \right) + \left(\overline{L}_{BB}^{[n_x-1]} \right) \left(\overline{A}_R^{[n_x]} \right) \Rightarrow$$

$$(6.77)$$

$$\begin{aligned}
\langle \psi(\overline{B}) | h^{[n_x, n_x+1]} | \psi(B) \rangle &= \left(\begin{array}{c|c} L_{B\overline{B}}^{[n_x-1]} & \overline{A}_R^{[n_x]} A_R^{[n_x+1]} \\ \hline & h^{[n_x, n_x+1]} \\ & A_R^{[n_x]} A_R^{[n_x+1]} \end{array} \right) \\
&+ \left(\begin{array}{c|c} \overline{B}^{[n_x]} \overline{A}_R^{[n_x+1]} & \overline{A}_L^{[n_x]} \overline{B}^{[n_x+1]} \\ \hline h^{[n_x, n_x+1]} & h^{[n_x, n_x+1]} \\ B^{[n_x]} A_R^{[n_x+1]} & B^{[n_x]} A_R^{[n_x+1]} \end{array} \right) \\
&+ \left(\begin{array}{c|c} \overline{A}_L^{[n_x]} \overline{B}^{[n_x+1]} & \overline{A}_L^{[n_x]} A_L^{[n_x+1]} \\ \hline h^{[n_x, n_x+1]} & h^{[n_x, n_x+1]} \\ B^{[n_x]} A_R^{[n_x+1]} & B^{[n_x]} A_R^{[n_x+1]} \end{array} \right) \\
&+ \left(\begin{array}{c|c} \overline{B}^{[n_x]} \overline{A}_R^{[n_x+1]} & \overline{A}_L^{[n_x]} \overline{B}^{[n_x+1]} \\ \hline h^{[n_x, n_x+1]} & h^{[n_x, n_x+1]} \\ A_L^{[n_x]} B^{[n_x+1]} & A_L^{[n_x]} B^{[n_x+1]} \end{array} \right) \\
&+ \left(\begin{array}{c|c} \overline{A}_L^{[n_x]} \overline{B}^{[n_x+1]} & \overline{A}_L^{[n_x]} A_L^{[n_x+1]} \\ \hline h^{[n_x, n_x+1]} & h^{[n_x, n_x+1]} \\ A_L^{[n_x]} B^{[n_x+1]} & A_L^{[n_x]} B^{[n_x+1]} \end{array} \right) \\
&+ \left(\begin{array}{c|c} \overline{B}^{[n_x]} \overline{A}_R^{[n_x+1]} & \overline{A}_L^{[n_x]} \overline{B}^{[n_x+1]} \\ \hline h^{[n_x, n_x+1]} & h^{[n_x, n_x+1]} \\ A_L^{[n_x]} A_L^{[n_x+1]} & R_B^{[n_x+2]} \end{array} \right) \\
&+ \left(\begin{array}{c|c} \overline{A}_L^{[n_x]} \overline{B}^{[n_x+1]} & \overline{A}_L^{[n_x]} \overline{B}^{[n_x+1]} \\ \hline h^{[n_x, n_x+1]} & h^{[n_x, n_x+1]} \\ A_L^{[n_x]} A_L^{[n_x+1]} & R_B^{[n_x+2]} \end{array} \right) \\
&+ \left(\begin{array}{c|c} \overline{B}^{[n_x]} \overline{A}_R^{[n_x+1]} & \overline{A}_L^{[n_x]} \overline{B}^{[n_x+1]} \\ \hline h^{[n_x, n_x+1]} & h^{[n_x, n_x+1]} \\ A_L^{[n_x]} A_L^{[n_x+1]} & R_{B\overline{B}}^{[n_x+2]} \end{array} \right) \quad . \\
&\qquad\qquad\qquad (6.78)
\end{aligned}$$

The diagram consists of a sum of eight terms, each represented by a grid of nodes connected by green and purple lines. The nodes are arranged in a 4x4 pattern. Green lines connect nodes in a checkerboard-like pattern, while purple lines connect nodes in a vertical column. The first term is a single grid with a purple line connecting the top-left node to the bottom-right node. Subsequent terms are added to it, each with a different set of connections. The terms involve various combinations of \overline{A} , A , B , and R operators, with indices n_x and n_x+1 . The final term includes a label (6.78) .

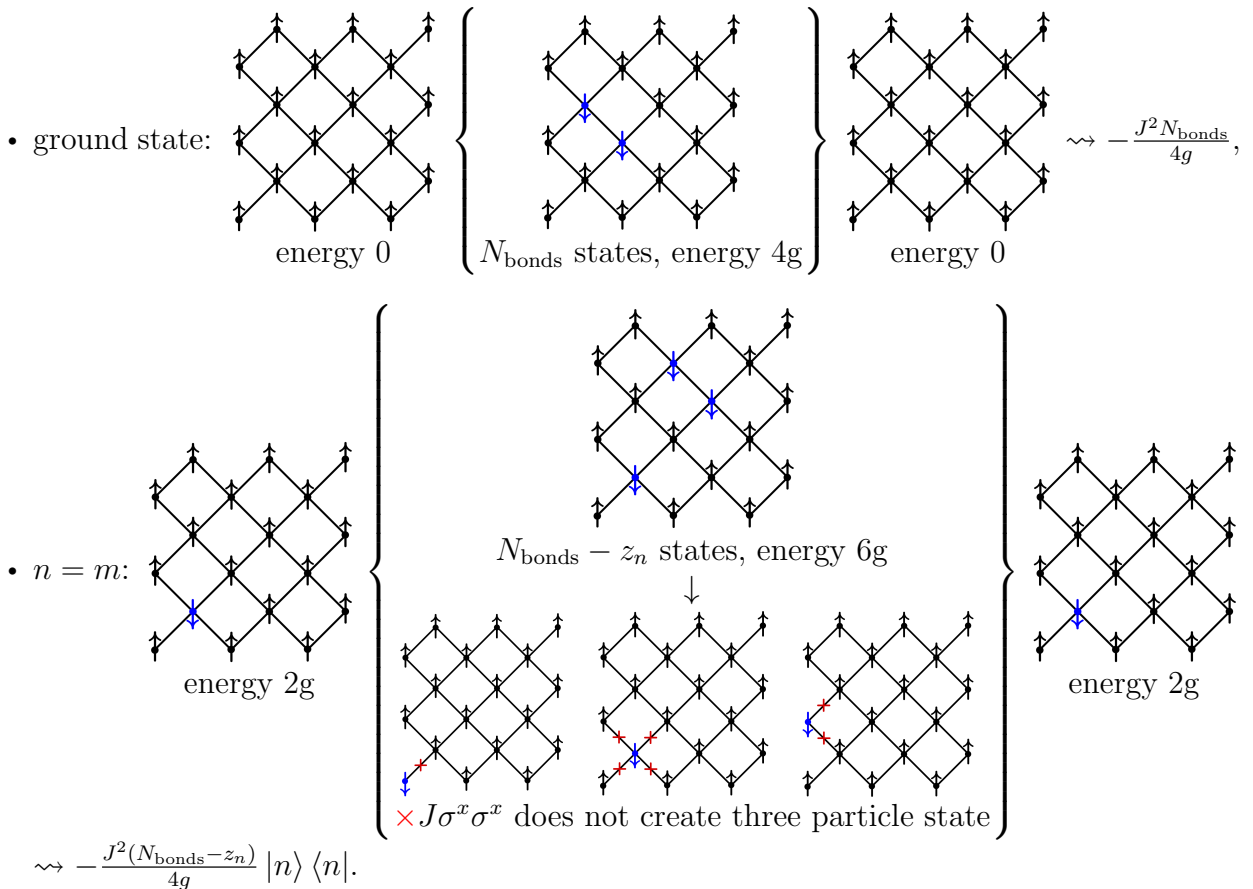
Before plotting the actual energies (6.78), let us derive a perturbative theory. We go deep into the paramagnetic phase ($g = 3.5$), where the single $\uparrow \rightsquigarrow \downarrow$ spin flip excitations effectively describe a single particle with hopping Hamiltonian

$$H_{\text{eff}} = \mu \sum_n |n\rangle\langle n| - t \sum_{\langle n,m \rangle} (|n\rangle\langle m| + |m\rangle\langle n|). \quad (6.79)$$

The uniform³ bond Hamiltonians (6.74) translate to

$$h_{n,m} = \frac{\mu}{2} |n\rangle\langle n| + \frac{\mu}{2} |m\rangle\langle m| - t(|n\rangle\langle m| + |m\rangle\langle n|) \quad n, m \text{ NN.} \quad (6.80)$$

In section 2.2 we derived the values $\mu = 2g$ and $t = J = 1$ for on-site energies and hopping. These hold for both PBC and OBC up to first order perturbation theory. For OBC in second order⁴, however, the on-site energy is shifted by a value that is site-dependent and proportional to the number of nearest neighbors z_n :



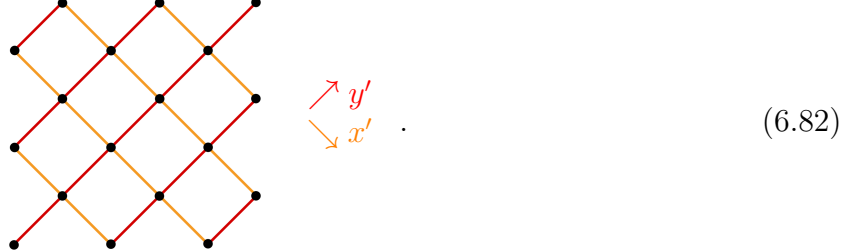
Since we are interested in the excitation energy relative to the ground state, we do not consider $-J^2 N_{\text{bonds}}/4g$ in the on-site energies. Taken first and second order together, the effective hopping parameters are

$$\mu_n = 2g + \frac{J^2}{4q} z_n, \quad t = 1. \quad (6.81)$$

³Note that we do not divide μ by the local coordination number and consequently $H_{\text{eff}} \neq \sum_{\langle n,m \rangle} h_{n,m}$ and the defined bond energies do not sum up to the total eigenenergy.

⁴We continue the effective Hamiltonian method (2.7) in second order, now for the diagonal square lattice.

If we worked on a conventional square lattice, we would expect the eigenstates of the corresponding Hamiltonian (6.79) to describe superpositions of 1D standing wave configurations (as we observed them in figure 5.3 for MPS) along the two axes x , y . We would label them with integer wave numbers k_x , k_y and two excitations with same $k_x + k_y$ would have the same energy due to the 90° rotation symmetry. For our rotated square lattice, we can restore the two axes along the diagonals:



So the overall picture of standing waves across x' , y' and corresponding quantum numbers $k_{x'}$, $k_{y'}$ stays the same. However, our choice of boundaries break the 90° rotation symmetry. In combination with the second order shift in on-site energies (6.81), which depend on the local coordination numbers, this asymmetry lifts the energy degeneracies for eigenstates with same $k_{x'} + k_{y'}$.

We now reinforce these perturbative expectations numerically and compare them to the actual results provided by (6.78), for the different optimization approaches (6.61), (6.63) and (6.73).

In figure 6.7, we diagonalize the single particle Hamiltonian (6.79) with parameters (6.81) at $g = 3.5$, for the four algebraically smallest eigenvalues. We visualize the corresponding bond energies—i.e. the expectation values of (6.80)—in a color plot. We find the expected superpositions of standing waves along the diagonal axes, for $L_x = L_y = 100, 10, 5, 3$ with decreasing resolution. The headline of each panel specifies the energy and inferred wave numbers of the corresponding eigenstate. We conclude that the $(k_{x'}, k_{y'}) = (2, 1)$ standing wave has a slightly lower energy than $(1, 2)$, manifesting the broken rotation symmetry.

In figure 6.8, for $L_x = L_y = 3$, we exactly diagonalize the TFI Hamiltonian (2.1) and take the four lowest eigenstates as optimization references for (6.61). As expected, the isoPEPS quasiparticle ansatz captures the excitations better and better with increasing variational power, i.e. with increasing maximal bond dimension $D_{\max} = 2, 4, 6$. This is evident both quantitatively and visually, from the achieved overlaps (shown in the headline of each panel) and the corresponding bond energy colorplots. A bond dimension $D_{\max} = 4$ is sufficient to capture all features and achieve overlap deviations of about 1%. For $D_{\max} = 6$, the variational approximations are quasi-exact with overlaps ≥ 0.9993 , while the number of free parameters (53,195) remains only about 20% of the total Hilbert space dimension ($2^{18} = 262,144$).

In figure 6.9, we perform the same procedure as in figure 6.8, but now for a larger system of $L_x = L_y = 5$ and VQPE MPS as reference for (6.63). Due to the exponential memory cost of $\mathcal{O}(D_{\max}^{2L_y-1})$, we only reach $D_{\max} = 3$. However, even this small bond dimension is sufficient for a good approximation of the low-energy excitations, with overlaps deviating by about 1%.

After having shown that the quasiparticle ansatz (6.60) has the variational power to represent the low-energy excitations, we now turn to the question of whether we can find them by diagonalization of the effective Hamiltonian (6.73). To simplify the implementation, we compress the boundaries (6.71) and (6.72) variationally—similar to (6.35), but by bringing the different contributions into a unified bMPS form before compressing their sum. With the available hardware, we are restricted⁵ to $D_{\max} = 2, 3$ for $L_x = L_y = 5$. The results are shown in figure 6.10. The energy differences to the VQPE MPS reference now serve as a quantitative measure of success, which we list in the headlines of the bond energy colorplots. For $D_{\max} = 2$, the ground state already shows clear deviations, which are naturally inherited by the quasiparticle excitations on top. For instance, the second and third isoPEPS excitations have contributions from both the $(k_{x'}, k_{y'}) = (2, 1)$ and $(1, 2)$ standing wave references, since the energy errors of the former are substantially larger than the degeneracy lifting of the latter. As expected, going to $D_{\max} = 3$ significantly improves both the total eigenenergies and the local wave patterns, indicating that the optimization algorithm successfully converges.

⁵As discussed in the outlook, the boundary compression for the excitations might benefit from (i) individual environments for the variational compression, or (ii) a slightly adapted variant of the bulk-weighted scheme (6.37). We could not implement these improvements for this thesis due to time restrictions.

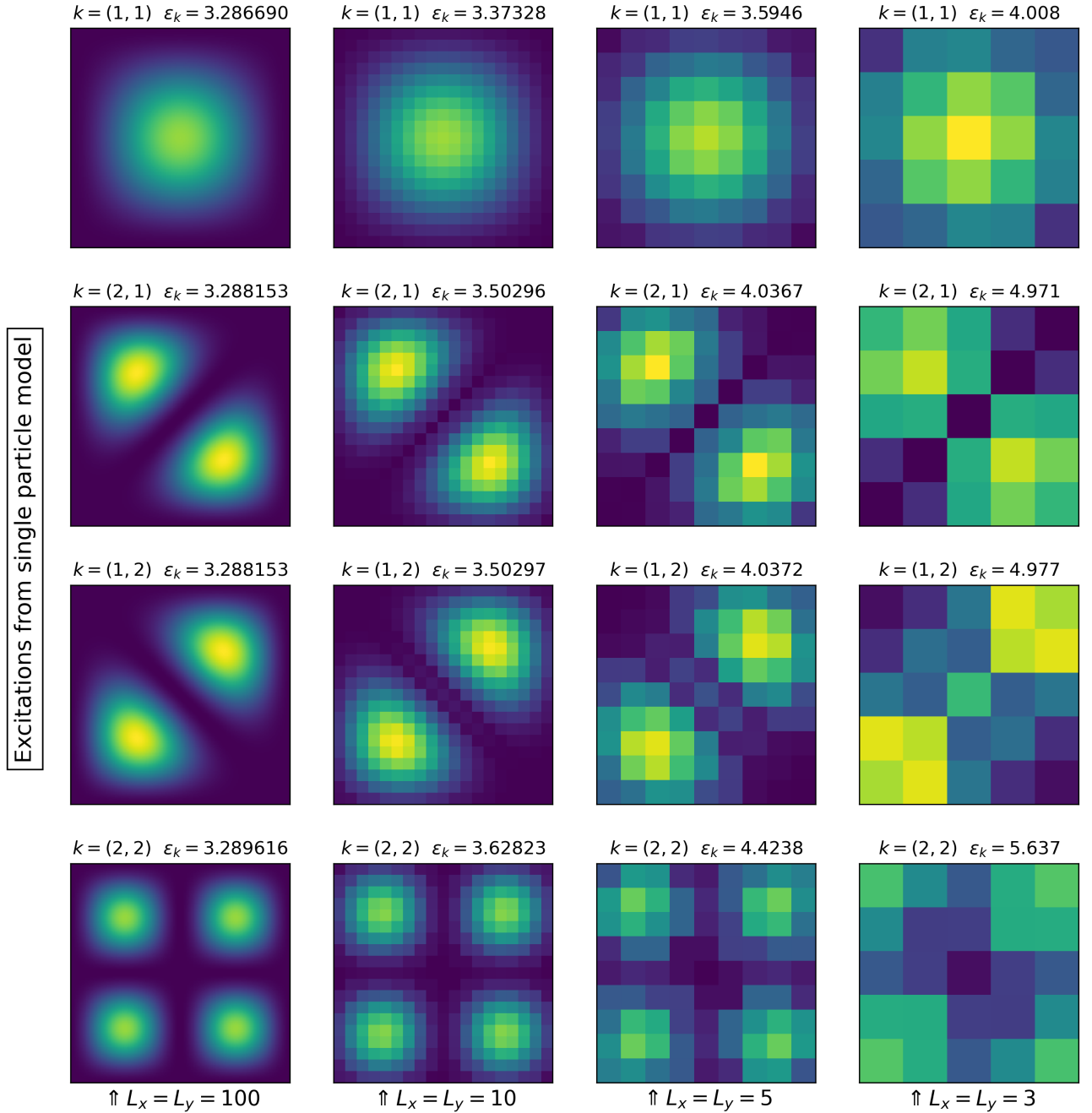


Figure 6.7: Bond energies for the four lowest-lying eigenstates of the single particle Hamiltonian (6.79) with parameters (6.81) at $g = 3.5$. We observe standing wave configurations along the two diagonal axes. The connectivity asymmetry of the lattice (6.82), in combination with the coordination-number-dependent chemical potential, slightly lifts the degeneracy between the excitations with wave numbers $(2, 1)$ and $(1, 2)$ —for finite system sizes. In the leftmost column we approach the thermodynamic limit with $L_x = L_y = 100$. Moving to the right, we reduce the system size via $L_x = L_y = 10$ to $L_x = L_y = 5$ and 3. For the latter values, the isoPEPS quasiparticle excitation ansatz is benchmarked in figures 6.8, 6.9, and 6.10.

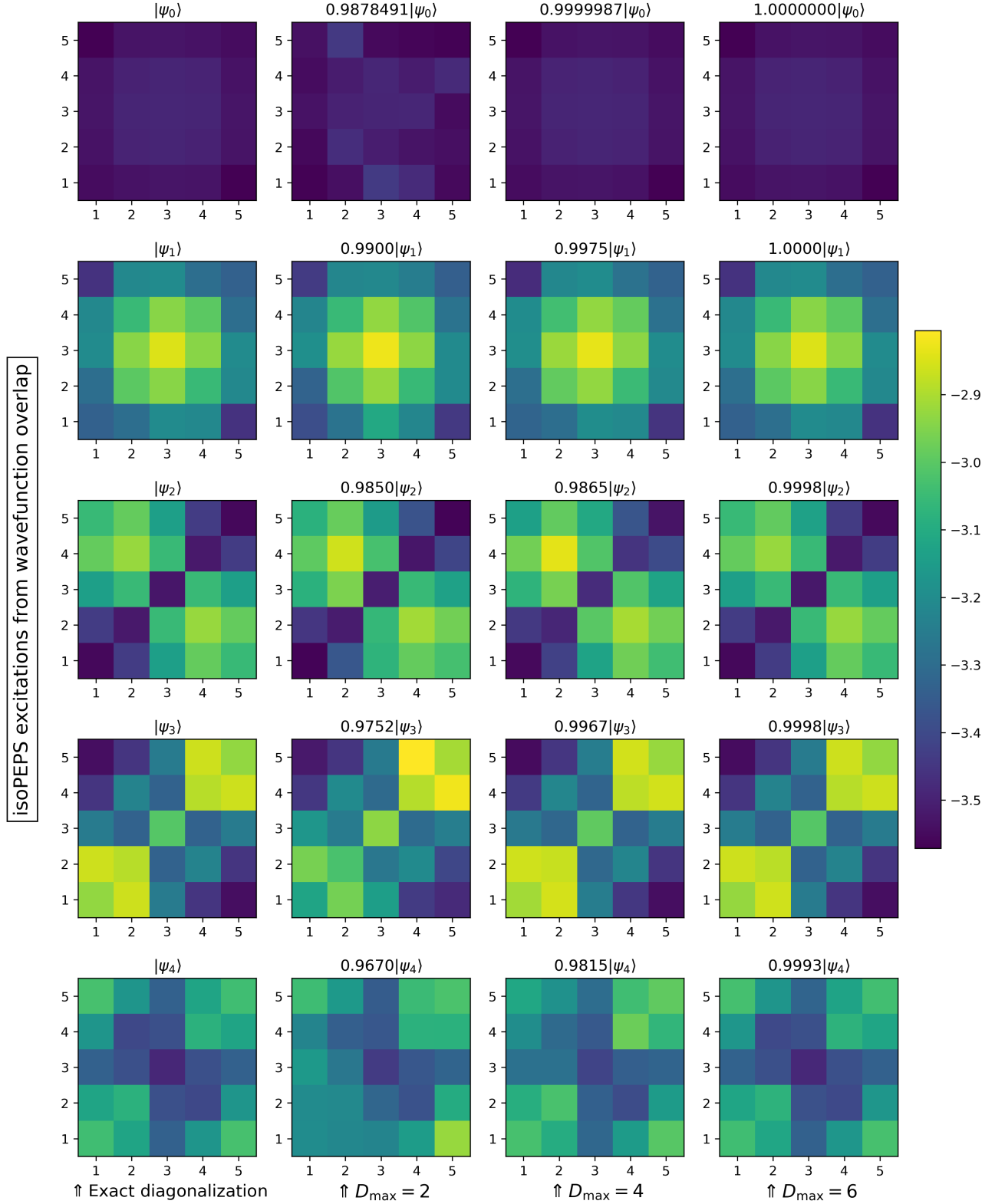


Figure 6.8: Bond energies of the four lowest-lying isoPEPS quasiparticle excitations (6.60), optimized from overlaps with the exact wavefunctions according to (6.61). From left to right, going from $D_{\max} = 2$ via $D_{\max} = 4$ up to $D_{\max} = 6$, the overlaps get closer to 1 and the standing wave configurations look more similar to the exact (leftmost column) and perturbative (figure 6.7) ones. Data for $L_x = L_y = 3$, at $g = 3.5$ in the paramagnetic phase of the TFI model.

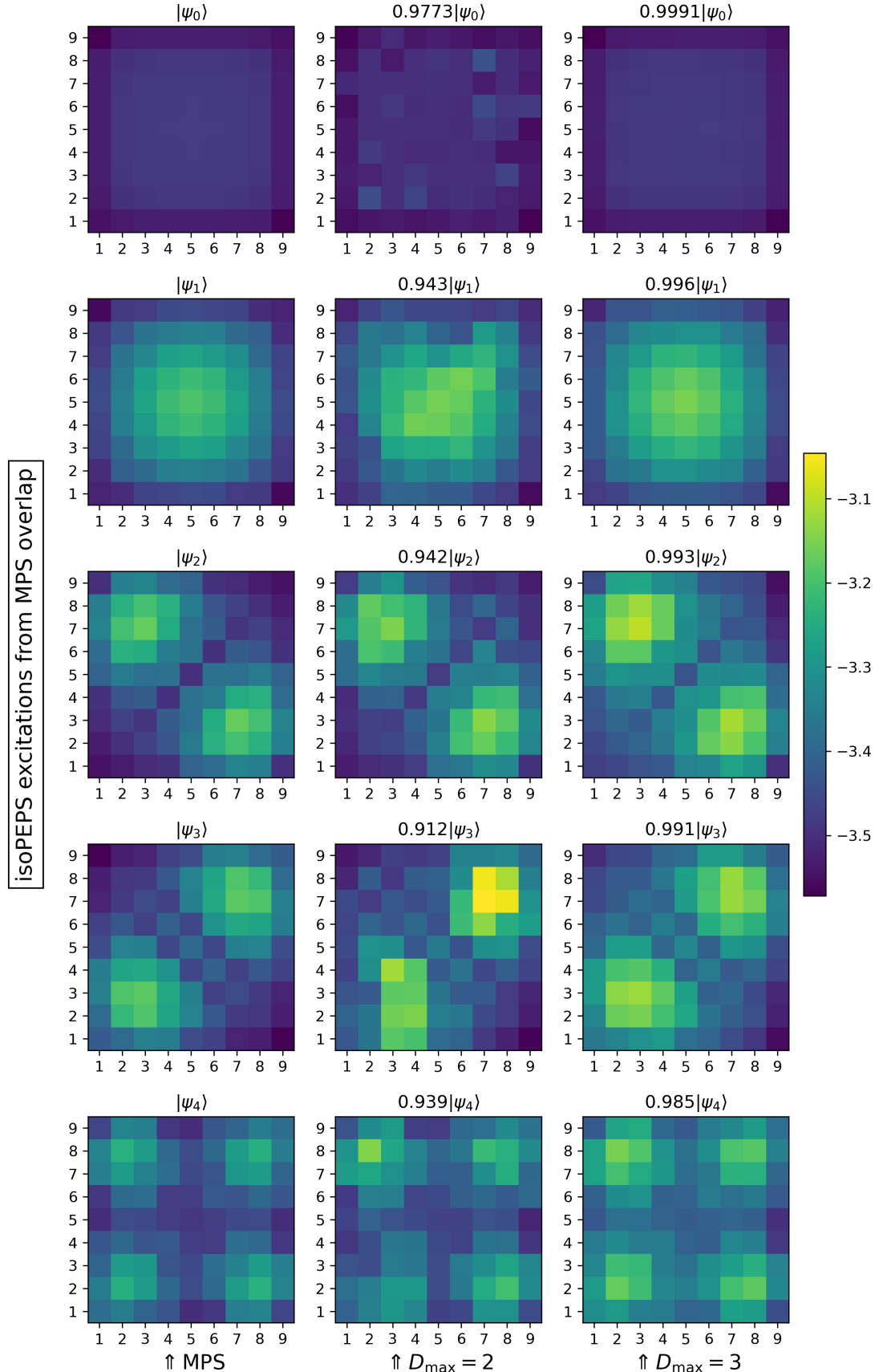


Figure 6.9: Bond energies of the four lowest-lying isoPEPS quasiparticle excitations (6.60), optimized from overlaps with VQPE MPS according to (6.63). Going from $D_{\max} = 2$ to $D_{\max} = 3$, the overlaps get significantly closer to 1 and the standing wave configurations look more similar to the MPS (leftmost column) and perturbative (figure 6.7) ones. Data for $L_x = L_y = 5$, at $g = 3.5$ in the paramagnetic phase of the TFI model.

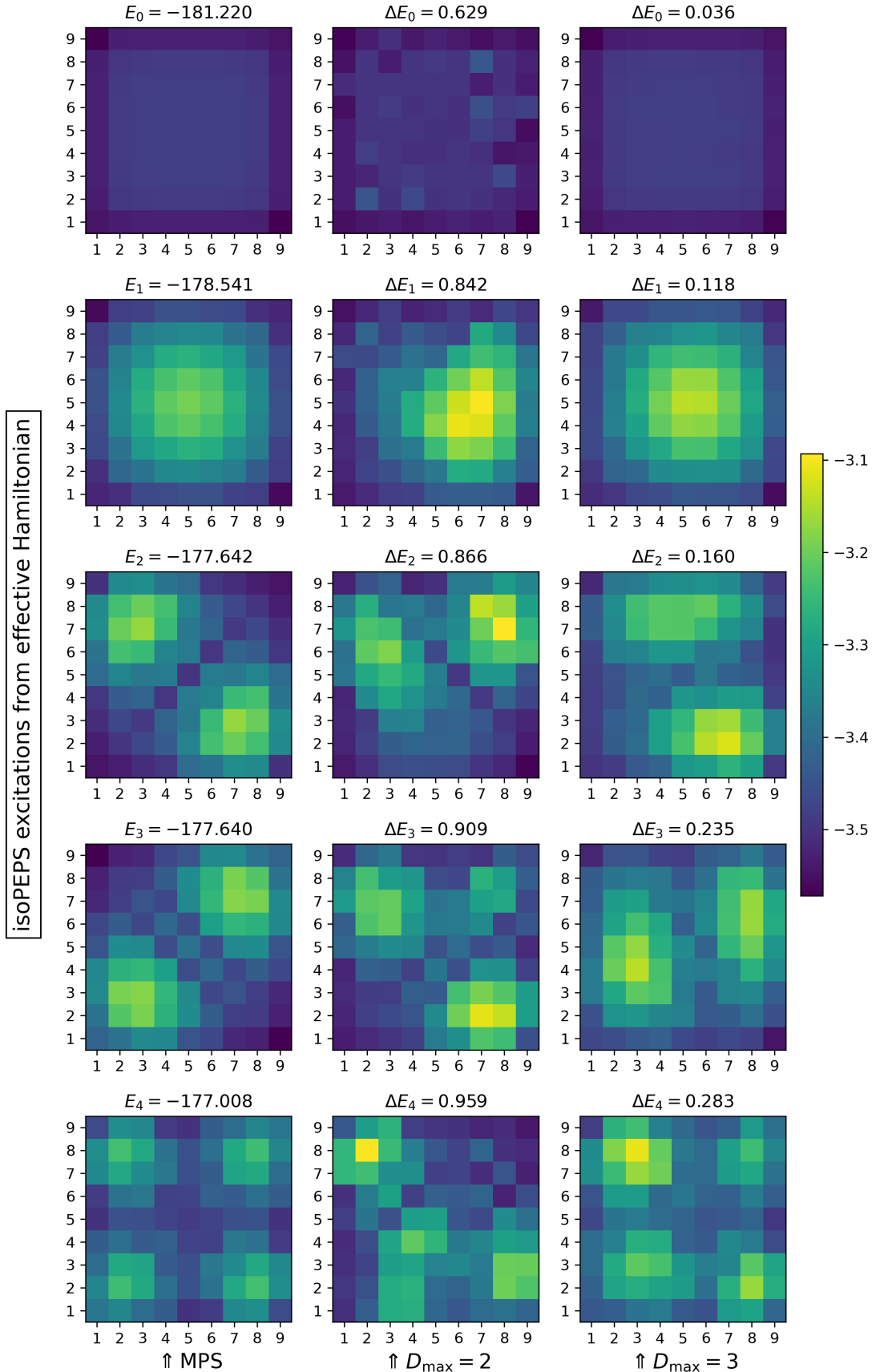


Figure 6.10: Bond energies of the four lowest-lying isoPEPS quasiparticle excitations (6.60), optimized by diagonalization of the effective Hamiltonian (6.73). Compared to the MPS reference (leftmost column), when going from $D_{\max} = 2$ to $D_{\max} = 3$, the energy differences become smaller and the standing wave configurations look more similar, indicating that the optimization algorithm successfully converges. Data for $L_x = L_y = 5$, at $g = 3.5$ in the paramagnetic phase of the TFI model.

Chapter 7

Conclusion and outlook

In this thesis, we variationally optimized ground states within manifolds of isometric tensor network states and, oriented towards the tangent space, quasiparticle excitations on top. In the following, we provide a concise summary of the central components: the ansätze, the corresponding optimization algorithms, and the main numerical results for the TFI model. Parts 1) and 2) reproduce well-established methods, while part 3) contains the newly developed bulk-weighted boundary compression and the quasiparticle excitation ansatz for isoPEPS:

1) Uniform matrix product states (uMPS)

The translation invariant state (4.1) on an infinite chain is completely characterized by a single rank-3 tensor. Within the gauge freedom (4.8), via iterative positive QR decompositions (4.18), we can isolate a normalized center tensor that is surrounded by isometries (4.20). To optimize for the ground state, the VUMPS algorithm (A1–A3) forces the residual of the Schrödinger equation—which is not exactly solvable within the manifold—to be orthogonal to the tangent space. The latter serves as variational space for quasiparticle excitations (4.58) against the correlated ground state vacuum. They arise from a superposition of local tensor perturbations, which are gauged (4.60) such that orthogonality to the ground state (4.62) and identity norm matrix (4.63) are ensured. Due to translation invariance, we can impose a well-defined momentum that gives direct access to the dispersion relation (figure 4.3). In the boundary terms of all effective Hamiltonians, we deal with infinite geometric sums (4.47, 4.70) of transfer matrices (4.2). To compute them, we make explicit use of the primitivity property (4.5).

2) Matrix product states (MPS)

Compared to 1), we restrict the chain to a finite length and make the tensors site-dependent (5.2). For OBC, the canonical form (5.12) can be reached via two half-sweeps of LQ (5.8) and singular value (5.10) decompositions. The DMRG algorithm (5.24–5.26) finds a faithful ground state approximation by solving the effective eigenvalue problem for two tensors at a time, followed by SVD truncation and shift to the next site. Completely analogous to uMPS, but without the explicit plane wave coefficient, the excitation ansatz (5.28) superposes local tensor perturbations and gauges them (5.30) so that they are orthogonal to the ground state and pairwise to each other (5.32). By choosing PBC for the Hamiltonian, momentum can be restored as a good quantum number, either (a) after or (b) together with energy optimization (figure 5.2). For OBC, the excitations describe standing wave configurations with nodes at the boundaries (figure 5.3). Environments (5.35, 5.44) are contracted by recursively summing up the tensors that (i) newly apply a perturbation to the trivial boundary, and (ii) transfer the boundary of all perturbations that already have been applied.

3) Isometric projected entangled pair states (isoPEPS)

On a diagonal square lattice with OBC (6.6), we impose the isometric conditions (6.7–6.11) on a strict subset (6.12) of 2D tensor network states (6.4). The orthogonality column can be shifted approximately with the YB move (6.17) and allows to implement a squared variant (6.48, 6.49) of the successful 1D DMRG algorithm. The boundaries (6.29) can in general only be contracted approximately. Seeing the two legs that stick out on each site as one "physical" leg of dimension D_{\max}^2 , this corresponds to a bMPS compression. To be precise, to an additive compression of the two terms (i) $(L_h^{\text{new}}|$ that newly applies a column MPO to the identity boundary, and (ii) $(L_h^{\text{transfer}}|$ that transfers the boundary of all previously applied column MPOs. The standard procedure is given by a variational sweep (6.35) over a bMPS $(L_h|$ with fixed bond dimension $\chi_{\max,b}$. In this way, all states in the variational space of dimension $D_{\max}^{2(2L_y-1)}$ are weighted equally, with no regard to the bulk of the isoPEPS. Consequently, the compression fidelity worsens when capturing a smaller fraction of the space, as happens when increasing D_{\max} while scaling $\chi_{\max,b} = 6D_{\max}^2$. For $D_{\max} > 4$, this deterioration becomes evident both in the energy expectation value (figure 6.1) and its minimization with DMRG² (figures 6.2–6.6). These findings motivated us to propose a new **bulk-weighted boundary compression** (6.37–6.43). It requires the target bMPS $(L_h|$ and the sum to be compressed—namely, $(L_h^{\text{new}}| + (L_h^{\text{transfer}}|$ —to approximately have the same expectation value with the double orthogonality column $|CC\rangle$ positioned right next to them. Due to the isometric structure of the isoPEPS, the latter contains the entire information about the bulk. With this compression method we reach significantly lower energy errors when computing the expectation value (figure 6.1) or running DMRG² (figures 6.2–6.6).

To create **isoPEPS quasiparticle excitations**, we start from the tangent space of a ground state $|\psi(A_L, C)\rangle$ (6.51). A subtle difference to MPS is given by the fact that the orthogonality column C remains nontrivial when located to the right of all left isometric site tensors. This requires including the derivative with respect to each of its components when forming the tangent space vector (6.52). In a fashion analogous to MPS, we parametrize the perturbation tensors (6.58) and (6.59) such that all desired orthogonality conditions (6.54) are satisfied. While for MPS this is exactly covered by the gauge freedom, our isoPEPS parametrization does not span the full tangent space. It projects out more directions than strictly necessary to remove the obvious zero-modes (6.55), although the closed loops in the isoPEPS bonds may allow additional gauge transformations that are not as straightforward to write down and depend on the specific representation of the reference ground state. In any case, by enforcing the orthogonality relations (6.54), we ensure that the map $X \mapsto |\psi(X; A_L, C)\rangle$ (6.60) is injective, making the variational problem well-defined. We solve it (i) via overlap with exact wavefunctions (6.61) or MPS (6.63), and (ii) by diagonalization of the effective Hamiltonian (6.73). The resulting states provide good approximations of the low-energy standing wave excitations in the paramagnetic phase of the TFI Hamiltonian (figures 6.7–6.10).

Reaching higher bond dimensions for excitations

Using our current implementation of the effective Hamiltonian (6.73), we can optimize the ansatz only up to $D_{\max} = 3$ on the available hardware. Memory and runtime costs could potentially be reduced by improving the boundary compressions (6.71) and (6.72). At present,

we perform them variationally and treat the different contributions in a unified way, by contracting them into a double-site shape and performing QR decompositions before compressing their sum. For the third term in (6.72), for instance, this scales with $\mathcal{O}(D_{\max}^6 \chi_{\max,b}^3 \chi_{\max,c}^3)$ in runtime and with $\mathcal{O}(D_{\max}^4 \chi_{\max,b}^2 \chi_{\max,c}^2)$ in memory per site. A more efficient approach would be to introduce individual environments for each overlap with the bMPS being swept over. In addition to these improvements within the variational compression scheme, it is worthwhile to investigate whether the new bulk-weighted compression, suitably adapted, also brings an advantage for excitations. For boundaries containing a B -column in the ket, one could form the expectation value with a single ground state orthogonality column in the bra.

Application to conventional MM isoPEPS

Originally, isoPEPS were introduced for the conventional, unrotated square lattice [ZP20]:

$$|\text{isoPEPS}\rangle = \begin{array}{c} \text{Diagram of a 4x4 square lattice with black dots at grid points. Blue arrows indicate horizontal and vertical connections between adjacent sites. A central vertical column of four blue dots represents the orthogonality column. Arrows point from the left and right sides towards the center. The bottom row has arrows pointing left and right, while the top row has arrows pointing up and down. The left and right columns have arrows pointing inwards towards the center. The top and bottom rows have arrows pointing outwards from the center.} \end{array}. \quad (7.1)$$

Here, the orthogonality column is shifted with a scheme dubbed the *Moses move* (MM). It merges $C^{[x]}$ with the adjacent isometric column $A_R^{[x+1]}$ into $A_C^{[x+1]}$ and then splits the latter back into two columns $\tilde{A}_L^{[x+1]}, \tilde{C}^{[x+1]}$:

$$\begin{array}{ccccccc} \text{Diagram 1: } & = & \text{Diagram 2: } & = & \text{Diagram 3: } & \approx \dots \approx & \text{Diagram 4: } \\ \text{Diagram 1 shows a 4x4 lattice with a central vertical column of blue dots. Diagram 2 shows the same lattice after a Moses move, where the central column has shifted. Diagram 3 shows the lattice after splitting the merged column back into two. Diagram 4 shows the final state. Arrows indicate the flow of legs and the merging/splitting process.} \end{array} \quad (7.2)$$

The crucial tripartite tensor decomposition works the same way as the one we described in (6.17) for the YB move.

It would be interesting to set up and test a quasiparticle excitation ansatz for these MM isoPEPS as well. Notably, our diagonal isoPEPS ansatz is not straightforwardly transferable. This is due to the fact that not all outgoing legs of the A_L -tensors are connected with the orthogonality column that is located right next to them. As a consequence, replacing one A_L with $V_L X$ —to fulfill the orthogonality conditions (6.54)—the perturbation X cannot be absorbed into the orthogonality center.

Unlike the excitation ansatz, our newly proposed bulk-weighted boundary compression is directly applicable to MM isoPEPS. Regarding boundary compression in general and this new method in particular, it would be worthwhile to investigate potential performance differences between the two lattice choices.

Infinite version with definite momentum

In order to put our quasiparticle excitations in a plane wave superposition with definite momentum, we need a uniform version of the isoPEPS. For the conventional MM isoPEPS, infinite columns were established in [WAL⁺23], but an infinite extension in both directions is still missing (for MM and diagonal isoPEPS). It requires finding a fixed-point solution of $A_L C = C A_R$, the column analog of the tensor equation that appeared for the canonical form of uMPS in section 4.2. There, we could reach convergence with iterative positive QR decompositions (4.18). There is no a priori reason to achieve the same with repeatedly applying the MM or YB move.

Application to more challenging models

In this thesis, we benchmarked all algorithms on the TFI model. Naturally, having established that they work on this comparatively simple model, it is desirable to apply them to more challenging systems, such as quantum spin liquids (QSL) mentioned in the introduction. Of special interest are numerical predictions about quantities that are directly accessible in experiments on candidate materials. Inelastic neutron scattering, for instance, measures the dynamical structure factor. It results from a space-time Fourier transformation of the dynamical two-point correlation function $C(n, t)$ for a local operator O :

$$S(p, \omega) = \frac{1}{2\pi} \int_{-\infty}^{\infty} dt \sum_n e^{i(\omega t - p \cdot n)} C(n, t) \quad \text{with } C(n, t) = \langle \psi_0 | e^{iHt} O^{[n]} e^{-iHt} O^{[0]} | \psi_0 \rangle. \quad (7.3)$$

In the following, we sketch two possible routes for computing $S(p, \omega)$ with tensor network methods.

1) Lowest-lying excitation branch from quasiparticle ansatz

By projecting the time evolution onto all excited states of H , we can simplify the correlation function as

$$C(n, t) = \sum_X e^{-i(E_X - E_0)t} \langle \psi_0 | O^{[n]} | \psi_X \rangle \langle \psi_X | O^{[0]} | \psi_0 \rangle. \quad (7.4)$$

We perform the Fourier transformation in time, denote with $\epsilon_X = E_X - E_0$ the energy above the ground state and end up with

$$S(p, \omega) = \sum_{X,n} e^{-ip \cdot n} \langle \psi_0 | O^{[n]} | \psi_X \rangle \langle \psi_X | O^{[0]} | \psi_0 \rangle \delta(\omega - \epsilon_X). \quad (7.5)$$

With the tangent space ansatz (6.60), we can only capture the isolated branch of single quasiparticle excitations, corresponding to a subset of terms in the sum over X in $S(p, \omega)$. For an overlap $\langle \psi_0 | O^{[n]} | \psi_X \rangle$ —that contributes to the spectral weight at momentum p after the Fourier sum—all states in the superposition $|\psi_X\rangle$, which have the excitation tensor left of the operator $O^{[n]}$, can be neglected due to the ground state orthogonality condition (6.54) 1). The nonzero terms, where the excitation tensors are right of the operator $O^{[n]}$, can be computed with the compressed bMPS (6.71).

2) Full excitation spectrum from time evolution

Alternatively, we can compute the correlation function $C(n, t)$ explicitly by (i) finding a ground state approximation $|\psi_0\rangle$, (ii) applying the local operator $O^{[0]}$, (iii) time-evolving the perturbed state with e^{-iHt} and (iv) computing the overlap with $O^{[n]} |\psi_0\rangle$:

$$C(n, t) = e^{iE_0 t} \langle \psi_0 | O^{[n]} \underbrace{e^{-iHt} O^{[0]} | \psi_0 \rangle}_{=|\psi(t)\rangle} = e^{iE_0 t} \langle \psi_0 | O^{[n]} | \psi(t) \rangle. \quad (7.6)$$

Then, we perform the Fourier transformation in space and time (where we multiply the time signal by a Gaussian window function to suppress artifacts arising from the finite time cutoff). In contrast to the quasiparticle ansatz, the time evolution accounts for the full excitation spectrum and can thus capture two particle scattering continua in $S(p, \omega)$. The downside is typically a higher computational cost.

In [DVMP23] these two approaches show excellent agreement for the dynamical spin structure factor of the highly frustrated, anti-ferromagnetic J_1 - J_2 Heisenberg model on a triangular lattice. They were implemented for an MPS on a cylindrical geometry. It would be interesting to see whether the obtained results can be reproduced with isoPEPS methods. Since TEBD² (at least without the use of SWAP gates) cannot be applied to models with next-nearest-neighbor interactions (such as the J_1 - J_2 model), a 2D version of TDVP is another further research direction.

Towards a tangent space projector and TDVP

The time-dependent variational principle (TDVP) projects the right hand side of the Schrödinger equation onto the tangent space of the manifold at the current state:

$$\frac{d}{dt} |\psi(A)\rangle = -i P_{|\psi(A)\rangle} H |\psi(A)\rangle. \quad (7.7)$$

This ensures that the state never leaves the manifold and can be described in terms of time-evolving tensors $|\psi(A_t)\rangle$ [HLO⁺16]. The following advantages over TEBD make TDVP particularly powerful for accurate long-time evolution [HOV13]:

- In its one-site formulation, TDVP exactly conserves the energy (and other symmetries of the Hamiltonian).
- TDVP does not rely on splitting the Hamiltonian into local gates. Consequently, it avoids the Trotter error present in TEBD and can be applied to Hamiltonians with long-range interactions.

To implement TDVP for isoPEPS, we need an expression for the projector $P_{|\psi(A_L, C)\rangle}$ onto the tangent space, which is spanned by the states $|\psi(B, D; A_L, C)\rangle$ (6.52). Our parametrization $(B, D)(X)$ according to (6.58, 6.59) ensures an identity norm matrix (6.54) and allows us to solve the minimization problem $\arg \min_X \|\psi(X; A_L, C) - \varphi\|^2$ for an arbitrary state φ easily and express its projection onto the tangent space as

$$P_{|\psi(A_L, C)\rangle} |\varphi\rangle = |\psi(X_\varphi; A_L, C)\rangle \text{ with } X_\varphi = \partial_{\bar{X}} \langle \psi(\bar{X}; \bar{A}_L, \bar{C}) | \varphi \rangle. \quad (7.8)$$

To make a statement about the exactness of $P_{|\psi(A_L, C)\rangle}$, we have to ultimately find all gauge transformations (in addition to (6.55)) that leave the tangent space vector $|\psi(B, D; A_L, C)\rangle$ invariant.

Chapter A

Detailed Jordan-Wigner and Bogoliubov transformation

Guided by [Pfe70] and [Sac11], we present detailed analytical calculations which diagonalize the transverse field Ising model in one spatial dimension. The Hamiltonian with periodic boundary conditions $\sigma_{N+1}^x \equiv \sigma_1^x$ is given by

$$H = -J \sum_{n=1}^N \sigma_n^x \sigma_{n+1}^x - g \sum_{n=1}^N \sigma_n^z. \quad (\text{A.1})$$

The essential tool is the *Jordan-Wigner transformation*, mapping spin-1/2 degrees of freedom to spinless fermions. On every site, we associate the spin-up state with an empty orbital and the spin-down state with an occupied orbital. This fixes the relation

$$\sigma_n^z = 1 - 2c_n^\dagger c_n, \quad (\text{A.2})$$

where c_n^\dagger and c_n denote the fermionic creation and annihilation operators. They have to fulfill the anti-commutation relations

$$\{c_n, c_m\} = \{c_n^\dagger, c_m^\dagger\} = 0, \quad \{c_n, c_m^\dagger\} = \delta_{nm}. \quad (\text{A.3})$$

Naively we may set c_n equal to $\sigma_n = \frac{1}{2}(\sigma_n^x + i\sigma_n^y)$ (flipping the spin from down to up) and c_n^\dagger equal to $\sigma_n^\dagger = \frac{1}{2}(\sigma_n^x - i\sigma_n^y)$ (flipping the spin from up to down). But spin operators commute on different sites:

$$[\sigma_n^\alpha, \sigma_m^\beta] = 0 \text{ for } n \neq m, \quad \sigma_n^\alpha \sigma_n^\beta = \delta_{\alpha\beta} \mathbb{1} + i\epsilon_{\alpha\beta\gamma} \sigma_n^\gamma. \quad (\text{A.4})$$

The solution to this dilemma is the introduction of the highly non-local Jordan-Wigner string

$$\eta_n = \prod_{m < n} \sigma_m^z = \prod_{m < n} (1 - 2c_m^\dagger c_m) = (-1)^{\sum_{m < n} c_m^\dagger c_m} = \eta_n^\dagger. \quad (\text{A.5})$$

The following mappings are consistent with all commutation and anti-commutation relations:

$$\sigma_n = \eta_n c_n, \quad \sigma_n^\dagger = \eta_n c_n^\dagger. \quad (\text{A.6})$$

For the Pauli-x and Pauli-y matrices they translate to

$$\sigma_n^x = \sigma_n^\dagger + \sigma_n = \eta_n(c_n^\dagger + c_n), \quad \sigma_n^y = i(\sigma_n^\dagger - \sigma_n) = i\eta_n(c_n^\dagger - c_n). \quad (\text{A.7})$$

Let us prove the consistency of (A.3) with (A.4). For this we use the following identities, which directly follow from (A.3):

$$[c_n, c_m^\dagger c_m] = \delta_{nm} c_n, \quad [c_n^\dagger, c_m^\dagger c_m] = -\delta_{nm} c_n^\dagger, \quad [c_n^\dagger c_n, c_m^\dagger c_m] = 0, \quad (\text{A.8})$$

$$(c_n^\dagger + c_n)(1 - 2c_n^\dagger c_n) = -(1 - 2c_n^\dagger c_n)(c_n^\dagger + c_n) = c_n^\dagger - c_n. \quad (\text{A.9})$$

The Jordan-Wigner string is not needed for relations on the same site and can be made ineffective using $[\eta_n, c_n] = [\eta_n, c_n^\dagger] = 0$ and $\eta_n^2 = 1$. It is essential though for the relations $[\sigma_n^\alpha, \sigma_m^\beta] = 0$, with $n \neq m$ and $\alpha, \beta \in \{x, y\}$. We exemplarily prove the one for $\alpha = \beta = x$, the others are structurally similar. W.l.o.g assume $m > n$:

$$\begin{aligned} \sigma_n^x \sigma_m^x &= \eta_n(c_n^\dagger + c_n) \eta_m(c_m^\dagger + c_m) \\ &= \eta_n(c_n^\dagger + c_n)(1 - 2c_n^\dagger c_n) \prod_{l=n+1}^{m-1} (1 - 2c_l^\dagger c_l)(c_m^\dagger + c_m) \eta_m \\ &= (-1)\eta_n(1 - 2c_n^\dagger c_n) \prod_{l=n+1}^{m-1} (1 - 2c_l^\dagger c_l)(c_n^\dagger + c_n)(c_m^\dagger + c_m) \eta_m \\ &= (-1)^2 \eta_m(c_m^\dagger + c_m) \eta_n(c_n^\dagger + c_n) \\ &= \sigma_m^x \sigma_n^x. \end{aligned} \tag{A.10}$$

Under the *Jordan-Wigner transformation*, the Ising interaction for $n < N$ translates to

$$\begin{aligned} \sigma_n^x \sigma_{n+1}^x &= \eta_n(c_n^\dagger + c_n) \eta_{n+1}(c_{n+1}^\dagger + c_{n+1}) \\ &= \eta_n^2(c_n^\dagger + c_n)(1 - 2c_n^\dagger c_n)(c_{n+1}^\dagger + c_{n+1}) \\ &= (c_n^\dagger - c_n)(c_{n+1}^\dagger + c_{n+1}). \end{aligned} \tag{A.11}$$

Connecting the last and first site we have to be careful. There are no spins left of site 1, so $\eta_1 = 1$. For the last Jordan-Wigner string we get

$$\eta_N = \prod_{n < N} (1 - 2c_n^\dagger c_n) = \prod_{n \leq N} (1 - 2c_n^\dagger c_n)(1 - 2c_N^\dagger c_N) = (-1)^{N_f} (1 - 2c_N^\dagger c_N), \tag{A.12}$$

where N_f denotes the total number of fermions in the system. Taken together we have

$$\sigma_N^x \sigma_1^x = (-1)^{N_f} (1 - 2c_N^\dagger c_N)(c_N^\dagger + c_N)(c_1^\dagger + c_1) = -P_f(c_N^\dagger - c_N)(c_1^\dagger + c_1), \tag{A.13}$$

where we defined the fermionic parity operator

$$P_f = (-1)^{N_f} = (-1)^{\sum_n c_n^\dagger c_n} = \prod_n \sigma_n^z. \tag{A.14}$$

To let (A.11) hold also for $n = N$, we impose PBC $c_{N+1} \equiv c_1$ for an odd number of fermions ($P_f = -1$) and APBC $c_{N+1} \equiv -c_1$ for an even number of fermions ($P_f = 1$). Then $[H, P_f] = 0$, i.e. the Hamiltonian block diagonalizes into the two parity sectors and we can diagonalize them independently. In the thermodynamic limit, we can stick to periodic boundary conditions and argue that the single correction term $+2J(c_N^\dagger - c_N)(c_1^\dagger + c_1)$ becomes negligible.

Inserting (A.2) and (A.11) into (A.1), we obtain the fermionic Hamiltonian

$$\begin{aligned} H &= - \sum_n \left[J(c_n^\dagger - c_n)(c_{n+1}^\dagger + c_{n+1}) + g(1 - 2c_n^\dagger c_n) \right] \\ &= - \sum_n \left[J(c_n^\dagger c_{n+1} + c_{n+1}^\dagger c_n + c_n^\dagger c_{n+1}^\dagger + c_{n+1} c_n) - 2g c_n^\dagger c_n + g \right]. \end{aligned} \tag{A.15}$$

Next we perform a *Fourier transformation* $c_n = \frac{1}{\sqrt{N}} \sum_p e^{-ipn} c_p$, with momenta $p = \frac{2\pi}{N} k$. The allowed k values are determined by the fermionic parity of N_f , and the parity of the system size N :

1) N_f odd: $e^{ipN} = 1 \Rightarrow$ integer quantization.

- N even: $k \in \{-\frac{N}{2} + 1, \dots, \frac{N}{2}\}$.
- N odd: $k \in \{-\frac{N-1}{2}, \dots, \frac{N-1}{2}\}$.

2) N_f even: $e^{ipN} = -1 \Rightarrow$ half-integer quantization.

- N even: $k \in \{-\frac{N-1}{2}, \dots, \frac{N-1}{2}\}$.
- N odd: $k \in \{-\frac{N}{2} + 1, \dots, \frac{N}{2}\}$.

The following calculations are valid for any of these four sectors. We use $\sum_n e^{i(p-\tilde{p})n} = N\delta_{p\tilde{p}}$ and $e^{ip} = \cos(p) + i\sin(p)$ for

$$\begin{aligned}
H &= -\frac{1}{N} \sum_{n,p,\tilde{p}} J \left(e^{ipn} e^{-i\tilde{p}(n+1)} c_p^\dagger c_{\tilde{p}} + e^{ip(n+1)} e^{-i\tilde{p}n} c_p^\dagger c_{\tilde{p}} + e^{ipn} e^{i\tilde{p}(n+1)} c_p^\dagger c_{\tilde{p}}^\dagger + e^{-ip(n+1)} e^{-i\tilde{p}n} c_p c_{\tilde{p}} \right) \\
&+ \frac{1}{N} \sum_{n,p,\tilde{p}} (2g e^{ipn} e^{-i\tilde{p}n} c_p^\dagger c_{\tilde{p}} - g) \\
&= \sum_p \left[-J \left(e^{-ip} c_p^\dagger c_p + e^{ip} c_p^\dagger c_p + e^{ip} c_{-p}^\dagger c_p^\dagger + e^{ip} c_{-p} c_p \right) + 2g c_p^\dagger c_p - g \right] \\
&= \sum_p \left[2(g - J \cos(p)) c_p^\dagger c_p - J e^{ip} (c_{-p}^\dagger c_p^\dagger + c_{-p} c_p) - g \right].
\end{aligned} \tag{A.16}$$

We can simplify the middle term by exploiting the symmetry under $p \rightarrow -p$:

$$\begin{aligned}
\sum_p e^{ip} (c_{-p}^\dagger c_p^\dagger + c_{-p} c_p) &= \sum_{0 < p < \pi} \left[e^{ip} (c_{-p}^\dagger c_p^\dagger + c_{-p} c_p) + e^{-ip} (c_p^\dagger c_{-p}^\dagger + c_p c_{-p}) \right] \\
&= \sum_{0 < p < \pi} (e^{ip} - e^{-ip}) (c_{-p}^\dagger c_p^\dagger + c_{-p} c_p) \\
&= \sum_{0 < p < \pi} 2i \sin(p) (c_{-p}^\dagger c_p^\dagger + c_{-p} c_p) \\
&= \sum_p i \sin(p) (c_{-p}^\dagger c_p^\dagger + c_{-p} c_p).
\end{aligned} \tag{A.17}$$

With this the Hamiltonian reads

$$H = \sum_p \left[2(g - J \cos(p)) c_p^\dagger c_p - iJ \sin(p) (c_{-p}^\dagger c_p^\dagger + c_{-p} c_p) - g \right]. \tag{A.18}$$

To diagonalize H , we define the *Bogoliubov transformation* for real numbers u_p and v_p :

$$\gamma_p = u_p c_p - i v_p c_{-p}^\dagger. \tag{A.19}$$

For γ_p defining proper fermionic operators, they have to inherit the canonical anti-commutation relations from c_p :

$$\begin{aligned}
\{\gamma_p, \gamma_{\tilde{p}}\} &= \{u_p c_p - i v_p c_{-p}^\dagger, u_{\tilde{p}} c_{\tilde{p}} - i v_{\tilde{p}} c_{-\tilde{p}}^\dagger\} = -i(u_p v_{-p} + u_{-p} v_p) \delta_{p,-\tilde{p}} \stackrel{!}{=} 0, \\
\{\gamma_p^\dagger, \gamma_{\tilde{p}}^\dagger\} &= \{u_p c_p^\dagger + i v_p c_{-p}, u_{\tilde{p}} c_{\tilde{p}}^\dagger + i v_{\tilde{p}} c_{-\tilde{p}}\} = i(u_p v_{-p} + u_{-p} v_p) \delta_{p,-\tilde{p}} \stackrel{!}{=} 0, \\
\{\gamma_p, \gamma_{\tilde{p}}^\dagger\} &= \{u_p c_p - i v_p c_{-p}^\dagger, u_{\tilde{p}} c_{\tilde{p}}^\dagger + i v_{\tilde{p}} c_{-\tilde{p}}\} = (u_p^2 + v_p^2) \delta_{p,\tilde{p}} \stackrel{!}{=} \delta_{p,\tilde{p}}.
\end{aligned} \tag{A.20}$$

We meet the conditions $u_p = u_{-p}$, $v_p = -v_{-p}$ and $u_p^2 + v_p^2 = 1$ with $u_p = \cos\left(\frac{\vartheta_p}{2}\right)$ and $v_p = \sin\left(\frac{\vartheta_p}{2}\right)$. For the rest of the calculations the following trigonometric identities are very useful:

$$\begin{aligned} u_p^2 - v_p^2 &= \cos^2\left(\frac{\vartheta_p}{2}\right) - \sin^2\left(\frac{\vartheta_p}{2}\right) = \cos(\vartheta_p), \\ 2u_p v_p &= 2 \cos\left(\frac{\vartheta_p}{2}\right) \sin\left(\frac{\vartheta_p}{2}\right) = \sin(\vartheta_p), \\ v_p^2 &= \sin^2\left(\frac{\vartheta_p}{2}\right) = (1 - \cos(\vartheta_p))/2. \end{aligned} \quad (\text{A.21})$$

Let us now insert the inverse of (A.19),

$$c_p = u_p \gamma_p + i v_p \gamma_{-p}^\dagger, \quad (\text{A.22})$$

into the Hamiltonian (A.18). For this compute separately the terms

$$\begin{aligned} c_p^\dagger c_p &= (u_p \gamma_p^\dagger - i v_p \gamma_{-p})(u_p \gamma_p + i v_p \gamma_{-p}^\dagger) \\ &= u_p^2 \gamma_p^\dagger \gamma_p + v_p^2 \gamma_{-p} \gamma_{-p}^\dagger - i u_p v_p (\gamma_{-p}^\dagger \gamma_p^\dagger + \gamma_{-p} \gamma_p), \end{aligned} \quad (\text{A.23})$$

$$\begin{aligned} c_{-p}^\dagger c_p^\dagger + c_{-p} c_p &= (u_p \gamma_{-p}^\dagger + i v_p \gamma_p)(u_p \gamma_p^\dagger - i v_p \gamma_{-p}) + (u_p \gamma_{-p} - i v_p \gamma_p^\dagger)(u_p \gamma_p + i v_p \gamma_{-p}^\dagger) \\ &= i u_p v_p (\gamma_p \gamma_{-p}^\dagger - \gamma_{-p}^\dagger \gamma_{-p} + \gamma_{-p} \gamma_{-p}^\dagger - \gamma_p^\dagger \gamma_p) + (u_p^2 - v_p^2) (\gamma_{-p}^\dagger \gamma_p^\dagger + \gamma_{-p} \gamma_p). \end{aligned} \quad (\text{A.24})$$

We demand that terms violating conservation of the γ -fermions (like $\gamma_{-p}^\dagger \gamma_p^\dagger$ and $\gamma_{-p} \gamma_p$) cancel out, requiring

$$\begin{aligned} 2(g - J \cos(p))(-i u_p v_p) - i J \sin(p)(u_p^2 - v_p^2) &\stackrel{!}{=} 0 \\ \Leftrightarrow \frac{u_p v_p}{u_p^2 - v_p^2} &= -\frac{J \sin(p)}{2(g - J \cos(p))} \\ \Leftrightarrow \tan(\vartheta_p) &= -\frac{J \sin(p)}{g - J \cos(p)}. \end{aligned} \quad (\text{A.25})$$

Next we simplify the remaining diagonal terms, again by exploiting the symmetry under $p \rightarrow -p$:

$$\begin{aligned} 2(g - J \cos(p))c_p^\dagger c_p + 2(g - J \cos(-p))c_{-p}^\dagger c_{-p} \\ = 2(g - J \cos(p))(u_p^2 \gamma_p^\dagger \gamma_p + v_p^2 \gamma_{-p} \gamma_{-p}^\dagger + u_p^2 \gamma_{-p}^\dagger \gamma_{-p} + v_p^2 \gamma_p \gamma_p^\dagger) \\ = 2(g - J \cos(p))(u_p^2 \gamma_p^\dagger \gamma_p + v_p^2 \gamma_p \gamma_p^\dagger) + 2(g - J \cos(-p))(u_{-p}^2 \gamma_{-p}^\dagger \gamma_{-p} + v_{-p}^2 \gamma_{-p} \gamma_{-p}^\dagger), \end{aligned} \quad (\text{A.26})$$

$$\begin{aligned} &- i J \sin(p)(c_{-p}^\dagger c_p^\dagger + c_{-p} c_p) - i J \sin(-p)(c_p^\dagger c_{-p}^\dagger + c_p c_{-p}) \\ &= 2 J \sin(p) u_p v_p (\gamma_p \gamma_p^\dagger - \gamma_{-p}^\dagger \gamma_{-p} + \gamma_{-p} \gamma_{-p}^\dagger - \gamma_p^\dagger \gamma_p) \\ &= 2 J \sin(p) u_p v_p (\gamma_p \gamma_p^\dagger - \gamma_p^\dagger \gamma_p) + 2 J \sin(-p) u_{-p} v_{-p} (\gamma_{-p} \gamma_{-p}^\dagger - \gamma_{-p}^\dagger \gamma_{-p}). \end{aligned} \quad (\text{A.27})$$

With (A.26) and (A.27) the Hamiltonian (A.18) takes the diagonal form

$$\begin{aligned} H &= 2 \sum_p [(g - J \cos(p))(u_p^2 \gamma_p^\dagger \gamma_p + v_p^2 \gamma_p \gamma_p^\dagger) - J \sin(p) u_p v_p (\gamma_p^\dagger \gamma_p - \gamma_p \gamma_p^\dagger) - g/2] \\ &= 2 \sum_p [(g - J \cos(p))(u_p^2 - v_p^2) - 2J \sin(p) u_p v_p] \gamma_p^\dagger \gamma_p \\ &\quad - \sum_p [-2(g - J \cos(p))v_p^2 - 2J \sin(p) u_p v_p + g]. \end{aligned} \quad (\text{A.28})$$

The trigonometric identities (A.21), and the fact that $J \cos(p)$ sums up to 0, help us to bring the two terms into the same form:

$$H = 2 \sum_p [(g - J \cos(p)) \cos(\vartheta_p) - J \sin(p) \sin(\vartheta_p)] (\gamma_p^\dagger \gamma_p - 1/2). \quad (\text{A.29})$$

We define $\epsilon_p/2 := (g - J \cos(p)) \cos(\vartheta_p) - J \sin(p) \sin(\vartheta_p)$ and compute its square by inserting (A.25) and using the trigonometric identities $\cos^2(\vartheta_p) = 1/(1 + \tan^2(\vartheta_p))$, $\sin^2(\vartheta_p) = \tan^2(\vartheta_p)/(1 + \tan^2(\vartheta_p))$ and $\cos(\vartheta_p) \sin(\vartheta_p) = \tan(\vartheta_p)/(1 + \tan^2(\vartheta_p))$:

$$\begin{aligned} \epsilon_p^2/4 &= [g - J \cos(p)]^2 \cos^2(\vartheta_p) + [J \sin(p)]^2 \sin^2(\vartheta_p) - 2[g - J \cos(p)][J \sin(p)] \cos(\vartheta_p) \sin(\vartheta_p) \\ &= \frac{[g - J \cos(p)]^2 + [J \sin(p)]^2 \tan^2(\vartheta_p) - 2[g - J \cos(p)][J \sin(p)] \tan(\vartheta_p)}{1 + \tan^2(\vartheta_p)} \\ &= \frac{[g - J \cos(p)]^2 + \frac{[J \sin(p)]^4}{[g - J \cos(p)]^2} + 2[J \sin(p)]^2}{1 + \frac{[J \sin(p)]^2}{[g - J \cos(p)]^2}} \\ &= \frac{[g - J \cos(p)]^4 + [J \sin(p)]^4 + 2[g - J \cos(p)]^2 [J \sin(p)]^2}{[g - J \cos(p)]^2 + [J \sin(p)]^2} \\ &= [g - J \cos(p)]^2 + [J \sin(p)]^2. \end{aligned} \quad (\text{A.30})$$

The final diagonal form of the Hamiltonian reads

$$H = \sum_p \epsilon_p \gamma_p^\dagger \gamma_p + E_0 \quad \text{with } \epsilon_p = 2\sqrt{g^2 - 2Jg \cos(p) + J^2} \quad \text{and } E_0 = -\sum_p \epsilon_p/2. \quad (\text{A.31})$$

Chapter B

Quantum channels and matrix product states

Representations of quantum channels

A state of a quantum system with D different configurations can be described by a *density matrix* $\rho \in \mathbb{C}^{D \times D}$ with $\rho \geq 0$ and $\text{tr}[\rho] = 1$. A linear map $\mathcal{E} : \mathbb{C}^{D \times D} \rightarrow \mathbb{C}^{D \times D}$ is called

- *positive* if $\mathcal{E}(X) \geq 0$ for all $X \geq 0$,
- *completely positive* (CP) if $\mathcal{E} \otimes \text{id}_n$ is positive for all $n \in \mathbb{N}$, where id_n is the identity map on $\mathbb{C}^{n \times n}$ such that $\mathcal{E} \otimes \text{id}_n : X \otimes Y \mapsto \mathcal{E}(X) \otimes Y$,
- *trace preserving* (TP) if $\text{tr}[\mathcal{E}(X)] = \text{tr}[X]$ for all X ,
- *unital* (U) if $\mathcal{E}(\mathbb{1}) = \mathbb{1}$.

A CPTP map is called a *quantum channel*, mapping density matrices to density matrices. It has the following representations:

- *Choi-Jamiolkowski isomorphism*: For the maximally entangled state $|\Omega\rangle = \sum_{\alpha=1}^D |\alpha, \alpha\rangle \in \mathbb{C}^D \otimes \mathbb{C}^D$, the Choi matrix

$$C_{\mathcal{E}} = (\mathcal{E} \otimes \text{id})(|\Omega\rangle\langle\Omega|) \stackrel{\text{CP}}{\geq} 0 \quad \text{with } \text{tr}_1[C_{\mathcal{E}}] \stackrel{\text{TP}}{=} \mathbb{1} \quad (\text{B.1})$$

defines a bijection $\mathcal{E} \mapsto C_{\mathcal{E}}$.

- *Kraus representation*: There exist Kraus operators $\{A^s \in \mathbb{C}^{D \times D}\}_{s=1}^d$ such that

$$\mathcal{E}(X) \stackrel{\text{CP}}{=} \sum_{s=1}^d A^s X A^{s\dagger} \quad \text{with} \quad \sum_{s=1}^d A^{s\dagger} A^s \stackrel{\text{TP}}{=} \mathbb{1}. \quad (\text{B.2})$$

- *Transfer matrix*: Using the isomorphism $|\alpha\rangle\langle\beta| \leftrightarrow |\alpha, \beta\rangle$ between $\mathbb{C}^{D \times D}$ and \mathbb{C}^{D^2} , with the relation

$$(\gamma|\mathcal{E}(|\alpha\rangle\langle\beta|)|\delta) = (\gamma, \delta|T_{\mathcal{E}}|\alpha, \beta), \quad (\text{B.3})$$

we get the matrix representation

$$T_{\mathcal{E}} \stackrel{\text{CP}}{=} \sum_{s=1}^d A^s \otimes \overline{A^s} \quad \text{with} \quad (\mathbb{1}|T_{\mathcal{E}}| \stackrel{\text{TP}}{=} (\mathbb{1}|). \quad (\text{B.4})$$

A linear map \mathcal{E} is CPTP if and only if the corresponding *dual map* \mathcal{E}^* , defined via $\text{tr}[\mathcal{E}(X)Y] = \text{tr}[X\mathcal{E}^*(Y)]$ for all $X, Y \in \mathbb{C}^{D \times D}$, is CPU. It has Kraus representation $\mathcal{E}^*(X) = \sum_s A^{s\dagger} X A^s$ and transfer matrix $T_{\mathcal{E}^*} = T_{\mathcal{E}}^\dagger$. [Wol12, Wol22]

The Kraus operators $\{A^s \in \mathbb{C}^{D \times D}\}_{s=1}^d$ can equivalently be seen as a rank-3 tensor $A \in \mathbb{C}^{d \times D \times D}$, which links quantum channels to uniform MPS. Making analytical proofs more convenient, we define the latter with periodic boundary conditions here. Namely, for d -dimensional spins on a chain of length N [CPGSV21]:

$$|\psi(A, N)\rangle = \sum_{s_1, \dots, s_N=1}^d \text{tr}[A^{s_1} \cdots A^{s_N}] |s_1 \dots s_N\rangle \in \mathbb{C}^{d^N}. \quad (\text{B.5})$$

Primitivity

As for every linear map with equal input and output space, we can assign a *spectrum* to a quantum channel:

$$\begin{aligned} \sigma(\mathcal{E}) &= \{\lambda \in \mathbb{C} \mid \mathcal{E}(X) = \lambda X \text{ for some nonzero } X \in \mathbb{C}^{D \times D}\} \\ &= \{\lambda \in \mathbb{C} \mid T_{\mathcal{E}}|X\rangle = \lambda|X\rangle \text{ for some nonzero } |X\rangle \in \mathbb{C}^{D^2}\}. \end{aligned} \quad (\text{B.6})$$

It is easy to show that the dual map \mathcal{E}^* has the same spectrum, with equal multiplicities for every eigenvalue. The *spectral radius* ρ is defined as the maximum magnitude in the spectrum, equal to 1 for TP maps:

$$\rho(\mathcal{E}) = \max\{|\lambda| \mid \lambda \in \sigma(\mathcal{E})\} \stackrel{\text{TP}}{=} 1. \quad (\text{B.7})$$

An important part of the spectrum in the context of MPS is the *peripheral spectrum*, consisting of all eigenvalues with absolute value equal to the spectral radius:

$$\sigma_p(\mathcal{E}) = \{\lambda \in \sigma(\mathcal{E}) \mid |\lambda| = 1\}. \quad (\text{B.8})$$

It turns out that for quantum channels the peripheral spectrum has trivial Jordan blocks, i.e. equal algebraic and geometric multiplicities. This is very useful for the following two spectral properties [Wol12]:

- *Irreducibility*: The spectral radius one is a nondegenerate eigenvalue with positive definite right eigenvector $r > 0$ (and left eigenvector $\mathbb{1}$). The other eigenvalues of magnitude one turn out to be the other p -th roots of one for some $p \leq D^2$, so that $T_{\mathcal{E}}$ can be written as

$$T_{\mathcal{E}} = |r\rangle\langle\mathbb{1}| + \sum_{j=1}^{p-1} e^{i2\pi j/p} |r_j\rangle\langle l_j| + \mathcal{O}(|\lambda_2|) \text{ with } |\lambda_2| < 1. \quad (\text{B.9})$$

The eigenvectors fulfill the orthonormality conditions

$$(\mathbb{1}|r) = \text{tr}[r] = 1, \quad (\mathbb{1}|r_j) = \text{tr}[r_j] = 0, \quad (l_j|r_k) = \text{tr}[l_j^T r_k] = \delta_{jk}. \quad (\text{B.10})$$

- *Primitivity*: \mathcal{E} is irreducible and has trivial peripheral spectrum, i.e. counting algebraic multiplicities, there is only one eigenvalue of magnitude and value one and the corresponding eigenvector r is positive definite:

$$T_{\mathcal{E}} = |r\rangle\langle\mathbb{1}| + \mathcal{O}(|\lambda_2|) \text{ with } |\lambda_2| < 1. \quad (\text{B.11})$$

In the main text, we defined primitivity for a general, completely positive map with dominant eigenvectors r, l . Here, we always work with the special cases of CPTP or CPU maps. However, this is not a restriction. Trace preservation (left isometric gauge) can be achieved with the similarity transformation $A^s \rightarrow \bar{l}^{1/2} A^s \bar{l}^{-1/2}$, unitality (right isometric gauge) with $A^s \rightarrow r^{-1/2} A^s r^{1/2}$. Both are gauge transformations of the form $A^s \rightarrow S A^s S^{-1}$, leaving the uMPS invariant for any invertible $S \in \mathbb{C}^{D \times D}$.

To get a physical intuition for irreducibility and primitivity, we want to make two examples for $d = 2$ [PGVWC07]:

- Antiferromagnetic GHZ state $|\psi(A)\rangle = |0101\dots\rangle + |1010\dots\rangle$ with

$$A^0 = \begin{pmatrix} 0 & 1 \\ 0 & 0 \end{pmatrix} \in \mathbb{C}^{2 \times 2}, \quad A^1 = \begin{pmatrix} 0 & 0 \\ 1 & 0 \end{pmatrix} \in \mathbb{C}^{2 \times 2}. \quad (\text{B.12})$$

The corresponding quantum channel $\mathcal{E}_A : \mathbb{C}^{2 \times 2} \rightarrow \mathbb{C}^{2 \times 2}$, $X \mapsto \sum_s A^s X A^{s\dagger}$ is irreducible with $p = 2$, since $\mathcal{E}_A^*(\mathbb{1}) = \mathbb{1}$ and $\mathcal{E}_A^*(\sigma^z) = -\sigma^z$ are the only peripheral left eigenvector equations.

- Ferromagnetic product state $|\psi(A)\rangle = |0000\dots\rangle$ with $A^0 = (1) \in \mathbb{C}^{1 \times 1}$, $A^1 = (0) \in \mathbb{C}^{1 \times 1}$. The corresponding quantum channel $\mathcal{E}_A : \mathbb{C} \rightarrow \mathbb{C}$, $x \mapsto A^0 x A^{0\dagger} = x$ is primitive.

In the literature, the terms *primitivity*, *injectivity* and *invertibility* are interchangeably used. Let us order them with the following theorem [FGSW⁺15]:

Theorem B.1: Primitivity, injectivity, invertibility

For a CPTP map \mathcal{E}_A , represented by the rank-3 tensor $A \in \mathbb{C}^{d \times D \times D}$, the following are equivalent:

- (1) \mathcal{E}_A is *primitive*.
- (2) There exists a finite $L_0 \in \mathbb{N}$ such that for all $L \geq L_0$:

$$\text{span}\{A^{s_1} \cdots A^{s_L}\}_{s_1, \dots, s_L} = \mathbb{C}^{D \times D}. \quad (\text{B.13})$$

- (3) For all $L \geq L_0$, the map $\Gamma_{A^L} : \mathbb{C}^{D \times D} \rightarrow \mathbb{C}^{d^L}$, defined by

$$\Gamma_{A^L}(X) = \sum_{s_1, \dots, s_L} \text{tr}[X A^{s_1} \cdots A^{s_L}] |s_1 \dots s_L\rangle, \quad (\text{B.14})$$

is *injective*.

- (4) For all $L \geq L_0$, the blocked tensor A^L is *invertible* with respect to the physical leg, i.e. there exists a tensor $A^{-1} \in \mathbb{C}^{d^L \times D \times D}$ such that

$$\sum_{s_1, \dots, s_L} (A^{s_1} \cdots A^{s_L})_{\alpha, \beta} (A^{-1})_{\gamma, \delta}^{s_1, \dots, s_L} = \delta_{\alpha\gamma} \delta_{\beta\delta}. \quad (\text{B.15})$$

If Γ_{A^L} is injective, Γ_{BA^L} and $\Gamma_{A^L C}$ are injective for any nonzero tensors B, C .

Proof. (1) \Leftrightarrow (2): Theorem B.2 below.

In the following we summarize the indices (s_1, \dots, s_L) in the multi-index $S \in \{0, \dots, d^L - 1\}$.

(2) \Leftrightarrow (3): $\text{span}\{A^S\} = \mathbb{C}^{D \times D} \Leftrightarrow$ for every nonzero $X \in \mathbb{C}^{D \times D}$ there is S such that $\text{tr}[XA^S] \neq 0 \Leftrightarrow \text{tr}[XA^S] = 0$ for all S implies $X = 0 \Leftrightarrow \Gamma_{A^L}(X) = 0$ implies $X = 0 \Leftrightarrow \Gamma_{A^L}$ is injective.

(2) \Rightarrow (4): Let $|a_{\gamma\delta}| \in \mathbb{C}^{d^L}$ be the coefficient vector corresponding to $|\gamma\rangle\langle\delta|$, i.e. $|\gamma\rangle\langle\delta| = \sum_S (S|a_{\gamma\delta}) A^S$. Define $(A^{-1})_{\gamma\delta}^S := (S|a_{\gamma\delta})$ and it follows

$$\sum_S A_{\alpha\beta}^S (A^{-1})_{\gamma\delta}^S = (\alpha| \left[\sum_S (S|a_{\gamma\delta}) A^S \right] |\beta) = (\alpha|\gamma)(\delta|\beta) = \delta_{\alpha\gamma}\delta_{\beta\delta}. \quad (\text{B.16})$$

(4) \Rightarrow (2): For any $X \in \mathbb{C}^{D \times D}$ define $(S|a_X) := \text{tr}[X^T (A^{-1})^S]$. Then

$$\begin{aligned} \sum_S (S|a_X) A^S &= \sum_{\alpha,\beta} \sum_{\gamma,\delta} (\delta| X^T |\gamma) \left[\sum_S (\alpha| A^S |\beta) (\gamma| (A^{-1})^S |\delta) \right] |\alpha\rangle\langle\beta| \\ &= \sum_{\alpha,\beta} (\beta| X^T |\alpha) |\alpha\rangle\langle\beta| = X. \end{aligned} \quad (\text{B.17})$$

Assume that Γ_{A^L} is injective and the tensor $B \in \mathbb{C}^{d_B \times D \times D}$ nonzero. The Γ -function of the product tensor BA^L is given by

$$\Gamma_{BA^L}(X) = \sum_{s,S} \text{tr}[XB^s A^S] |s, S\rangle = \sum_s |s\rangle \otimes \Gamma_{A^L}(XB^s). \quad (\text{B.18})$$

It holds: $\Gamma_{BA^L}(X) = 0 \Leftrightarrow \Gamma_{A^L}(XB^s) = 0$ for all $s \Leftrightarrow XB^s = 0$ for all $s \Leftrightarrow X = 0$, where we used injectivity of Γ_{A^L} for the second equivalence. Consequently Γ_{BA^L} is also injective. The proof for $\Gamma_{A^L C}$ with nonzero $C \in \mathbb{C}^{d_C \times D \times D}$ works the same way. \square

We still owe the proof for (1) \Leftrightarrow (2), which we provide with an extra theorem [Wol12]:

Theorem B.2: Primitive CPTP maps

Let $\mathcal{E} : \mathbb{C}^{D \times D} \rightarrow \mathbb{C}^{D \times D}$ be a completely positive trace preserving map with Kraus representation $\mathcal{E}(X) = \sum_{s=1}^d A^s X A^{s\dagger}$ and Choi matrix $C_{\mathcal{E}} = (\mathcal{E} \otimes \text{id})(|\Omega\rangle\langle\Omega|)$ such that $d \geq \text{rank}(C_{\mathcal{E}})$. The following properties are equivalent:

(1) Primitivity: There exists a positive definite $r \in \mathbb{C}^{D \times D}$ with unit trace such that

$$T_{\mathcal{E}} = |r\rangle\langle r| + \mathcal{O}(|\lambda_2|) \text{ with } |\lambda_2| < 1. \quad (\text{B.19})$$

(2) Eventual strict positivity: There exists a minimal $M_0 \in \mathbb{N}$ such that for all $M \geq M_0$ and nonzero positive semidefinite $X \in \mathbb{C}^{D \times D}$:

$$\mathcal{E}^M(X) > 0. \quad (\text{B.20})$$

(3) Eventual full Kraus rank: There exists a minimal $L_0 \in \mathbb{N}$ such that for all $L \geq L_0$:

$$\text{rank}(C_{\mathcal{E}^L}) = D^2. \quad (\text{B.21})$$

(4) There exists a minimal $L_0 \in \mathbb{N}$ such that for all $L \geq L_0$:

$$\text{span}\{A^{s_1} \cdots A^{s_L}\} = \mathbb{C}^{D \times D}. \quad (\text{B.22})$$

The L_0 s in (3) and (4) are the same. Moreover, $M_0 \leq L_0$.

Proof. We prove $(1) \Rightarrow (3) \Rightarrow (2) \Rightarrow (1)$ and $(3) \Leftrightarrow (4)$.

$(1) \Rightarrow (3)$: Primitivity implies $\lim_{L \rightarrow \infty} \mathcal{E}^L(X) =: \mathcal{E}^\infty(X) = r \text{tr}[X]$ and thus the following convergence for the Choi matrix:

$$\lim_{L \rightarrow \infty} C_{\mathcal{E}^L} = (\mathcal{E}^\infty \otimes \text{id})(|\Omega\rangle\langle\Omega|) = r \otimes \mathbb{1}, \quad (\text{B.23})$$

with $r > 0$. If $C_{\mathcal{E}^L}$ had a kernel for all L , with eigenvector $|\psi_L\rangle$, we could derive the following bound for the minimal eigenvalue of r :

$$\begin{aligned} \lambda_{\min}(r) &\leq |\langle \bar{\psi}_L | C_{\mathcal{E}^L} - r \otimes \mathbb{1} | \psi_L \rangle| \leq \|C_{\mathcal{E}^L} - r \otimes \mathbb{1}\| = \|[(\mathcal{E}^L - \mathcal{E}^\infty) \otimes \text{id}](|\Omega\rangle\langle\Omega| - r \otimes \mathbb{1})\| \\ &\leq \mu^L c \| |\Omega\rangle\langle\Omega| - r \otimes \mathbb{1} \|, \end{aligned} \quad (\text{B.24})$$

where $\|\cdot\|$ is the operator norm, $|\lambda_2| < \mu < 1$ and $c > 0$. So for sufficiently large L the bound contradicted $r > 0$. As a consequence, there has to be a finite $L_0 \in \mathbb{N}$ such that for all $L \geq L_0$: $C_{\mathcal{E}^L} > 0$, implying $\text{rank}(C_{\mathcal{E}^L}) = D^2$.

$(3) \Rightarrow (2)$: For $|\psi\rangle, |\varphi\rangle \in \mathbb{C}^D$ and $X \in \mathbb{C}^{D \times D}$ the following implications hold:

$$\begin{aligned} C_{\mathcal{E}^{L_0}} > 0 &\Rightarrow \langle \bar{\varphi}, \psi | C_{\mathcal{E}^{L_0}} | \varphi, \bar{\psi} \rangle > 0 \text{ for all nonzero } |\psi\rangle, |\varphi\rangle \\ &\Rightarrow \langle \bar{\varphi} | \mathcal{E}^{L_0}(|\psi\rangle\langle\bar{\psi}|) | \varphi \rangle > 0 \text{ for all nonzero } |\psi\rangle, |\varphi\rangle \\ &\Rightarrow \mathcal{E}^{L_0}(|\psi\rangle\langle\bar{\psi}|) > 0 \text{ for all nonzero } |\psi\rangle \\ &\Rightarrow \mathcal{E}^{L_0}(X) > 0 \text{ for all nonzero } X \geq 0. \end{aligned} \quad (\text{B.25})$$

From the first to the second line we used

$$\begin{aligned} \langle \bar{\varphi}, \psi | C_{\mathcal{E}^{L_0}} | \varphi, \bar{\psi} \rangle &= \langle \bar{\varphi}, \psi | (\mathcal{E}^{L_0} \otimes \text{id})(|\Omega\rangle\langle\Omega|) | \varphi, \bar{\psi} \rangle = \sum_{\alpha, \beta} \langle \bar{\varphi} | \mathcal{E}^{L_0}(|\alpha\rangle\langle\beta|) | \varphi \rangle (\psi | \alpha)(\beta | \bar{\psi}) \\ &= \langle \bar{\varphi} | \mathcal{E}^{L_0}(|\psi\rangle\langle\bar{\psi}|) | \varphi \rangle. \end{aligned} \quad (\text{B.26})$$

This also shows that $M_0 \leq L_0$. For $M \geq M_0$, $\mathcal{E}^{M-M_0}(X)$ is nonzero and positive semidefinite if X is so, since \mathcal{E} is trace preserving and positive. As a consequence $\mathcal{E}^M(X) = \mathcal{E}^{M_0}(\mathcal{E}^{M-M_0}(X)) > 0$ if $\mathcal{E}^{M_0}(X) > 0$.

$(2) \Rightarrow (1)$: We show that if \mathcal{E} is not primitive, there is a nonzero $X \geq 0$ such that $\mathcal{E}^n(X)$ is not full rank for all $n \in \mathbb{N}$. Denote by r a positive semidefinite fixed point, which always exists for a positive TP map. Then primitivity can be violated in the following three ways:

(i) r is not full rank $\Rightarrow \mathcal{E}^n(r) = r$ is not full rank for all $n \in \mathbb{N}$.

- (ii) There is another eigenvector \tilde{r} corresponding to the eigenvalue 1, which can be taken Hermitian since \mathcal{E} is positive $\Rightarrow \lambda_{\max}r - \tilde{r}$ with $\lambda_{\max} := \max \sigma(r^{-1/2}\tilde{r}r^{-1/2})$ is a positive semidefinite fixed point that does not have full rank \Rightarrow (i) for $\lambda_{\max}r - \tilde{r}$.
- (iii) There is another eigenvalue $\tilde{\lambda}$ with modulus 1, which has to be another p -th root of unity for some $p \leq D^2 \Rightarrow$ (ii) for \mathcal{E}^p .

(3) \Leftrightarrow (4): For $|\psi\rangle \in \mathbb{C}^D \otimes \mathbb{C}^D$, $X \in \mathbb{C}^{D \times D}$ and the multi-index $S = (s_1, \dots, s_{L_0})$ the following equivalences hold:

$$\begin{aligned}
\text{rank}(C_{\mathcal{E}^{L_0}}) = D^2 &\Leftrightarrow C_{\mathcal{E}^{L_0}} > 0 \Leftrightarrow (\bar{\psi}| C_{\mathcal{E}^{L_0}} |\psi) > 0 \text{ for all nonzero } |\psi\rangle \\
&\Leftrightarrow \sum_S |(\bar{\psi}| A^S \otimes \mathbb{1} |\Omega\rangle)|^2 > 0 \text{ for all nonzero } |\psi\rangle \\
&\Leftrightarrow \text{for every nonzero } |\psi\rangle \text{ there is } S \text{ such that } (\bar{\psi}| A^S \otimes \mathbb{1} |\Omega\rangle) \neq 0 \\
\text{span}\{A^S\} = \mathbb{C}^{D \times D} &\Leftrightarrow \text{for every nonzero } X \text{ there is } S \text{ such that } \text{tr}[X^\dagger A^S] \neq 0
\end{aligned} \tag{B.27}$$

For $C_{\mathcal{E}^{L_0}} > 0$ there is a constant $c > 0$ so that $C_{\mathcal{E}^{L_0}} \geq cC_{\mathcal{E}^{L_0-1}} \geq 0$. It follows for $L_0 + 1$ and by induction for all integers larger than L_0 : $C_{\mathcal{E}^{L_0+1}} = (\mathcal{E} \otimes \mathbb{1})(C_{\mathcal{E}^{L_0}}) \geq c(\mathcal{E} \otimes \mathbb{1})(C_{\mathcal{E}^{L_0-1}}) = cC_{\mathcal{E}^{L_0}} > 0$. \square

From theorem B.1 we can make the following important conclusion about the genericness of primitive tensors: For d randomly drawn matrices $\{A^s\}_{s=1}^d$, the dimension of $\text{span}\{A^{s_1} \cdots A^{s_L}\}$ is expected to grow as d^L until it reaches D^2 . Therefore, a generic rank-3 tensor is expected to be primitive with $L_0 \sim 2 \ln D / \ln d$, whereas non-primitive tensors appear with measure zero in the space $\mathbb{C}^{D \times d \times D}$. [PGVWC07]

Fundamental theorem

In general, it can be proven that $|\psi(A, N)\rangle = |\psi(B, N)\rangle$ if and only if $B^s = SA^sS^{-1}$ with $S \in \mathbb{C}^{D \times D}$ invertible. Here, we prove this under the assumption of primitivity and unitality, which requires S to be unitary [CPGSV17]:

Theorem B.3: Fundamental theorem

For tensors $A \in \mathbb{C}^{d \times D_A \times D_A}$ and $B \in \mathbb{C}^{d \times D_B \times D_B}$ with corresponding primitive CPU maps \mathcal{E}_A and \mathcal{E}_B , the following are equivalent (for some phases $\alpha, \beta \in \mathbb{C}$):

- (1) $|\psi(B, N)\rangle = e^{i\alpha} |\psi(A, N)\rangle$,
- (2) $D_A = D_B =: D$ and there exists unitary $U \in \mathbb{C}^{D \times D}$ such that
 - $\mathcal{E}_{AB}(U) = e^{i\beta} U$ with 1 the spectral radius,
 - $B^s = e^{-i\beta} U^\dagger A^s U$ for all s .

Proof. (2) \Rightarrow (1): Trivial insertion of the MPS definition and use of the trace cyclicity:

$$\begin{aligned}
|\psi(B, N)\rangle &= \sum_{s_1, \dots, s_N} \text{tr}[B^{s_1} \cdots B^{s_N}] |s_1 \dots s_N\rangle \\
&= e^{-i\beta N} \sum_{s_1, \dots, s_N} \text{tr}[U^\dagger A^{s_1} U \cdots U^\dagger A^{s_N} U] |s_1 \dots s_N\rangle \\
&= e^{-i\beta N} \sum_{s_1, \dots, s_N} \text{tr}[A^{s_1} \cdots A^{s_N}] |s_1 \dots s_N\rangle \\
&= e^{-i\beta N} |\psi(A, N)\rangle.
\end{aligned} \tag{B.28}$$

(1) \Rightarrow (2): $T_A = \sum_s A^s \otimes \overline{A^s}$ is the transfer matrix of $\mathcal{E}_A : X \mapsto \sum_s A^s X A^{s\dagger}$ in the basis of matrix units. In the same manner we define the mixed transfer matrix $T_{AB} := \sum_s A^s \otimes \overline{B^s}$ of $\mathcal{E}_{AB} : X \mapsto \sum_s A^s X B^{s\dagger}$. We first show that $|\psi(B, N)\rangle = e^{i\alpha} |\psi(A, N)\rangle$ implies spectral radius 1 for \mathcal{E}_{AB} . Inserting the MPS definition and using trace properties we have

$$\begin{aligned}
\langle \psi(A, N) | \psi(A, N) \rangle &= \sum_{s_1, \dots, s_N} \text{tr}[A^{s_1} \cdots A^{s_N}] \overline{\text{tr}[A^{s_1} \cdots A^{s_N}]} \\
&= \sum_{s_1, \dots, s_N} \text{tr}[A^{s_1} \cdots A^{s_N} \otimes \overline{A^{s_1}} \cdots \overline{A^{s_N}}] \\
&= \text{tr}[T_A^N].
\end{aligned} \tag{B.29}$$

As \mathcal{E}_A is CPU primitive, we can write $T_A = |\mathbb{1}\rangle (l_A| + \mathcal{O}(|\lambda_2|))$ with $|\lambda_2| < 1$ the second largest eigenvalue magnitude. So $\langle \psi(A, N) | \psi(A, N) \rangle = \text{tr}[T_A^N]$ equals $(l_A|\mathbb{1}\rangle) = \text{tr}[l_A] = 1$ up to a correction exponentially small in N . In the same manner we compute the mixed overlap

$$\begin{aligned}
\langle \psi(B, N) | \psi(A, N) \rangle &= \sum_{s_1, \dots, s_N} \text{tr}[A^{s_1} \cdots A^{s_N}] \overline{\text{tr}[B^{s_1} \cdots B^{s_N}]} \\
&= \sum_{s_1, \dots, s_N} \text{tr}[A^{s_1} \cdots A^{s_N} \otimes \overline{B^{s_1}} \cdots \overline{B^{s_N}}] \\
&= \text{tr}[T_{AB}^N].
\end{aligned} \tag{B.30}$$

Taken together, $|\psi(B, N)\rangle = e^{i\alpha} |\psi(A, N)\rangle$ and $\lim_{N \rightarrow \infty} \langle \psi(A, N) | \psi(A, N) \rangle = 1$ imply

$$\lim_{N \rightarrow \infty} |\langle \psi(B, N) | \psi(A, N) \rangle| = 1 = \lim_{N \rightarrow \infty} |\text{tr}[T_{AB}^N]|. \quad (\text{B.31})$$

So \mathcal{E}_{AB} has spectral radius 1. Next we show that $\mathcal{E}_{AB}(X) = e^{i\beta} X$ for some X implies $X =: U$ is unitary and $B^s = e^{-i\beta} U^\dagger A^s U$ for all s . For this consider the general eigenvalue equation for $X \in \mathbb{C}^{D_A \times D_B}$.

$$\mathcal{E}_{AB}(X) = \sum_s A^s X B^{s\dagger} = \lambda X. \quad (\text{B.32})$$

Denoting by $l_B = \sqrt{l_B} \sqrt{l_B}$ the positive definite left leading eigenvector of T_B , we derive the upper bound

$$\begin{aligned} |\lambda| |\text{tr}[X l_B X^\dagger]| &= \left| \sum_s \text{tr}\left[(X B^{s\dagger} \sqrt{l_B})(\sqrt{l_B} X^\dagger A^s) \right] \right| \\ &\leq \left(\sum_k \text{tr}\left[X B^{s\dagger} \sqrt{l_B} \sqrt{l_B} B^s X^\dagger \right] \right)^{1/2} \left(\sum_k \text{tr}\left[\sqrt{l_B} X^\dagger A^s A^{s\dagger} X \sqrt{l_B} \right] \right)^{1/2} \\ &= |\text{tr}[X l_B X^\dagger]|, \end{aligned} \quad (\text{B.33})$$

where we inserted (B.32) for the first equality and used $\mathcal{E}_A(\mathbb{1}) = \sum_s A^s A^{s\dagger} = \mathbb{1}$, $\mathcal{E}_B^*(l_B) = \sum_s B^{s\dagger} l_B B^s = l_B$, $\text{tr}[X l_B X^\dagger] > 0$ for the last equality. The inequality results from the following two applications of Cauchy-Schwarz:

$$\begin{aligned} \left| \sum_s \text{tr}[X^s Y^s] \right| &\leq \sum_s |\text{tr}[X^s Y^s]| \stackrel{\text{CS}}{\leq} \sum_s \text{tr}[X^{s\dagger} X^s]^{1/2} \text{tr}[Y^{s\dagger} Y^s]^{1/2} \\ &\stackrel{\text{CS}}{\leq} \left(\sum_s \text{tr}[X^{s\dagger} X^s] \right)^{1/2} \left(\sum_s \text{tr}[Y^{s\dagger} Y^s] \right)^{1/2}. \end{aligned} \quad (\text{B.34})$$

So $|\lambda| \leq 1$. For $|\lambda| = 1$, Cauchy-Schwarz is fulfilled with an equal sign, implying proportionality $\sqrt{l_B} B^s X^\dagger = \mu \sqrt{l_B} X^\dagger A^s$. Since l_B is nonsingular, this is equivalent to

$$B^s X^\dagger = \mu X^\dagger A^s. \quad (\text{B.35})$$

From

$$\bar{\mu} X = \bar{\mu} \sum_s A^s A^{s\dagger} X = \stackrel{(\text{B.35})}{=} \sum_s A^s X B^{s\dagger} \stackrel{(\text{B.32})}{=} \lambda X \quad (\text{B.36})$$

we get $\lambda = \bar{\mu} =: e^{i\beta}$, and from

$$\mathcal{E}_B(X^\dagger X) = \sum_s B^s X^\dagger X B^{s\dagger} \stackrel{(\text{B.35})}{=} |\mu|^2 X^\dagger \left(\sum_s A^s A^{s\dagger} \right) X = X^\dagger X \quad (\text{B.37})$$

we get $X^\dagger X = \mathbb{1}$ and $D_A \geq D_B$ (since \mathcal{E}_B is CPU primitive). Moreover,

$$\mathcal{E}_A^*(X l_B X^\dagger) = \sum_s A^{s\dagger} X l_B X^\dagger A^s \stackrel{(\text{B.35})}{=} X \left(\sum_s B^{s\dagger} l_B B^s \right) X^\dagger = X l_B X^\dagger. \quad (\text{B.38})$$

So $X l_B X^\dagger$ is a fixed point of \mathcal{E}_A^* which is not full rank if $D_A > D_B$, contradicting primitivity of \mathcal{E}_A^* . Consequently, $D_A = D_B =: D$ and $X =: U$ is unitary. \square

Parent Hamiltonian

In the final chapter of this appendix, we want to find a local Hamiltonian for which the uMPS $|\psi(A, N)\rangle$ is the exact unique ground state, if it is generated by an invertible tensor A .

For d -dimensional spins, let $h = h^\dagger \in \mathbb{C}^{d^L \times d^L}$ be an interaction with interaction length L . The corresponding translational invariant Hamiltonian on N sites is defined as

$$H = \sum_{n=1}^N h_n \text{ with } h_n = \mathbb{1}_{\{1, \dots, n-1\}} \otimes h_{\{n, \dots, n+L-1\}} \otimes \mathbb{1}_{\{n+L, \dots, N\}}, \quad N+1 \equiv 1. \quad (\text{B.39})$$

We call $h \geq 0$ *parent interaction* if there is a rank-3 tensor $A \in \mathbb{C}^{d \times D \times D}$ such that

$$\ker(h) = \mathcal{G}_{AL} = \text{ran}(\Gamma_{AL}) = \left\{ \sum_{s_1, \dots, s_L} \text{tr}[XA^{s_1} \dots A^{s_L}] |s_1 \dots s_L\rangle \middle| X \in \mathbb{C}^{D \times D} \right\}. \quad (\text{B.40})$$

The corresponding Hamiltonian H is called *parent Hamiltonian*. Since the dimension of \mathcal{G}_{AL} is at most D^2 , the parent Hamiltonian will necessarily be nontrivial as soon as $d^L > D^2$. [CPGSV21]

Theorem B.4: Frustration freeness

The parent Hamiltonian is *frustration free*, in the sense that its ground space minimizes the energy locally:

$$\ker(H) = \bigcap_{n=1}^N \ker(h_n). \quad (\text{B.41})$$

Proof. The Hamiltonian reads $H = \sum_{n=1}^N h_n$ with $h_n \geq 0$, $\ker(h_n) = \mathbb{C}^{d^{n-1}} \otimes \mathcal{G}_{AL} \otimes \mathbb{C}^{d^{N-L-n+1}}$. It is easy to check that $|\psi(A, N)\rangle \in \ker(h_n)$ for all n :

$$|\psi(A, N)\rangle = \sum_{s_1, \dots, s_{n-1}} \sum_{s_{n+L}, \dots, s_N} |s_1 \dots s_{n-1}\rangle \otimes \underbrace{\Gamma_{AL}(A^{s_{n+L}} \dots A^{s_N} A^{s_1} \dots A^{s_{n-1}})}_{\in \mathcal{G}_{AL}} \otimes |s_{n+L} \dots s_N\rangle.$$

This trivially implies $H|\psi(A, N)\rangle = 0$. Since $\langle \varphi | H | \varphi \rangle = \sum_n \langle \varphi | h_n | \varphi \rangle \geq 0$ for all $|\varphi\rangle \in \mathbb{C}^{d^N}$, $|\psi(A, N)\rangle$ is a ground state of H . The whole ground space is given by $\ker(H)$ and the following inclusions hold:

$$\ker(H) \supseteq \bigcap_{n=1}^N \ker(h_n) \supseteq \{\alpha |\psi(A, N)\rangle \mid \alpha \in \mathbb{C}\}. \quad (\text{B.42})$$

To show inclusion in the other direction, first note that for $H \geq 0$, $H|\varphi\rangle = 0$ iff $\langle \varphi | H | \varphi \rangle = 0$ [Tas20]:

$$H|\varphi\rangle = 0 \iff \sqrt{H}|\varphi\rangle = 0 \iff \|\sqrt{H}\varphi\| = 0 \iff \langle \sqrt{H}\varphi, \sqrt{H}\varphi \rangle = \langle \varphi | H | \varphi \rangle = 0. \quad (\text{B.43})$$

Now, with $\langle \varphi | h_n | \varphi \rangle \geq 0$ for all n , $\langle \varphi | H | \varphi \rangle = \sum_n \langle \varphi | h_n | \varphi \rangle = 0$ implies $\langle \varphi | h_n | \varphi \rangle = 0$ and thus $h_n|\varphi\rangle = 0$ for all n . So

$$\ker(H) \subseteq \bigcap_{n=1}^N \ker(h_n). \quad (\text{B.44})$$

□

Theorem B.5: Intersection property

Let $B \in \mathbb{C}^{d_B \times D \times D}$ be invertible, $A \in \mathbb{C}^{d_A \times D \times D}$, $C \in \mathbb{C}^{d_C \times D \times D}$. Then

$$(\mathcal{G}_{AB} \otimes \mathbb{C}^{d_C}) \cap (\mathbb{C}^{d_A} \otimes \mathcal{G}_{BC}) = \mathcal{G}_{ABC}. \quad (\text{B.45})$$

$$\left\{ \begin{array}{c} \text{Diagram: } A \xrightarrow{\quad} B \xrightarrow{\quad} C \\ \text{Input: } Y \\ \text{Output: } Z \end{array} \middle| Y \in \mathbb{C}^{d_C \times D \times D} \right\} \cap \left\{ \begin{array}{c} \text{Diagram: } Z \xrightarrow{\quad} B \xrightarrow{\quad} C \\ \text{Input: } Z \\ \text{Output: } X \end{array} \middle| Z \in \mathbb{C}^{d_A \times D \times D} \right\}$$

$$= \left\{ \begin{array}{c} \text{Diagram: } A \xrightarrow{\quad} B \xrightarrow{\quad} C \\ \text{Input: } X \\ \text{Output: } Y \end{array} \middle| X \in \mathbb{C}^{D \times D} \right\}.$$

Proof. Diagrammatic. [CPGSV21]

$$\begin{array}{c} \text{Diagram: } A \xrightarrow{\quad} B \xrightarrow{\quad} C \\ \text{Input: } Y \\ \text{Output: } Z \end{array} = \begin{array}{c} \text{Diagram: } B \xrightarrow{\quad} C \\ \text{Input: } Z \\ \text{Output: } Z \end{array} \quad (\text{B.46})$$

$$\text{Invert } B \quad \begin{array}{c} \text{Diagram: } A \xrightarrow{\quad} C \\ \text{Input: } Y \\ \text{Output: } Z \end{array} = \begin{array}{c} \text{Diagram: } C \\ \text{Input: } Z \\ \text{Output: } Z \end{array} \quad (\text{B.47})$$

$$\text{Re-attach } B \quad \begin{array}{c} \text{Diagram: } A \xrightarrow{\quad} B \xrightarrow{\quad} C \\ \text{Input: } Y \\ \text{Output: } Z \end{array} = \begin{array}{c} \text{Diagram: } B \xrightarrow{\quad} C \\ \text{Input: } Z \\ \text{Output: } Z \end{array} \quad (\text{B.48})$$

$$\text{Invert } (AB) \quad \begin{array}{c} \text{Diagram: } (AB)^{-1} \\ \text{Input: } Y \\ \text{Output: } Z \end{array} = \begin{array}{c} \text{Diagram: } (AB)^{-1} \\ \text{Input: } Z \\ \text{Output: } Z \end{array} \quad (\text{B.49})$$

$$\text{Contract} \quad \begin{array}{c} \text{Diagram: } C \\ \text{Input: } Y \\ \text{Output: } X \end{array} = \begin{array}{c} \text{Diagram: } C \\ \text{Input: } X \\ \text{Output: } X \end{array} \quad (\text{B.50})$$

□

Theorem B.6: Closure property

Let $A \in \mathbb{C}^{d_A \times D \times D}$ and $B \in \mathbb{C}^{d_B \times D \times D}$ be both invertible. Then

$$\begin{aligned} & \left\{ \sum_{s,k} \text{tr}[XA^sB^k] |s,k\rangle \mid X \in \mathbb{C}^{D \times D} \right\} \cap \left\{ \sum_{s,k} \text{tr}[A^sYB^k] |s,k\rangle \mid Y \in \mathbb{C}^{D \times D} \right\} \\ &= \text{span} \left\{ \sum_{s,k} \text{tr}[A^sB^k] |s,k\rangle \right\}. \end{aligned} \quad (\text{B.51})$$

$$\begin{aligned} & \left\{ \begin{array}{c} \text{Diagram: } A \text{ and } B \text{ stacked horizontally, } X \text{ below them.} \\ \text{Condition: } X \in \mathbb{C}^{D \times D} \end{array} \right\} \cap \left\{ \begin{array}{c} \text{Diagram: } A \text{ and } Y \text{ stacked horizontally, } B \text{ below them.} \\ \text{Condition: } Y \in \mathbb{C}^{D \times D} \end{array} \right\} \\ &= \left\{ \alpha \cdot \begin{array}{c} \text{Diagram: } A \text{ and } B \text{ stacked horizontally.} \\ \text{Condition: } \alpha \in \mathbb{C} \end{array} \right\}. \end{aligned}$$

Proof. Diagrammatic. [SCPG10]

$$\begin{array}{c} \text{Diagram: } A \text{ and } B \text{ stacked horizontally, } X \text{ below them.} \\ = \end{array} \quad \begin{array}{c} \text{Diagram: } A \text{ and } Y \text{ stacked horizontally, } B \text{ below them.} \end{array} \quad (\text{B.52})$$

$$\begin{array}{c} \text{Invert } A, B \\ \text{Diagram: } X \end{array} = \begin{array}{c} \text{Diagram: } Y \end{array} \quad (\text{B.53})$$

$$\begin{array}{c} \text{Contract} \\ \text{Diagram: } X \end{array} = \frac{1}{D} \frac{\text{tr}[Y]}{} \quad (\text{B.54})$$

□

Theorem B.7: Unique ground state

Let $A \in \mathbb{C}^{d_A \times D \times D}$ be an invertible tensor with injectivity length L_0 . For $L \geq L_0 + 1$ and $N \geq L + L_0$, $|\psi(A, N)\rangle$ is the unique ground state of the corresponding parent Hamiltonian:

$$\ker(H) = \text{span} \{ |\psi(A, N)\rangle \}. \quad (\text{B.55})$$

Proof. By theorem B.4 the ground space of the parent Hamiltonian is given by

$$\ker(H) = \bigcap_{n=1}^N \ker(h_n) \text{ with } \ker(h_n) = \mathbb{C}^{d^{n-1}} \otimes \mathcal{G}_{A^L} \otimes \mathbb{C}^{d^{N-L-n+1}}. \quad (\text{B.56})$$

We split the Hamiltonian into two sums defined by

$$H_{\text{left}} := h_1 + \dots + h_{L-1} + \frac{1}{2}(h_L + \dots + h_{N-L+1}), \quad (\text{B.57})$$

$$H_{\text{right}} := \frac{1}{2}(h_L + \dots + h_{N-L+1}) + h_{N-L+2} + \dots + h_N. \quad (\text{B.58})$$

$N - L$ applications of the intersection property B.5 yield:

$$\begin{aligned} \ker(H_{\text{left}}) &= \underbrace{(\mathcal{G}_{AA^{L-1}} \otimes \mathbb{C}^d \otimes \mathbb{C}^{d^{N-L-1}}) \cap (\mathbb{C}^d \otimes \mathcal{G}_{A^{L-1}A} \otimes \mathbb{C}^{d^{N-L-1}})}_{=\mathcal{G}_{A^2 A^{L-1}} \otimes \mathbb{C}^d \otimes \mathbb{C}^{d^{N-L-2}}} \cap (\mathbb{C}^{d^2} \otimes \mathcal{G}_{A^{L-1}A} \otimes \mathbb{C}^{d^{N-L-2}}) \cap \dots \\ &\quad \underbrace{\vdots}_{=\mathcal{G}_{AN}} \\ &= \mathcal{G}_{A^3 A^{L-1}} \otimes \mathbb{C}^d \otimes \mathbb{C}^{d^{N-L-3}} \end{aligned}$$

We do the same for H_{right} to get

$$\ker(H_{\text{left}}) = \left\{ \sum_{s_1, \dots, s_N} \text{tr}[XA^{s_1} \dots A^{s_N}] |s_1 \dots s_N\rangle \middle| X \in \mathbb{C}^{D \times D} \right\}, \quad (\text{B.59})$$

$$\ker(H_{\text{right}}) = \left\{ \sum_{s_1, \dots, s_N} \text{tr}[A^{s_1} \dots A^{s_{L-1}} Y A^{s_L} \dots A^{s_N}] |s_1 \dots s_N\rangle \middle| Y \in \mathbb{C}^{D \times D} \right\}. \quad (\text{B.60})$$

After one application of the closure property B.6 we end up with

$$\begin{aligned} \ker(H) &= \ker(H_{\text{left}}) \cap \ker(H_{\text{right}}) \\ &= \text{span} \left\{ \sum_{s_1, \dots, s_N} \text{tr}[A^{s_1} \dots A^{s_N}] |s_1 \dots s_N\rangle \right\} = \text{span} \{|\psi(A, N)\rangle\}. \end{aligned} \quad (\text{B.61})$$

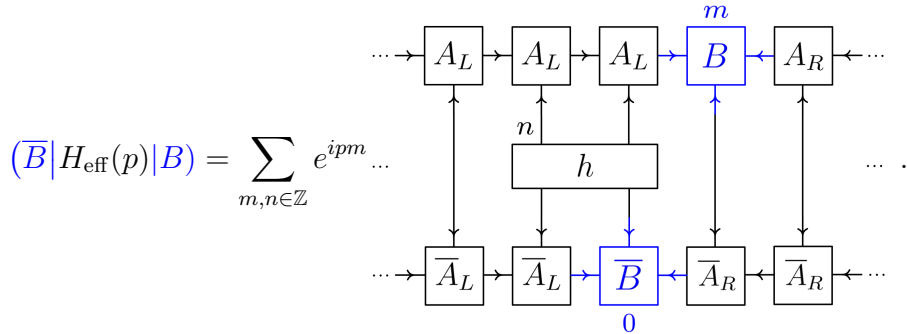
In addition it can be proven that the parent Hamiltonian has a finite energy gap $\Delta > 0$ above the ground state. [PGVWC07, SCPG10] \square

Chapter C

Extensive tensor network diagrams

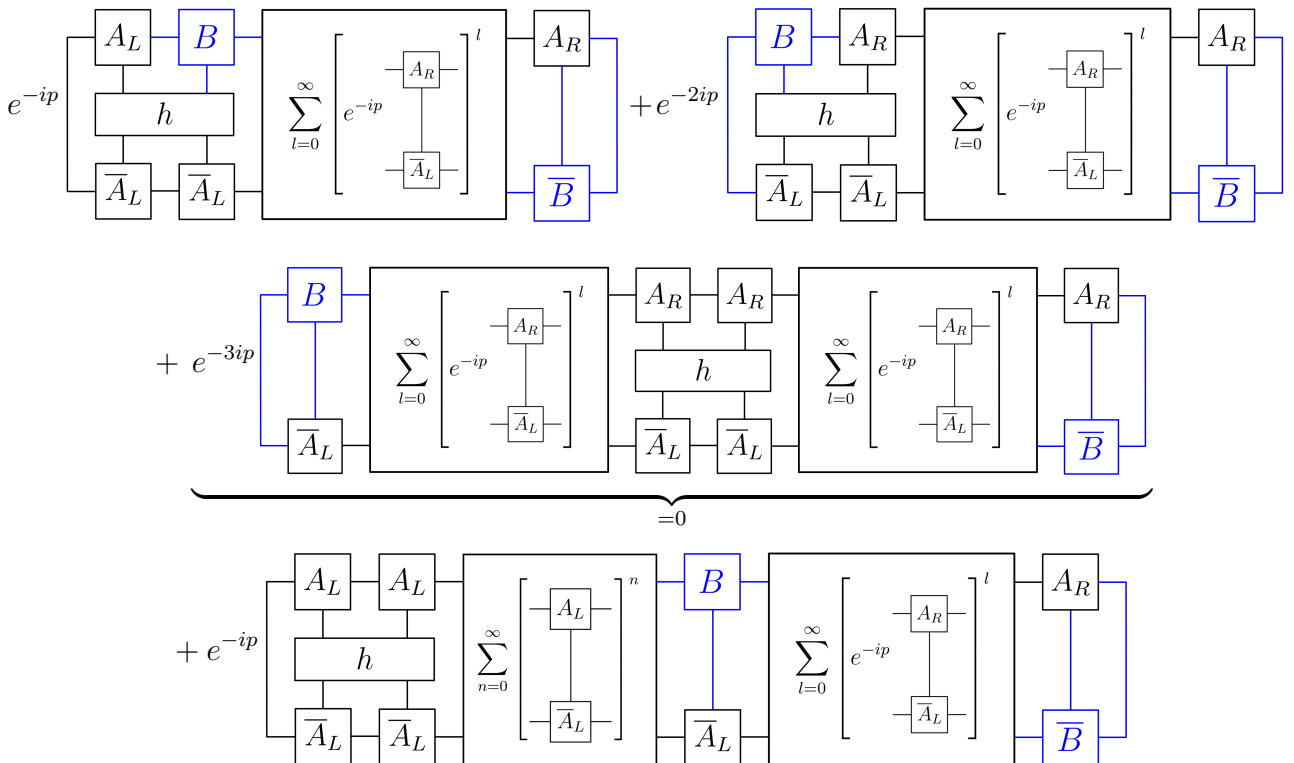
Effective Hamiltonian for uMPS plane wave excitations

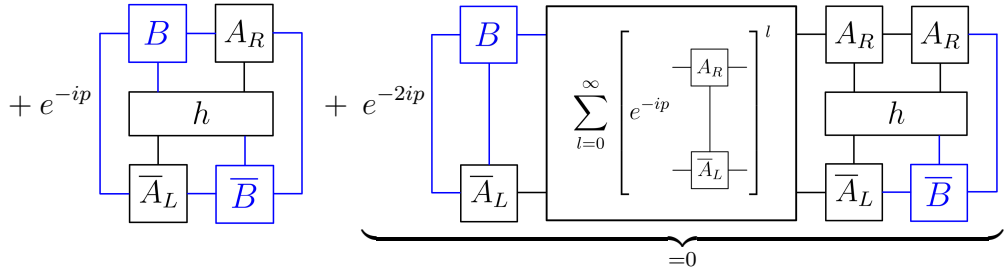
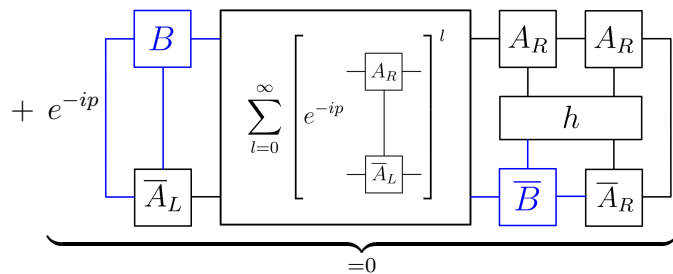
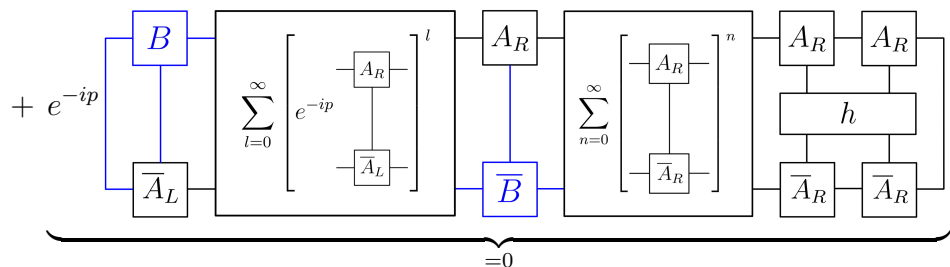
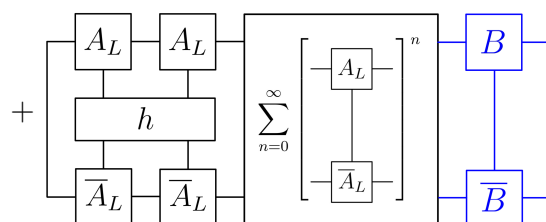
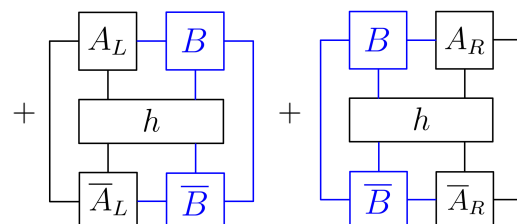
In the actual *matvec* implementation of $H_{\text{eff}}(p)$ (4.67), we compute $B = V_L X$, then $|\tilde{B}\rangle = H_{\text{eff}}(p) |B\rangle$, and in the end we transform back to $\tilde{X} = \overline{V_L} \tilde{B}$. In the following we draw all tensor diagrams appearing in the expectation value

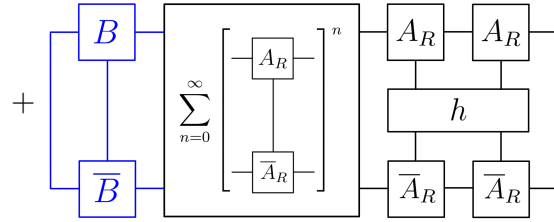
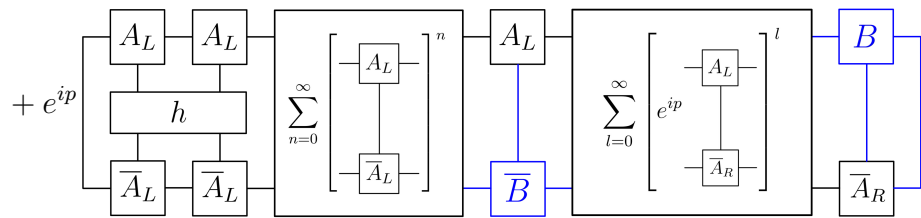
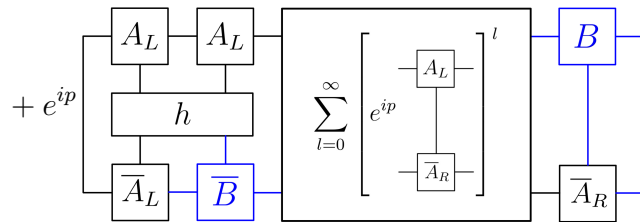
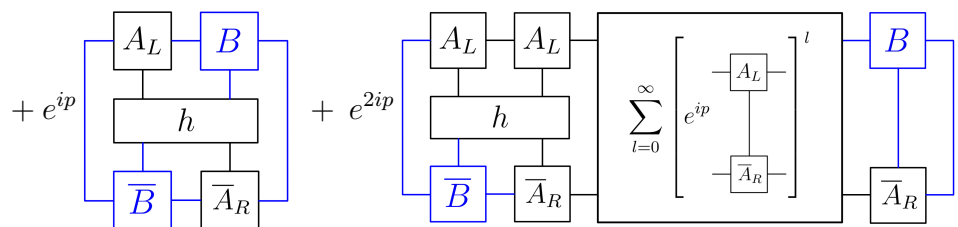
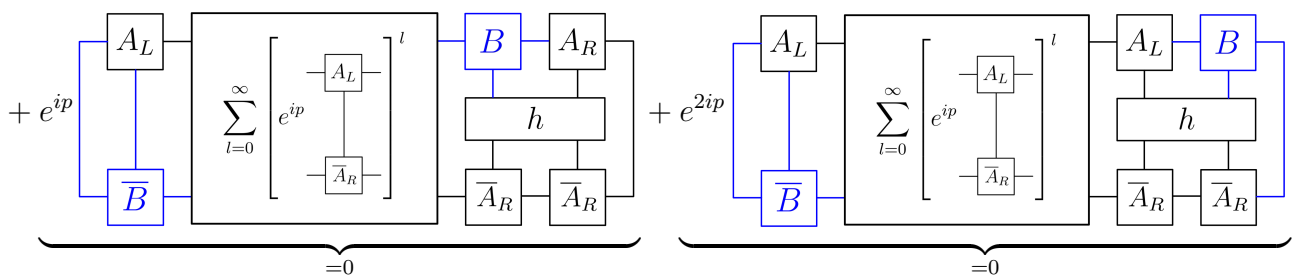


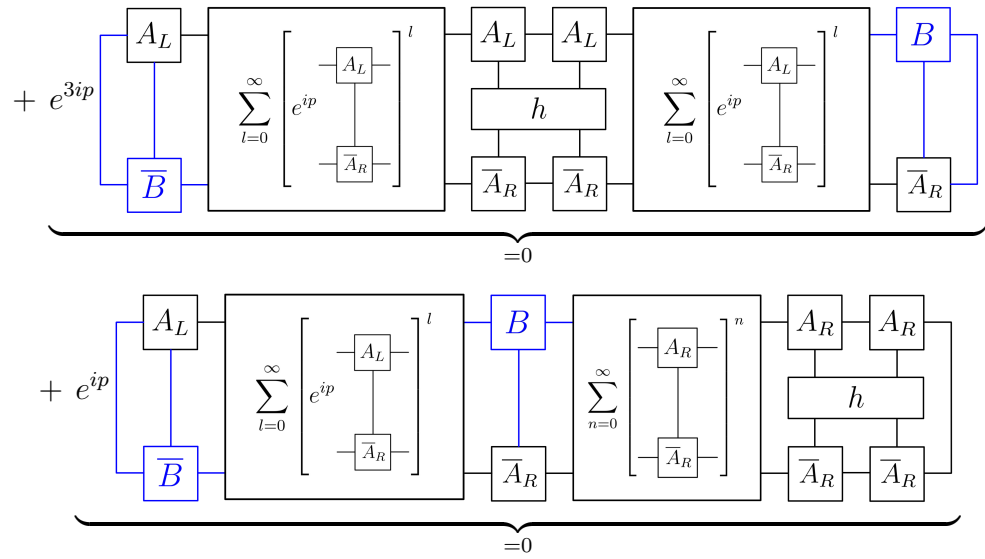
$$1) \quad m = -1, \dots, -\infty$$

$$1a) \quad n = -2, \dots, -\infty$$



1b) $n = -1$ 1c) $n = 0$ 1d) $n = 1, \dots, \infty$ 2) $m = 0$ 2a) $n = -2, \dots, -\infty$ 2b,c) $n = -1, 0$ 

2d) $n = 1, \dots, \infty$ 3) $m = 1, \dots, \infty$ 3a) $n = -2, \dots, -\infty$ 3b) $n = -1$ 3c) $n = 0$ 3d) $n = 1, \dots, \infty$ 

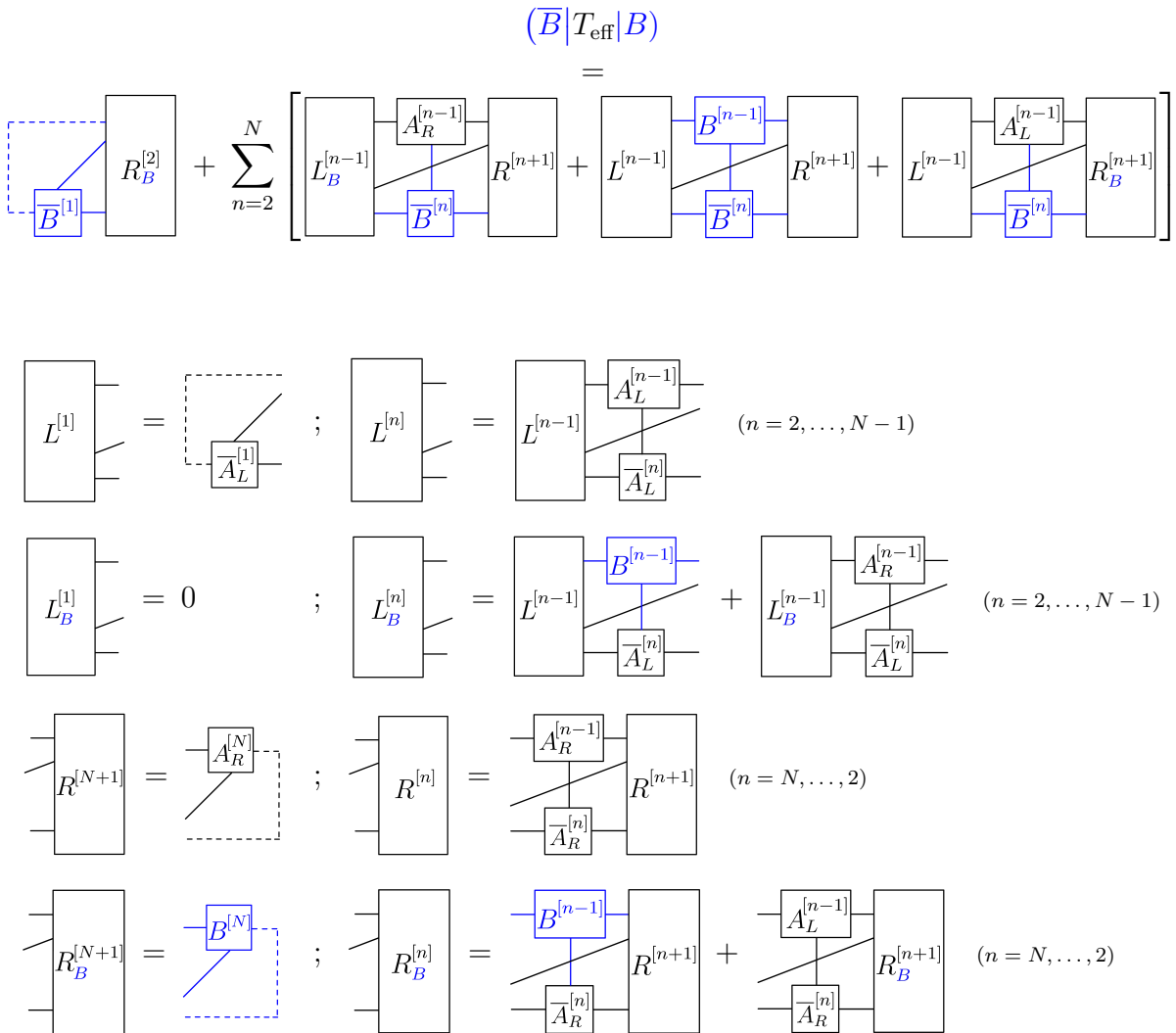


Effective translation operator for MPS quasiparticle excitations

For an MPS quasiparticle excitation ansatz (5.31), variational in both energy and momentum, we have to solve the eigenvalue problem

$$\left[H_{\text{eff}} - \alpha \left(e^{-i\frac{2\pi}{N}k} T_{\text{eff}} + e^{i\frac{2\pi}{N}k} T_{\text{eff}}^\dagger \right) \right] |B\rangle = \epsilon_k |B\rangle.$$

In this appendix we specify the boundary tensors for the effective translation operator T_{eff} and its adjoint. Note that $B^{[n]} = V_L^{[n]} X^{[n]}$ (5.30).



$$\begin{aligned}
 & (\overline{B} | T_{\text{eff}}^\dagger | B) \\
 = & \sum_{n=1}^{N-1} \left[\begin{array}{c} \text{Diagram 1} \\ + \end{array} \right. \begin{array}{c} \text{Diagram 2} \\ + \end{array} \left. \begin{array}{c} \text{Diagram 3} \\ + \end{array} \right] \quad \text{Diagram 4}
 \end{aligned}$$

Diagram 1:

Diagram 2:

Diagram 3:

Diagram 4:

$$\begin{aligned}
 L^{[0]} &= \boxed{A_L^{[1]}} ; \quad L^{[n]} = \begin{array}{c} \text{Diagram 1} \\ + \end{array} \quad (n = 1, \dots, N-1) \\
 L_B^{[0]} &= \boxed{B^{[1]}} ; \quad L_B^{[n]} = \begin{array}{c} \text{Diagram 2} \\ + \end{array} \quad (n = 1, \dots, N-1) \\
 R^{[N]} &= \boxed{\overline{A}_R^{[N]}} ; \quad R^{[n]} = \begin{array}{c} \text{Diagram 3} \\ + \end{array} \quad (n = N-1, \dots, 2) \\
 R_B^{[N]} &= 0 ; \quad R_B^{[n]} = \begin{array}{c} \text{Diagram 4} \\ + \end{array} \quad (n = N-1, \dots, 2)
 \end{aligned}$$

Diagram 1:

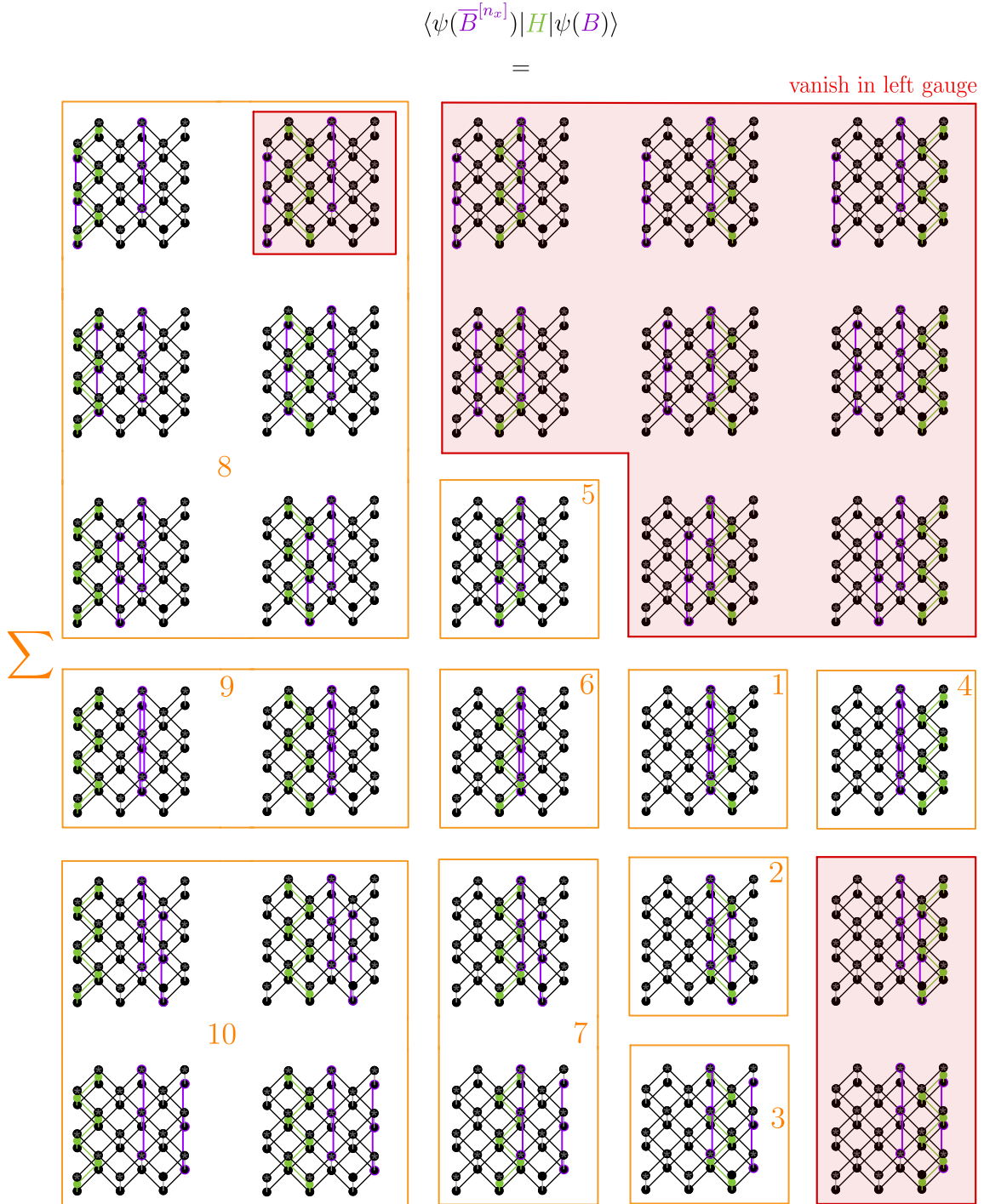
Diagram 2:

Diagram 3:

Diagram 4:

Effective Hamiltonian for isoPEPS quasiparticle excitations

We show all terms that appear when sandwiching the Hamiltonian (6.23) between the ket superposition (6.69) and a single bra state of the latter. Since we are ultimately interested in implementing the effective Hamiltonian $[H_{\text{eff}}|B)]^{[n_x,y]} = \partial_{\overline{B}^{[n_x,y]}} \langle \psi(\overline{B}^{[n_x]}) | H | \psi(B) \rangle$ with compressed bMPS, we move the ket excitations and column MPO Hamiltonians relative to the bra column $\overline{B}^{[n_x]}$ (here exemplarily for $n_x = 4$):



Bibliography

- [AKLV13] Itai Arad, Alexei Kitaev, Zeph Landau, and Umesh Vazirani. An area law and sub-exponential algorithm for 1d systems. *arXiv preprint arXiv:1301.1162*, 2013.
- [BD02] Henk WJ Blöte and Youjin Deng. Cluster monte carlo simulation of the transverse ising model. *Physical Review E*, 66(6):066110, 2002.
- [CPGSV17] J Ignacio Cirac, David Perez-Garcia, Norbert Schuch, and Frank Verstraete. Matrix product density operators: Renormalization fixed points and boundary theories. *Annals of Physics*, 378:100–149, 2017.
- [CPGSV21] J Ignacio Cirac, David Perez-Garcia, Norbert Schuch, and Frank Verstraete. Matrix product states and projected entangled pair states: Concepts, symmetries, theorems. *Reviews of Modern Physics*, 93(4):045003, 2021.
- [DVMP23] Markus Drescher, Laurens Vanderstraeten, Roderich Moessner, and Frank Pollmann. Dynamical signatures of symmetry-broken and liquid phases in an $s=1/2$ heisenberg antiferromagnet on the triangular lattice. *Physical Review B*, 108(22):L220401, 2023.
- [FGSW⁺15] Carlos Fernández-González, Norbert Schuch, Michael M Wolf, J Ignacio Cirac, and David Perez-Garcia. Frustration free gapless hamiltonians for matrix product states. *Communications in Mathematical Physics*, 333:299–333, 2015.
- [Has07] Matthew B Hastings. An area law for one-dimensional quantum systems. *Journal of statistical mechanics: theory and experiment*, 2007(08):P08024, 2007.
- [HCO⁺11] Jutho Haegeman, J Ignacio Cirac, Tobias J Osborne, Iztok Pižorn, Henri Verschelde, and Frank Verstraete. Time-dependent variational principle for quantum lattices. *Physical review letters*, 107(7):070601, 2011.
- [HJ12] Roger A Horn and Charles R Johnson. *Matrix analysis*. Cambridge university press, 2012.
- [HLO⁺16] Jutho Haegeman, Christian Lubich, Ivan Oseledets, Bart Vandereycken, and Frank Verstraete. Unifying time evolution and optimization with matrix product states. *Physical Review B*, 94(16):165116, 2016.
- [HMOV14] Jutho Haegeman, Michaël Mariën, Tobias J Osborne, and Frank Verstraete. Geometry of matrix product states: Metric, parallel transport, and curvature. *Journal of Mathematical Physics*, 55(2), 2014.
- [HOV13] Jutho Haegeman, Tobias J Osborne, and Frank Verstraete. Post-matrix product state methods: To tangent space and beyond. *Physical Review B—Condensed Matter and Materials Physics*, 88(7):075133, 2013.

- [HPW⁺12] Jutho Haegeman, Bogdan Pirvu, David J Weir, J Ignacio Cirac, Tobias J Osborne, Henri Verschelde, and Frank Verstraete. Variational matrix product ansatz for dispersion relations. *Physical Review B—Condensed Matter and Materials Physics*, 85(10):100408, 2012.
- [KM19] Johannes Knolle and Roderich Moessner. A field guide to spin liquids. *Annual Review of Condensed Matter Physics*, 10(1):451–472, 2019.
- [LZP22] Sheng-Hsuan Lin, Michael P Zaletel, and Frank Pollmann. Efficient simulation of dynamics in two-dimensional quantum spin systems with isometric tensor networks. *Physical Review B*, 106(24):245102, 2022.
- [MZMP16] Johannes Motruk, Michael P Zaletel, Roger SK Mong, and Frank Pollmann. Density matrix renormalization group on a cylinder in mixed real and momentum space. *Physical Review B*, 93(15):155139, 2016.
- [Orú14] Román Orús. A practical introduction to tensor networks: Matrix product states and projected entangled pair states. *Annals of physics*, 349:117–158, 2014.
- [Pag93] Don N Page. Average entropy of a subsystem. *Physical review letters*, 71(9):1291, 1993.
- [Pfe70] Pierre Pfeuty. The one-dimensional ising model with a transverse field. *ANNALS of Physics*, 57(1):79–90, 1970.
- [PGVWC07] D Perez-Garcia, Frank Verstraete, MM Wolf, and JI Cirac. Matrix product state representations. *QUANTUM INFORMATION & COMPUTATION*, 7(5-6):401–430, 2007.
- [PMTM09] Frank Pollmann, Subroto Mukerjee, Ari M Turner, and Joel E Moore. Theory of finite-entanglement scaling at one-dimensional quantum critical points. *Physical review letters*, 102(25):255701, 2009.
- [Sac11] Subir Sachdev. *Quantum Phase Transitions*. Cambridge University Press, 2 edition, 2011.
- [San10] Anders W Sandvik. Computational studies of quantum spin systems. In *AIP Conference Proceedings*, volume 1297, pages 135–338. American Institute of Physics, 2010.
- [Sap24] Benjamin Sapler. Development of a diagonal isometric tensor network algorithm. <https://github.com/SnackerBit/YB-isoTPS>, 2024.
- [Sch11] Ulrich Schollwöck. The density-matrix renormalization group in the age of matrix product states. *Annals of physics*, 326(1):96–192, 2011.
- [SCPG10] Norbert Schuch, Ignacio Cirac, and David Pérez-García. Peps as ground states: Degeneracy and topology. *Annals of Physics*, 325(10):2153–2192, 2010.
- [SKZP25] Benjamin Sapler, Masataka Kawano, Michael P Zaletel, and Frank Pollmann. Diagonal isometric form for tensor product states in two dimensions. *arXiv preprint arXiv:2507.08080*, 2025.

- [SSB⁺20] Tomohiro Soejima, Karthik Siva, Nick Bultinck, Shubhayu Chatterjee, Frank Pollmann, and Michael P Zaletel. Isometric tensor network representation of string-net liquids. *Physical Review B*, 101(8):085117, 2020.
- [Tas20] Hal Tasaki. *Physics and mathematics of quantum many-body systems*, volume 66. Springer, 2020.
- [VC04] Frank Verstraete and J Ignacio Cirac. Renormalization algorithms for quantum-many body systems in two and higher dimensions. *arXiv preprint cond-mat/0407066*, 2004.
- [VC06] Frank Verstraete and J Ignacio Cirac. Matrix product states represent ground states faithfully. *Physical Review B—Condensed Matter and Materials Physics*, 73(9):094423, 2006.
- [VDVH⁺21] Maarten Van Damme, Robijn Vanhove, Jutho Haegeman, Frank Verstraete, and Laurens Vanderstraeten. Efficient matrix product state methods for extracting spectral information on rings and cylinders. *Physical Review B*, 104(11):115142, 2021.
- [VHV19a] Laurens Vanderstraeten, Jutho Haegeman, and Frank Verstraete. Simulating excitation spectra with projected entangled-pair states. *Physical Review B*, 99(16):165121, 2019.
- [VHV19b] Laurens Vanderstraeten, Jutho Haegeman, and Frank Verstraete. Tangent-space methods for uniform matrix product states. *SciPost Physics Lecture Notes*, page 007, 2019.
- [Vid04] Guifré Vidal. Efficient simulation of one-dimensional quantum many-body systems. *Physical review letters*, 93(4):040502, 2004.
- [VMVH15] Laurens Vanderstraeten, Michaël Mariën, Frank Verstraete, and Jutho Haegeman. Excitations and the tangent space of projected entangled-pair states. *Physical Review B*, 92(20):201111, 2015.
- [WAL⁺23] Yantao Wu, Sajant Anand, Sheng-Hsuan Lin, Frank Pollmann, and Michael P Zaletel. Two-dimensional isometric tensor networks on an infinite strip. *Physical Review B*, 107(24):245118, 2023.
- [Whi92] Steven R White. Density matrix formulation for quantum renormalization groups. *Physical review letters*, 69(19):2863, 1992.
- [Wit25] Lukas Wittmann. Variational ground states and quasiparticle excitations in isometric tensor network states. https://github.com/lukasjwittmann/iso_tns-public, 2025.
- [Wol12] Michael M. Wolf. Quantum channels and operations - guided tour. Graue Literatur, <https://mediatum.ub.tum.de/node?id=1701036>, 2012.
- [Wol22] Michael M. Wolf. Mathematical introduction to quantum information processing. Graue Literatur, <https://mediatum.ub.tum.de/node?id=1706981>, 2022.

- [ZP20] Michael P Zaletel and Frank Pollmann. Isometric tensor network states in two dimensions. *Physical review letters*, 124(3):037201, 2020.
- [ZSVF⁺18] Valentin Zauner-Stauber, Laurens Vanderstraeten, Matthew T Fishman, Frank Verstraete, and Jutho Haegeman. Variational optimization algorithms for uniform matrix product states. *Physical Review B*, 97(4):045145, 2018.